Petrogenesis, W metallogenic and tectonic implications of granitic intrusions in the southern Great Xing'an Range W belt, NE China: insights from the Narenwula Complex

Wei Xie[1,2,3] (iD), Qing-Dong Zeng[1,2,3], Jin-Hui Yang[2,3,4], Rui Li[2,3,4], Zhuang Zhang[5], Rui-Liang Wang[6] and Jin-Jian Wu[1,2,3]

[1]Key Laboratory of Mineral Resources, Institute of Geology and Geophysics, Chinese Academy of Sciences, Beijing 100029, China; [2]Innovation Academy for Earth Science, Chinese Academy of Sciences, Beijing 100029, China; [3]College of Earth and Planetary Sciences, University of Chinese Academy of Sciences, Beijing 100049, China; [4]State Key Laboratory of Lithospheric Evolution, Institute of Geology and Geophysics, Chinese Academy of Sciences, Beijing 100029, China; [5]Chifeng Chaihulanzi Gold Mining Co. Ltd, Chifeng 024000, China and [6]Faculty of Geosciences and Resources, China University of Geosciences (Beijing), Beijing 100083, China

Abstract

Extensive magmatism in NE China, eastern Central Asian Orogenic Belt, has produced multistage granitic plutons and accompanying W mineralization. The Narenwula complex in the southwestern Great Xing'an Range provides important insights into the petrogenesis, geodynamic processes and relationship with W mineralization. The complex comprises granodiorites, monzogranites and granite porphyry. Mafic microgranular enclaves are common in the granodiorites, and have similar zircon U–Pb ages as their host rocks (258.5–253.9 Ma), whereas the W-bearing granitoids yield emplacement ages of 149.8–148.1 Ma. Permian granodiorites are I-type granites that are enriched in large-ion lithophile elements and light rare earth elements, and depleted in high field strength elements and heavy rare earth elements. Both the mafic microgranular enclaves and granodiorites have nearly identical zircon Hf isotopic compositions. The results suggest that the mafic microgranular enclaves and granodiorites formed by the mixing of mafic and felsic magmas. W-bearing granitoids are highly fractionated A-type granites, enriched in Rb, Th, U and Pb, and depleted in Ba, Sr, P, Ti and Eu. They have higher W concentrations and Rb/Sr ratios, and lower Nb/Ta, Zr/Hf and K/Rb ratios than the W-barren granodiorites. These data and negative $\epsilon_{Hf}(t)$ values (–6.0 to –2.1) suggest that they were derived from the partial melting of ancient lower crust and subsequently underwent extreme fractional crystallization. Based on the regional geology, we propose that the granodiorites were generated in a volcanic arc setting related to the subduction of the Palaeo-Asian Ocean, whereas the W-bearing granitoids and associated deposits formed in a post-orogenic extensional setting controlled by the Mongol–Okhotsk Ocean and Palaeo-Pacific Ocean tectonic regimes.

1. Introduction

NE China, previously tectonically referred to as the Xing-Meng Orogenic Belt (XMOB), comprises the main part of the eastern segment of the Central Asian Orogenic Belt (CAOB) and is one of the most important polymetallic metallogenic regions in China (Zeng *et al.* 2012, 2015a; Ouyang *et al.* 2015; Wang *et al.* 2021) (Fig. 1). Numerous W deposits have been discovered in NE China, demonstrating the significant W metallogenic potential of this region (Ouyang *et al.* 2015; Zeng *et al.* 2015b; Liu *et al.* 2016; Wang *et al.* 2017; Zhang, X. B. *et al.* 2017; Gao *et al.* 2019; Wang, R. L. *et al.* 2020; Xie *et al.* 2021). At present, NE China is known to host 4 large, 18 medium and 17 small W deposits (Fig. 1c). Three W belts can be distinguished according to the distribution of the W deposits: the northern and central Great Xing'an Range W belt (NCGB), southern Great Xing'an Range W belt (SGB) and Lesser Xing'an–Zhangguangcai Range W belt (LXZB) (Xie *et al.* 2021) (Fig. 1c).

The SGB, situated in the southwestern part of NE China, hosts voluminous Mesozoic W deposits (Fig. 1c). All of these W deposits are spatially and genetically related to granitic intrusions (Xie *et al.* 2021). Although some studies have been conducted on the petrogenesis of these W-related granitic plutons, the petrogenesis of the these granitoids remains controversial (Mei *et al.* 2015; Zeng *et al.* 2015b; Wang *et al.* 2017; Gao *et al.* 2019; Yang *et al.* 2019). In addition, the distribution of W-related and W-barren granitoids commonly overlaps. However, because of the paucity of detailed comparative studies, the geochemical difference between the W-related and W-barren granitoids is not clear, which limits our understanding of the

CAMBRIDGE
UNIVERSITY PRESS
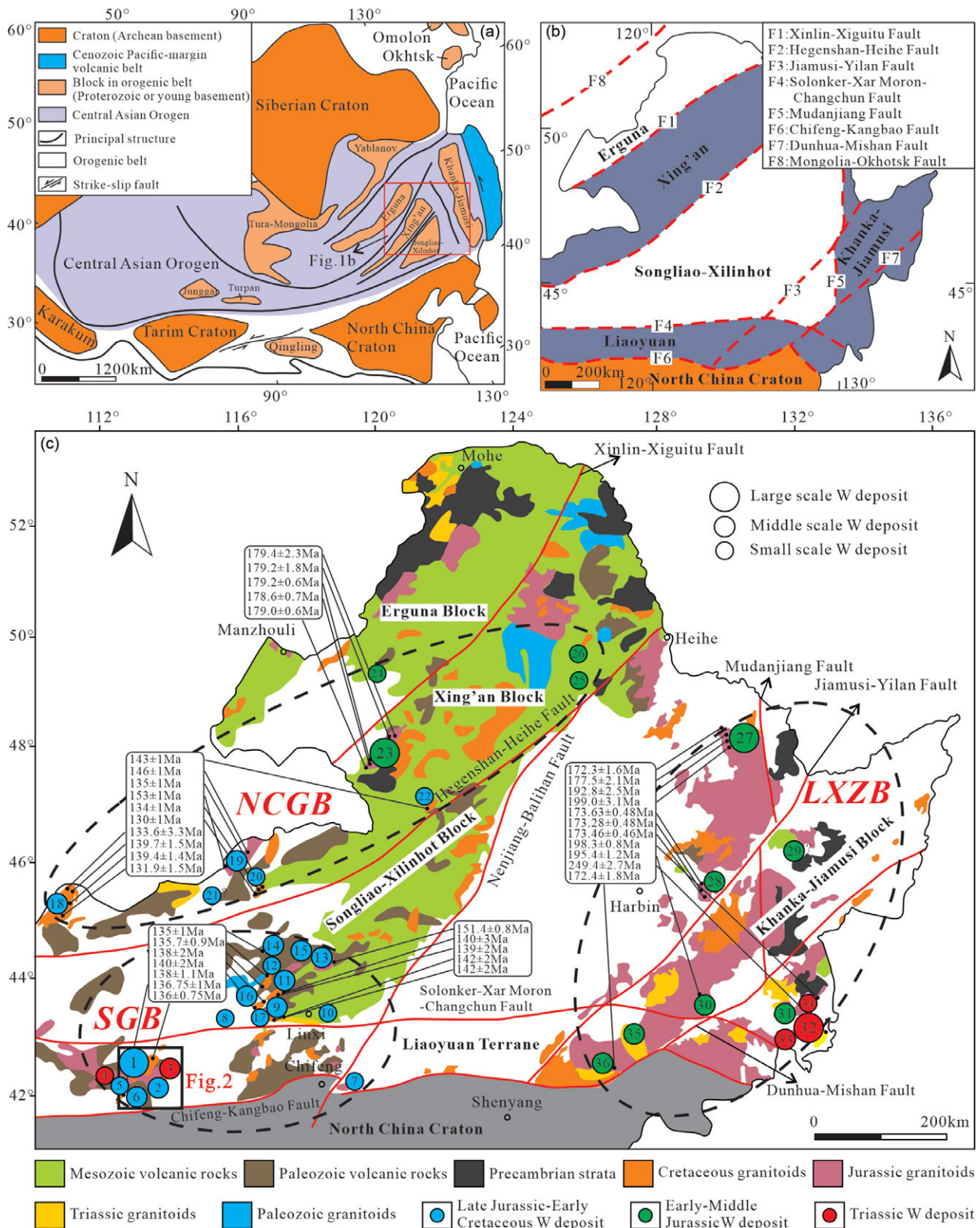
Fig. 1. (Colour online) (a) simplified tectonic map of the Central Asian Orogenic Belt (modified from Liu, Y. J. *et al*. 2017; Feng *et al*. 2019). (b) schematic tectonic map of NE China (modified from Wu *et al*. 2011). (c) distribution of major tungsten deposits in NE China (modified from Zeng *et al*. 2012). The black solid circles mark the sampling locations of the previously published geochronological data for W-related granitoids in NE China, which are in online Supplementary Material Table S1. Deposit locations: 1 – Narenwula; 2 – Baishitouwa; 3 – Shazigou; 4 – Tianbaogou; 5 – Shalahada; 6 – Sansheng; 7 – Halihaitu; 8 – Chamuhan; 9 – Xiaolaogualinzi; 10 – Baiyinhan; 11 – Weilasituo; 12 – Wulegeerjidaban; 13 – Dongshanwan; 14 – Daolundaba; 15 – Xiaohaiqing; 16 – Huanggang; 17 – Xiaodonggou; 18 – Wurinitu; 19 – Shamai; 20 – Dayana; 21 –Bayandulan; 22 – Weilianhe; 23 – Honghuaerji; 24 – Zishi; 25 – Guanniaohe; 26 – Weijiang; 27 – Cuihongshan; 28 – Gongpengzi; 29 – Yangbishan; 30 – Xin'antun; 31 – Baishilizi; 32 – Yangjingou; 33 – Wudaogou; 34 – Liudaogou; 35 – Xinglong; 36 – Sanjiazi. Abbreviations: NCGB – northern and central Great Xing'an Range W belt; SGB – southern Great Xing'an Range W belt; LXZB – Lesser Xing'an–Zhangguangcai Range W belt.

genetic mechanism between granitic magmatism and W mineralization. Moreover, the tectonic evolution of the SGB was essential for the spatial and temporal distribution of W-related granitoids and related deposits. Romer & Kroner (2016) highlighted that different tectonic settings may have led to the input of mantle melt or the emplacement of ultrahigh-temperature metamorphic rocks, which were crucial for metal extraction from the source rocks, thus playing a critical role in controlling the discontinuous distribution of W mineralization within the belt. However, the overprinting of the Palaeo-Asian Ocean (PAO), Mongol–Okhotsk Ocean (MOO) and Palaeo-Pacific Ocean (PPO) tectonic regimes had significant influence on the SGB during late Mesozoic time, which has led to disagreements on the interpretation of the deep geodynamic processes and limited our understanding of regional W-related granitic magmatism and W mineralization. Several models have been proposed for the SGB tectonic setting during late Mesozoic time, including (a) upwelling of a mantle plume (Wang, T. *et al.* 2015), (b) post-orogenic gravitational collapse and/or subduction-induced back-arc extension related to the closure of the MOO (Wang, Z. H. *et al.* 2015; Fritzell *et al.* 2016; Guan *et al.* 2018; Ji *et al.* 2018, 2020; Han *et al.* 2021; Shi *et al.* 2020; Wei *et al.* 2021), (c) arc/back-arc extension and asthenosphere upwelling induced by subduction of the PPO (Ji *et al.* 2019; Li, S. Z. *et al.* 2019; Suo *et al.* 2019; He *et al.* 2020; Sun *et al.* 2020; Wang, L *et al.* 2020; Wei *et al.* 2020; Jing *et al.* 2021), and (d) compositional effects resulting from the closure of the MOO and subduction of the PPO (Ouyang *et al.* 2015; Liu, C. F. *et al.* 2017; Liu *et al.* 2020; Pang *et al.* 2020; Zhang, C. *et al.* 2020; Mi *et al.* 2021). Additionally, although researchers generally agree that the disappearance of the PAO occurred along the Solonker–Xar Moron–Changchun Fault (SXCF), the closure time of the PAO remains ambiguous (Liu, Y. J. *et al.* 2017). There are two different models: one popular model suggests that the closure occurred during late Permian to Early Triassic times (Chen *et al.* 2000; Zhai & Santosh, 2013; Ju & Hou, 2014; Xiao & Santosh, 2014; Han *et al.* 2015; Liu & Nie, 2015; Wilde, 2015), while another model dates the closure to the pre-Permian period (Zhang, X. H. *et al.* 2008; Shi *et al.* 2010; Xu, B. *et al.* 2013, 2015; Xu, W. L. *et al.* 2013; Li, Y. L. *et al.* 2014).

The Narenwula complex is situated in the southwestern section of the SGB and is adjacent to the boundary between the XMOB and the North China Craton (NCC) (Fig. 1c), comprising granodiorite, monzogranite and granite porphyry. The monzogranite and granite porphyry are W-bearing granitoids, while the granodiorites are W-barren granitoids. Therefore, the Narenwula complex provides an excellent opportunity to understand the genesis and geochemical differences between W-related and W-barren granitoids, and more importantly, the link between granitic magmatism and W mineralization. It also provides an avenue to investigate the tectonic evolution and geodynamic setting for the formation of the W-related granitoids and associated deposits in the SGB, which have great significance for the further exploration of W deposits in this region. In this paper, we report field and petrographic observations, zircon U–Pb dating, whole-rock geochemistry and zircon Hf isotopic data for the mafic microgranular enclaves (MMEs), their host granodiorites and W-bearing granitoids from the Narenwula complex. We use these data to constrain the petrogenesis and geochemical differences of the granodiorites and W-bearing granitoids, as well as their relationship to W mineralization. The findings provide insights into the tectonic evolution of the SGB during late Permian and Late Jurassic times and advance our understanding of the regional W-related tectonic–magmatic–metallogenic mechanism.

2. Geological background and sampling

Tectonic components of the XMOB include the Erguna Block (EB), Xing'an Block (XB), Songliao–Xilinhot Block (SXB), Khanka–Jiamusi Block (KJB) (from NW to SE) and Liaoyuan Terrane (LT) in the south (Wu *et al.* 2011; Liu, Y. J. *et al.* 2017) (Fig. 1b). The Xinlin–Xiguitu Fault (XXF) represents the boundary between the EB and XB, the Hegenshan–Heihe Fault (HHF) separates the XB and SXB, the Mudanjiang Fault (MF) represents the boundary between the SXB and KJB, and the SXCF is the boundary between the SXB and LT (Wu *et al.* 2011; Liu, Y. J. *et al.* 2017) (Fig. 1c). Throughout the Phanerozoic Eon, the XMOB underwent a complex tectonomagmatic evolution involving multiple stages of accretion and collision (Sengör *et al.* 1993). During the Palaeozoic Era, the XMOB was controlled by the PAO tectonic regime, which led to the amalgamation of several micro-continental blocks, multi-arc systems and accretionary complexes (Wu *et al.* 2011; Xiao & Santosh, 2014). Since the Mesozoic Era, the XMOB has been affected mainly by the closure of the MOO and subduction of the PPO, leading to the widespread occurrence of Mesozoic volcanic rocks and coeval granitic intrusions (Wu *et al.* 2011).

The SGB, located in the southwestern part of NE China, extends north to Heilongjiang and Jilin provinces, and east to the Songliao Basin. This area is tectonically bordered by the HHF to the north, the Chifeng–Kangbao Fault (CKF) to the south and the Nenjiang–Balihan Fault (NBF) to the east (Xie *et al.* 2021) (Fig. 1c). The oldest formation in this region is a Palaeozoic medium- to high-grade metamorphic complex, dominantly composed of amphibolite gneiss, granite gneiss and mica schist. Several Ordovician–Silurian, Devonian and Carboniferous detrital metasedimentary units, carbonate rocks and volcanic formations occur in this region. Permian volcano-sedimentary formations, consisting of carbonaceous clastic rocks, carbonate rocks and mafic to intermediate–acidic volcanic rocks, are also abundant and act as the host rocks for many of the mineral deposits (Ouyang *et al.* 2015). Voluminous late Palaeozoic to Mesozoic granitic plutons intrude the Palaeozoic strata, which are overlain by Mesozoic volcano-sedimentary sequences. Recent geochronological data suggest that granitic magmatic events within the SGB can be subdivided into two stages: during the first stage, late Palaeozoic intrusions comprising diorite, tonalite and granodiorite were mainly distributed throughout the western part of the region and emplaced from 321 to 250 Ma based on the zircon U–Pb ages (Fig. 1c); during the second stage, Mesozoic granites, composed of granodiorite, monzonitic granite, granite porphyry and syenogranite, were emplaced from 150 to 131 Ma based on zircon U–Pb ages (Wu *et al.* 2011; Wan *et al.* 2019).

The Narenwula region in the southwestern SGB features large-scale W polymetallic mineralization (Fig. 2). This region has local exposures of Proterozoic–early Palaeozoic leptite, granulite, metasandstone, slate, phyllite, schist and crystalline limestone. The widely exposed lower Permian and Jurassic strata consist of intermediate–acid volcanic rocks, volcaniclastic rocks and sedimentary clastic rocks (IMBGMR, 1991). The intrusive rocks mainly include late Permian, Triassic, Early–Middle Jurassic and Late Jurassic granitic intrusions (Fig. 2). The widespread late Permian felsic intrusive rocks intrude into the Proterozoic–lower Palaeozoic strata. The rock types mainly include granodiorite and quartz diorite. A Triassic granitic pluton is locally exposed in the southwestern part of this region, related to the W mineralization in the Tantoushan deposit (unpub. data). Early–Middle Jurassic granitoids mainly occur in the western part of the region, with
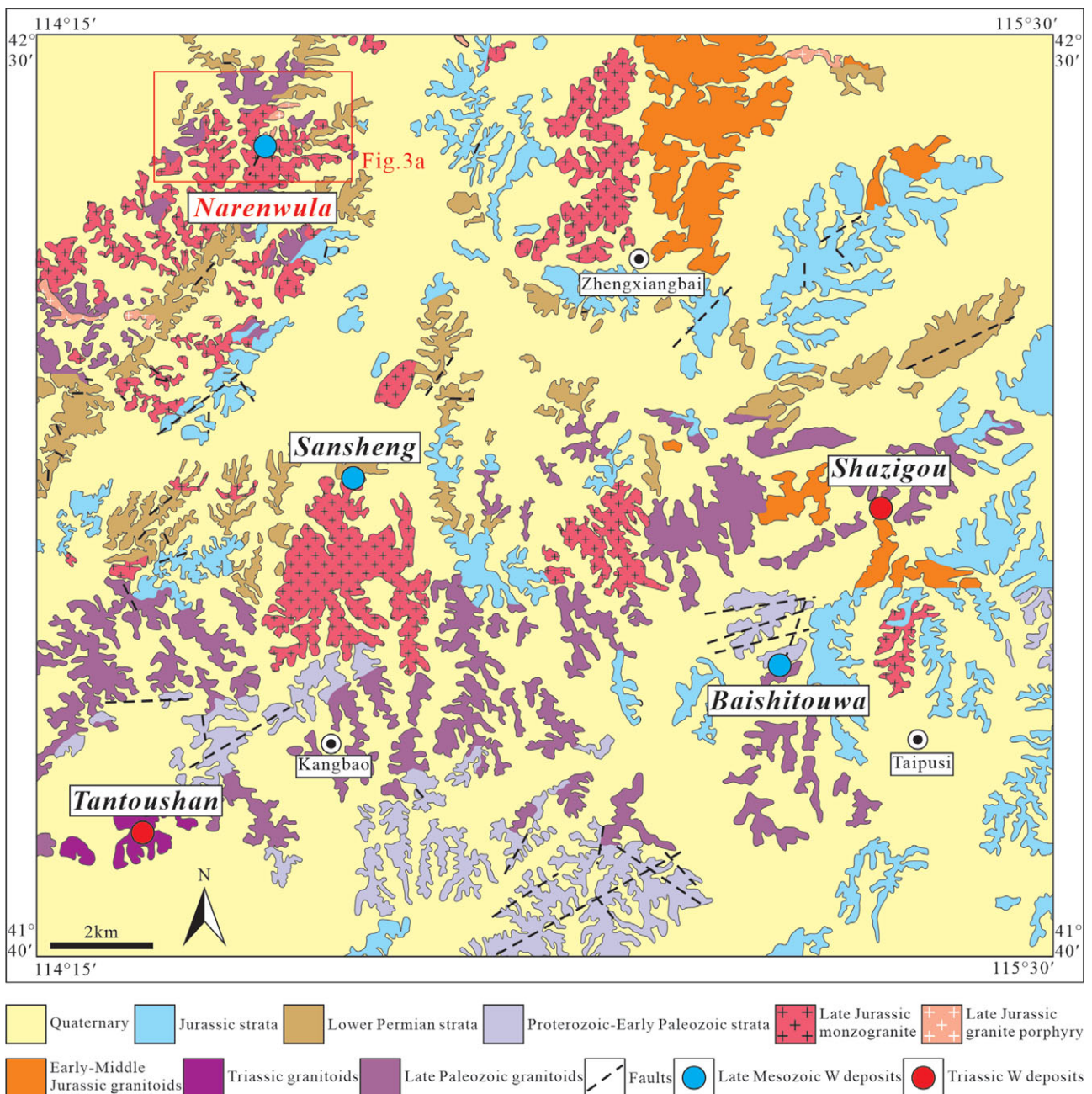
Fig. 2. (Colour online) Simplified geological map of the Narenwula region (after IMBGMR, 1991).

minor occurrences in the eastern part, comprising fine-grained and minor biotite granite. Late Jurassic granitoids are common in the central and western parts of this region, mainly composed of monzogranite and granite porphyry (IMBGMR, 1991) (Fig. 2).

The Narenwula quartz-vein type W polymetallic deposit (42° 25′ N, 114° 31′ E) is situated in the southwestern part of the SGB (Fig. 2). This deposit has estimated reserves of 89 950 t WO_3 with a grade of 0.776 %. The strata exposed in the mining area are mainly the lower Permian Sanmianjing and Erlitu formations and Quaternary sediments (Fig. 3). The Sanmianjing Formation contains tuff, silt-slate, sandstone and conglomerate. The Erlitu Formation consists of andesite, tuff and sedimentary tuff (IMBGMED, 2016). These rocks are intruded by the Narenwula complex (Fig. 3). The orebodies mainly occur as veins in the monzogranite and granite porphyry (Fig. 3b, c).

The granodiorite unit (samples WL-28, WL-29, WL-30, WL-31, WL-32-2 and WL-32-3) is grey-white to pale red in colour and shows a hypidiomorphic granular texture, with a massive structure (Fig. 4a–c). It contains plagioclase (0.5–2 mm; 60–65 %), quartz (0.5–1 mm; ~20–25 %), hornblende (0.4–1 mm; ~10 %), biotite (0.8–1.5 mm; 5–10 %) and alkali feldspar (~0.5 mm; < 5 %). MMEs are common in the granodiorites from the complex. The MME samples (samples WL-33-2, WL-34 and WL-34-2) are dark grey in colour and exhibit a porphyritic or hypidiomorphic granular texture (Fig. 4d, e). The phenocrysts (15–25 % rock mass) comprise plagioclase (0.5–3 mm; ~25–45 %), biotite (0.5–3.5 mm; ~25–35 %) and a low proportion of hornblende (0.5–1.5 mm; ~20 %). The matrix is mainly composed of hornblende, plagioclase, biotite, minor pyroxene, aphanitic minerals and magnetite.
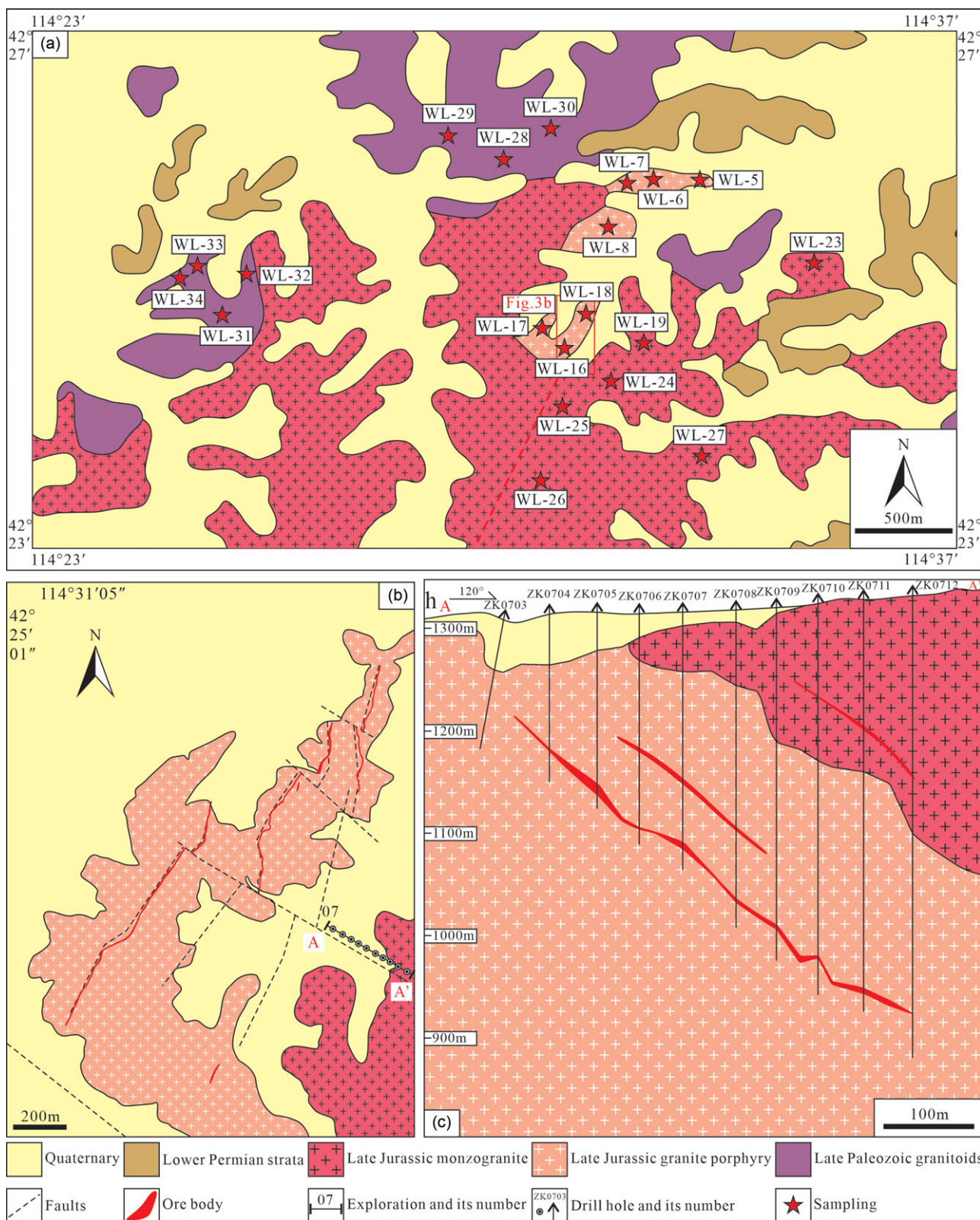
Fig. 3. (Colour online) (a, b) Geological map of the Narenwula deposit showing the sampling locations. (c) Schematic geological cross-section of no. 07 exploration line (after IMBGMED, 2016).

The monzogranite and granite porphyry are the ore-bearing rocks (Fig. 3b, c). The monzogranite unit (samples WL-5, WL-19, WL-23, WL-24, WL-25, WL-26-1 and WL-27) is red in colour and displays a hypidiomorphic granular texture, with a massive structure (Fig. 4f–i). It consists of quartz (1–2.5 mm; 30–40 %), alkali feldspar (1.5–2.5 mm; 25–35 %), plagioclase (0.8–1.5 mm; 15–20 %) and biotite (1–1.5 mm; < 5 %), along with accessory minerals. The granite porphyry unit (samples WL-6, WL-7-2,
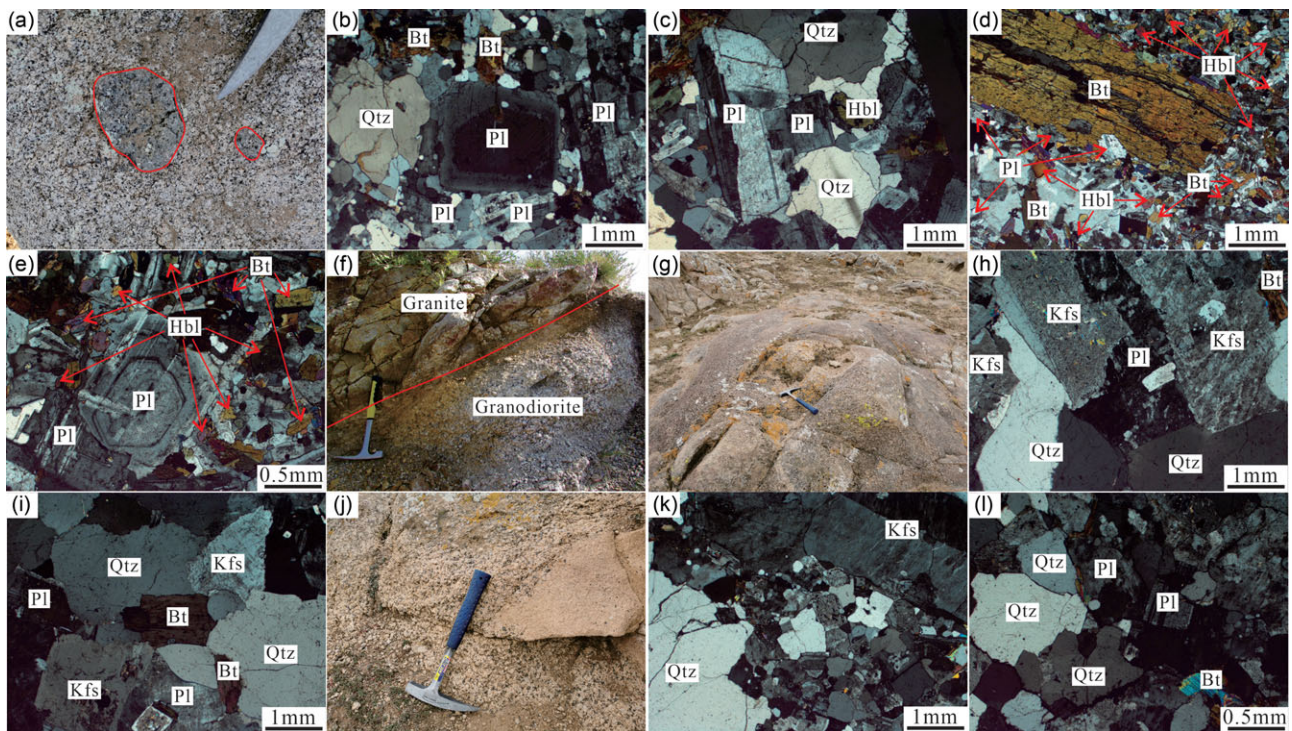
Fig. 4. (Colour online) Lithologic characteristics and representative photographs (crossed-polarized light) of granitoids and MMEs from the Narenwula complex. (a–c) Granodiorite. (d, e) Mafic microgranular enclaves in granodiorite. (f–i) Monzogranite. (j–l) Granite porphyry. Abbreviations: Pl – plagioclase; Kfs – potassium feldspar; Hbl – hornblende; Qtz – quartz; Bt – biotite. Length of hammer for scale is ~330 mm.

WL-8-2, WL-16, WL-17, WL-18 and WL-26-2) is pale red in colour with a porphyritic texture (Fig. 4j–l). The phenocrysts are mainly anhedral quartz (0.5–2 mm; ~15–20 %), subhedral to euhedral alkali feldspar (1–2.5 mm; ~15–20 %) and plagioclase (0.5–1 mm; ~5–10 %). The groundmass (~50 %) consists of quartz, plagioclase, alkali feldspar and biotite.

Eighty-five orebodies have been discovered in the mining district. NE-trending faults mainly control the orebodies (Fig. 3b), which dip to the SE at an angle of 30–48°. The individual orebodies have a length of 300–1010 m, thickness of 1.00–5.35 m and slope depth of 100–636 m. The ore structures are massive, disseminated and in the form of veinlets. The ore minerals are mainly wolframite, bismuthinite, cassiterite and pyrite, with minor amounts of sphalerite, galena, chalcopyrite, argentite and pyrrhotite. The gangue minerals are predominantly quartz with varying amounts of muscovite, biotite, apatite, plagioclase, K-feldspar, sericite and carbonate. Wall-rock alteration consists of silicification, sericitization, K-feldspathization, greisenization, chloritization, epidotization and kaolinization.

3. Analytical methods

3.a. Zircon U–Pb dating

Zircons from four representative granitoid samples and one MME sample from the Narenwula complex were analysed using laser ablation inductively coupled plasma mass spectrometry (LA-ICP-MS) U–Pb dating. Figure 3a shows the sampling locations. The samples were analysed at the mineral separation laboratory at the Regional Geology Minerals Investigation Research Institute, Hebei Province, China. Zircon grains were collected using conventional density and magnetic separation techniques

before handpicking under a binocular microscope. Transmitted and reflected microscopy images were then collected to examine the exterior structures while cathodoluminescence (CL) images were collected to examine the internal textures in the zircon to identify and select points on each grain suitable for U–Pb analyses.

LA-ICP-MS U–Pb dating analyses were conducted at the Institute of Geology and Geophysics, Chinese Academy of Sciences. The operating conditions for the laser ablation system and ICP-MS instrument, including the data reduction methods, are similar to those reported by Liu *et al.* (2010). Laser sampling was performed using a GeoLasPro laser coupled with an Agilent 7700e ICP-MS instrument. A laser spot size of 32 μm and a laser repetition rate of 6 Hz were used during the analyses. Quantitative calibration for the trace-element analyses and U–Pb dating was performed using the ICPMSDataCal software (Liu *et al.* 2010). Zircon 91500 was used as the external U–Pb dating standard and analysed twice every five analyses. The single point analytical error for the isotopic ratios and ages is reported at the 1σ level. Concordia diagrams were constructed using the ISOPLOT software (Ludwig, 2003).

3.b. In situ *zircon Hf isotope analyses*

In situ zircon Hf isotopic analyses were conducted at Beijing Createch Testing Technology Co., Ltd, Beijing, China, using a Thermo Scientific Neptune (Plus) multi-collector-ICP-MS (MC-ICP-MS) coupled to a New Wave 213 nm solid-state laser ablation system. The analyses were conducted on the same zircon grains that were previously analysed for U–Pb isotopes. The laser ablation beam was 35 μm in diameter, with a 10 Hz laser repetition rate and laser energy of 10–11 J cm^{-2}. Ablated material was injected into the MC-ICP-MS with a high-purity He carrier gas.

Details on the instrumental conditions and data acquisition protocols are reported by Hou *et al.* (2007). The $^{176}Hf/^{177}Hf$ ratio was normalized to $^{179}Hf/^{177}Hf = 0.7325$. Hafnium isotopic data were age-corrected using a ^{176}Lu decay constant of $1.867 \times 10^{-11} a^{-1}$ (Söderlund *et al.* 2004). The $\epsilon_{Hf}(t)$ values and Hf model ages were calculated using the methods reported by Bouvier *et al.* (2008) and Griffin *et al.* (2002), respectively.

3.c. Major- and trace-element analyses

After combining samples from the hand-picked specimens with those selected for microscopic photography, weathered surfaces were removed and the samples were ground in an agate mill to 200-mesh. Concentrations of the major (ME-XRF26d analytical package) and trace (ME-MS81 analytical package) elements were determined at ALS Chemex, Guangzhou, China. Major-element analyses were performed using X-ray fluorescence (XRF) with a PANalytical PW2424 instrument. Approximately 0.5 g of crushed whole-rock power were dissolved using $LiNO_3$, and a glass bead was then produced after fusion. According to the measured values of the GSR-1 standard, uncertainties were less than 5 %. Trace-element concentrations were determined using a Perkin Elmer Elan 9000 ICP-MS instrument. Approximately 50 mg of crushed whole-rock powder were dissolved using a $LiBO_2/Li_2B_4O_7$ mixture at ~1025 °C. The solution was then extracted after cooling and diluted with HF, HCl and HNO_3 before measurement. External standards BHVO-1 and G-2 were used to monitor drift in the mass response during measurement. The precision was generally better than 10 % for most trace elements.

4. Results

4.a. Zircon U–Pb ages

The dating results for four granitic samples and one MME from the Narenwula complex are listed in Table 1. Figure 5 shows representative CL images of the zircon grains. These samples contain some fine-grained colourless-to-light yellow zircon crystals with an adamantine lustre. The grains commonly occur as short columns, with a small portion exhibiting elliptical or irregular shapes, with sizes ranging from 80 to 200 μm and length-to-width ratios of 1–3. Most of the zircon grains exhibit growth zoning without a core–rim structure, as shown in the CL images (Fig. 5). All zircons have high Th/U ratios (0.51–2.09), indicating a magmatic origin (Belousova *et al.* 2002).

For granite porphyry sample WL-16, with three grains showing $^{206}Pb-^{238}U$ age outliers (155.4 Ma for WL-16-1, 156.7 Ma for WL-16-4 and 143.9 Ma for WL-16-18), 15 analytical spots showed a tight concordant grouping, yielding a weighted mean $^{206}Pb-^{238}U$ age of 149.8 ± 2.7 Ma (1σ, MSWD = 0.23), which is the crystallization age of the granite porphyry (Fig. 6a).

One analysis result was excluded from the mean calculations owing to the discordant values for monzogranite sample WL-24. The remaining 14 points plot along a Concordia line with $^{206}Pb-^{238}U$ ages between 143.5 and 153.8 Ma, yielding a weighted mean $^{206}Pb-^{238}U$ age of 148.1 ± 2.1 Ma (1σ, MSWD = 0.35), which can be interpreted as the magmatic crystallization age of the monzogranite (Fig. 6b).

For granodiorite sample WL-28, all 18 analytical spots exhibit a tight concordant grouping with $^{206}Pb-^{238}U$ ages ranging from 252 to 267 Ma, yielding a weighted mean $^{206}Pb-^{238}U$ age of 258.5 ± 1.9 Ma (1σ, MSWD = 0.23), interpreted as the crystallization age of the granodiorite (Fig. 6c).

For granodiorite sample WL-31, with two grains showing $^{206}Pb-^{238}U$ age outliers (281.2 Ma for WL-31-1 and 264.8 Ma for WL-31-10), 20 analytical spots showed a tight concordant grouping, defining a weighted mean $^{206}Pb-^{238}U$ age of 254.7 ± 2.1 Ma (1σ, MSWD = 1.2), interpreted as the crystallization age of the granodiorite (Fig. 6d).

The result of one zircon was excluded from the age calculation owing to the discordant values for the MME sample WL-34. The remaining 20 points plot along a Concordia line with $^{206}Pb-^{238}U$ ages varying from 248.5 to 260.8 Ma, yielding a weighted mean $^{206}Pb-^{238}U$ age of 253.9 ± 2.7 Ma (1σ), which is interpreted as the MME emplacement age. This crystallization age is identical, within acceptable error, to that of the host granodiorites obtained in this study (Fig. 6e).

4.b. In situ *zircon Hf isotopes*

Table 2 lists the zircon Hf isotope data for the Late Jurassic W-bearing granitoids (samples WL-16 and WL-24), late Permian barren granitoids (samples WL-28 and WL-31) and MMEs (sample WL-34). The results show that zircon grains from the Late Jurassic W-bearing granitoids (WL-16 and WL-24) have relatively consistent Hf isotopic compositions, with initial $^{176}Hf/^{177}Hf$ ratios ranging from 0.282512 to 0.282618, $\epsilon_{Hf}(t)$ values from −6.0 to −2.1, and two-stage model ages (T_{DM2}) varying from 1338 to 1583 Ma. The zircon grains separated from the late Permian barren granitoids (samples WL-28 and WL-31) yielded $^{176}Hf/^{177}Hf$ values of 0.282631–0.282711, corresponding to $\epsilon_{Hf}(t)$ values between +0.4 and +3.6 and T_{DM2} ages of 1067–1256 Ma. The initial $^{176}Hf/^{177}Hf$ ratios of zircon from the MMEs (sample WL-34) vary from 0.282623 to 0.282720. The calculated $\epsilon_{Hf}(t)$ values range from +0.1 to +3.5, with corresponding T_{DM1} and T_{DM2} ages of 778–903 Ma and 1061–1272 Ma, respectively. On a $\epsilon_{Hf}(t)$ versus age diagram (Fig. 7), all analysed spots from the Late Jurassic W-bearing granitoids plot below the chondritic uniform reservoir (CHUR) line. In contrast, samples from the late Permian barren granitoids all extend between the depleted mantle and CHUR line, similar to zircons from the Phanerozoic igneous rocks found in the eastern CAOB. The MME samples conformably plot between the depleted mantle and CHUR line.

4.c. Whole-rock major- and trace-element compositions

Table 3 lists the whole-rock major- and trace-element data for the late Permian barren granodiorite and hosting MMEs, as well as the Late Jurassic W-bearing monzogranite and granite porphyry samples.

The late Permian barren granodiorites have the following major elemental concentrations: $SiO_2 = 67.24–70.72$ wt %, $Al_2O_3 = 14.30–15.46$ wt %, total alkalis $(K_2O + Na_2O) = 5.91–6.45$ wt %, $Fe_2O_3^T = 3.08–4.41$ wt %, CaO = 2.65–3.98 wt %, $P_2O_5 = 0.08–0.11$ wt % and $TiO_2 = 0.29–0.38$ wt %. Their MgO content is 1.06–1.60 wt %, with Mg no. values of 40.54–41.82. Comparatively, the MMEs in the granodiorite have the following major elemental concentrations: $SiO_2 = 55.53–58.03$ wt %, $Al_2O_3 = 16.76–17.08$ wt %, total alkalis $(K_2O + Na_2O) = 5.96–6.57$ wt %, $Fe_2O_3^T = 8.21–9.16$ wt %, CaO = 5.04–5.33 wt %, $P_2O_5 = 0.23–0.25$ wt % and $TiO_2 = 0.77–0.97$ wt %. The MMEs have high MgO contents of 3.27–3.66 wt % and Mg no. values of 44.10–44.18. The Late Jurassic W-bearing monzogranite and granite porphyry have the following major elemental concentrations: $SiO_2 = 73.73–75.65$ wt %, $Al_2O_3 = 12.86–13.82$ wt %, total alkalis $(K_2O + Na_2O) = 8.40–9.14$ wt %, $Fe_2O_3^T = 1.08–1.46$ wt %,

Table 1. Zircon LA-ICP-MS U–Pb dating data for the Narenwula complex and MMEs

Sample No.	Th (ppm)	U (ppm)	Pb (ppm)	Th/U	$^{207}Pb/^{206}Pb$ Ratio	1σ	$^{207}Pb/^{235}U$ Ratio	1σ	$^{206}Pb/^{238}U$ Ratio	1σ	$^{207}Pb–^{206}Pb$ Ages (Ma)	1σ	$^{207}Pb–^{235}U$ Ages (Ma)	1σ	$^{206}Pb–^{238}U$ Ages (Ma)	1σ
Granite porphyry																
WL-16-01	493.7	332.3	23.0	1.49	0.04626	0.00673	0.15028	0.02177	0.02440	0.00057	13.1	314.8	142.2	19.2	155.4	3.6
WL-16-02	188.2	231.3	10.4	0.81	0.04685	0.00755	0.14892	0.02407	0.02325	0.00056	42.7	344.4	141.0	21.3	148.1	3.5
WL-16-03	753.1	360.9	33.4	2.09	0.04664	0.00834	0.14847	0.02649	0.02370	0.00045	31.6	381.4	140.6	23.4	151.0	2.8
WL-16-04	271.4	382.7	15.7	0.71	0.05562	0.00298	0.18598	0.00929	0.02461	0.00050	438.9	115.7	173.2	8.0	156.7	3.1
WL-16-05	244.8	275.2	13.6	0.89	0.04955	0.00311	0.15911	0.00981	0.02356	0.00045	172.3	150.9	149.9	8.6	150.1	2.8
WL-16-06	238.9	454.0	15.8	0.53	0.05350	0.00256	0.17543	0.00798	0.02402	0.00046	350.1	107.4	164.1	6.9	153.0	2.9
WL-16-07	398.1	774.1	25.5	0.51	0.04876	0.00188	0.15852	0.00614	0.02350	0.00036	200.1	95.4	149.4	5.4	149.7	2.3
WL-16-08	367.6	447.1	19.7	0.82	0.05204	0.00282	0.16626	0.00833	0.02356	0.00048	287.1	119.4	156.2	7.3	150.1	3.0
WL-16-09	216.2	185.0	11.3	1.17	0.05437	0.00482	0.17314	0.01332	0.02398	0.00065	387.1	201.8	162.1	11.5	152.8	4.1
WL-16-10	136.0	188.2	8.0	0.72	0.04952	0.00435	0.15921	0.01201	0.02338	0.00056	172.3	192.6	150.0	10.5	149.0	3.5
WL-16-11	276.8	255.5	14.8	1.08	0.05232	0.00361	0.16756	0.00953	0.02332	0.00047	298.2	125.0	157.3	8.3	148.6	3.0
WL-16-12	319.7	362.7	17.8	0.88	0.05030	0.00291	0.16222	0.00862	0.02392	0.00045	209.3	130.5	152.6	7.5	152.4	2.8
WL-16-13	261.4	396.8	15.4	0.66	0.04958	0.00230	0.16032	0.00748	0.02350	0.00046	176.0	107.4	151.0	6.5	149.7	2.9
WL-16-14	326.2	424.4	18.9	0.77	0.04897	0.00245	0.15834	0.00761	0.02358	0.00040	146.4	113.9	149.3	6.7	150.2	2.5
WL-16-15	192.0	291.5	12.4	0.66	0.05364	0.00295	0.17653	0.00902	0.02444	0.00044	366.7	124.1	165.1	7.8	155.7	2.8
WL-16-16	205.8	271.6	11.8	0.76	0.05224	0.00304	0.17368	0.00916	0.02429	0.00052	294.5	133.3	162.6	7.9	154.7	3.3
WL-16-17	233.0	295.0	13.5	0.79	0.04719	0.00274	0.15295	0.00864	0.02350	0.00045	57.5	133.3	144.5	7.6	149.7	2.9
WL-16-18	208.8	179.3	10.4	1.16	0.05395	0.00444	0.16729	0.01182	0.02258	0.00053	368.6	185.2	157.1	10.3	143.9	3.3
Monzogranite																
WL-24-01	558.6	727.3	32.4	0.77	0.05105	0.00227	0.16242	0.00676	0.02328	0.00038	242.7	71.3	152.8	5.9	148.4	2.4
WL-24-02	615.6	425.8	32.7	1.45	0.05314	0.00295	0.17716	0.00932	0.02366	0.00044	344.5	123.1	165.6	8.0	150.7	2.8
WL-24-03	423.2	677.0	24.6	0.63	0.05182	0.00206	0.16811	0.00668	0.02359	0.00039	276.0	90.7	157.8	5.8	150.3	2.5
WL-24-04	342.3	517.6	19.5	0.66	0.05003	0.00241	0.16057	0.00748	0.02334	0.00040	194.5	112.9	151.2	6.5	148.8	2.5
WL-24-05	517.4	278.4	22.8	1.86	0.04886	0.00338	0.15313	0.01057	0.02306	0.00048	142.7	151.8	144.7	9.3	147.0	3.0
WL-24-06	297.7	261.9	15.2	1.14	0.04697	0.00336	0.15309	0.01017	0.02345	0.00042	55.7	153.7	144.6	9.0	149.4	2.7
WL-24-07	198.7	172.2	9.6	1.15	0.05258	0.00515	0.17006	0.01303	0.02325	0.00057	309.3	221.3	159.5	11.3	148.1	3.6
WL-24-08	227.7	251.8	12.4	0.90	0.05333	0.00382	0.16285	0.01066	0.02331	0.00053	342.7	162.9	153.2	9.3	148.6	3.4
WL-24-09	542.0	822.4	30.3	0.66	0.05171	0.00195	0.15876	0.00568	0.02215	0.00032	272.3	91.7	149.6	5.0	141.2	2.0
WL-24-10	351.8	343.9	17.7	1.02	0.04739	0.00274	0.15383	0.00786	0.02335	0.00044	77.9	133.3	145.3	6.9	148.8	2.8
WL-24-11	318.0	539.5	17.9	0.59	0.04442	0.00199	0.14253	0.00630	0.02332	0.00036	309.3	221.3	135.3	5.6	148.6	2.2
WL-24-12	223.7	272.8	13.1	0.82	0.04835	0.00423	0.14890	0.01215	0.02322	0.00049	116.8	192.6	140.9	10.7	148.0	3.1

(Continued)

Table 1. (*Continued*)

Sample No.	Th (ppm)	U (ppm)	Pb (ppm)	Th/U	$^{207}Pb/^{206}Pb$ Ratio	1σ	$^{207}Pb/^{235}U$ Ratio	1σ	$^{206}Pb/^{238}U$ Ratio	1σ	$^{207}Pb–^{206}Pb$ Ages (Ma)	1σ	$^{207}Pb–^{235}U$ Ages (Ma)	1σ	$^{206}Pb–^{238}U$ Ages (Ma)	1σ
WL-24-13	287.4	213.7	15.1	1.34	0.05124	0.00535	0.16911	0.01621	0.02415	0.00064	250.1	225.9	158.6	14.1	153.8	4.0
WL-24-14	693.2	812.7	35.4	0.85	0.04675	0.00468	0.14273	0.01389	0.02251	0.00036	35.3	225.9	135.5	12.3	143.5	2.2
WL-24-15	552.7	543.6	28.3	1.02	0.04614	0.00513	0.14624	0.01663	0.02280	0.00038	400.1	146.3	138.6	14.7	145.3	2.4
Granodiorite																
WL-28-01	338.4	420.7	33.0	0.80	0.05461	0.00223	0.30548	0.01222	0.04036	0.00061	398.2	92.6	270.7	9.5	255.0	3.8
WL-28-02	208.0	333.8	24.4	0.62	0.05612	0.00261	0.32324	0.01352	0.04201	0.00062	457.5	108.3	284.4	10.4	265.3	3.8
WL-28-03	252.7	410.2	26.8	0.62	0.05541	0.00229	0.30384	0.01176	0.03987	0.00070	427.8	86.1	269.4	9.2	252.0	4.4
WL-28-04	280.2	409.6	28.6	0.68	0.04933	0.00284	0.28482	0.01518	0.04018	0.00079	164.9	133.3	254.5	12.0	253.9	4.9
WL-28-05	165.4	276.8	19.0	0.60	0.05230	0.00287	0.31329	0.01555	0.04172	0.00075	298.2	125.9	276.7	12.0	263.5	4.7
WL-28-06	273.4	353.1	26.8	0.77	0.05296	0.00291	0.29248	0.01476	0.04030	0.00072	327.8	128.7	260.5	11.6	254.7	4.4
WL-28-07	288.2	413.3	29.5	0.70	0.05402	0.00268	0.30403	0.01327	0.04099	0.00063	372.3	111.1	269.5	10.3	259.0	3.9
WL-28-08	353.2	505.7	35.0	0.70	0.05401	0.00186	0.30659	0.01002	0.04066	0.00060	372.3	77.8	271.5	7.8	256.9	3.7
WL-28-09	151.1	278.9	16.2	0.54	0.05170	0.00247	0.28841	0.01296	0.04019	0.00074	272.3	111.1	257.3	10.2	254.0	4.6
WL-28-10	241.9	344.6	23.4	0.70	0.05199	0.00233	0.29416	0.01325	0.04039	0.00070	283.4	97.2	261.8	10.4	255.3	4.4
WL-28-11	234.2	375.7	24.6	0.62	0.04913	0.00243	0.27428	0.01253	0.04033	0.00061	153.8	114.8	246.1	10.0	254.9	3.8
WL-28-12	214.6	339.1	22.2	0.63	0.05334	0.00238	0.30313	0.01313	0.04097	0.00066	342.7	101.8	268.8	10.2	258.8	4.1
WL-28-13	198.2	327.1	19.7	0.61	0.05280	0.00234	0.29391	0.01196	0.04054	0.00069	320.4	100.0	261.6	9.4	256.2	4.3
WL-28-14	170.8	287.1	18.4	0.59	0.05354	0.00237	0.30574	0.01396	0.04102	0.00067	353.8	97.2	270.9	10.9	259.1	4.2
WL-28-15	242.9	348.9	24.4	0.70	0.05318	0.00202	0.30269	0.01106	0.04099	0.00055	344.5	82.4	268.5	8.6	259.0	3.4
WL-28-16	220.2	319.4	23.2	0.69	0.05404	0.00273	0.31075	0.01478	0.04165	0.00065	372.3	114.8	274.8	11.4	263.1	4.1
WL-28-17	199.4	314.2	22.1	0.63	0.05470	0.00242	0.32086	0.01434	0.04228	0.00068	398.2	98.1	282.6	11.0	267.0	4.2
WL-28-18	182.2	294.4	19.5	0.62	0.05495	0.00244	0.31144	0.01298	0.04149	0.00067	409.3	98.1	275.3	10.1	262.0	4.1
WL-31-01	251.1	341.0	29.0	0.74	0.05509	0.00240	0.33844	0.01417	0.04458	0.00084	416.7	93.5	296.0	10.7	281.2	5.2
WL-31-02	417.6	561.2	44.6	0.74	0.05502	0.00203	0.31974	0.01062	0.04246	0.00073	413.0	83.3	281.7	8.2	268.0	4.5
WL-31-03	282.9	426.0	28.1	0.66	0.05438	0.00182	0.31139	0.00960	0.04156	0.00061	387.1	75.9	275.3	7.4	262.5	3.8
WL-31-04	372.2	470.1	36.7	0.79	0.05322	0.00206	0.29645	0.01120	0.04007	0.00052	338.9	88.9	263.6	8.8	253.3	3.3
WL-31-05	318.0	381.4	30.2	0.83	0.05470	0.00231	0.29514	0.01113	0.03954	0.00064	466.7	99.1	262.6	8.7	250.0	4.0
WL-31-06	159.1	277.6	17.4	0.57	0.05660	0.00276	0.31513	0.01467	0.04070	0.00068	476.0	112.0	278.2	11.3	257.2	4.2
WL-31-07	143.2	247.0	17.7	0.58	0.05381	0.00308	0.29315	0.01515	0.03961	0.00073	361.2	129.6	261.0	11.9	250.4	4.5
WL-31-08	271.1	358.8	26.1	0.76	0.05127	0.00197	0.28218	0.01125	0.03961	0.00065	253.8	88.9	252.4	8.9	250.4	4.0
WL-31-09	339.7	398.7	33.0	0.85	0.05116	0.00206	0.28564	0.01082	0.04066	0.00068	255.6	92.6	255.1	8.5	256.9	4.2
WL-31-10	156.8	247.8	16.6	0.63	0.05187	0.00325	0.29473	0.01440	0.04193	0.00098	279.7	144.4	262.3	11.3	264.8	6.0
WL-31-11	250.1	338.8	23.3	0.74	0.05268	0.00232	0.28961	0.01303	0.03970	0.00068	322.3	100.0	258.2	10.3	251.0	4.2

(*Continued*)

Table 1. (*Continued*)

Sample No.	Th (ppm)	U (ppm)	Pb (ppm)	Th/U	$^{207}Pb/^{206}Pb$ Ratio	1σ	$^{207}Pb/^{235}U$ Ratio	1σ	$^{206}Pb/^{238}U$ Ratio	1σ	$^{207}Pb-^{206}Pb$ Ages (Ma)	1σ	$^{207}Pb-^{235}U$ Ages (Ma)	1σ	$^{206}Pb-^{238}U$ Ages (Ma)	1σ
WL-31-12	210.2	323.4	22.2	0.65	0.05312	0.00245	0.29517	0.01355	0.04032	0.00071	344.5	100.9	262.6	10.6	254.8	4.4
WL-31-13	231.1	325.0	23.2	0.71	0.05755	0.01410	0.31316	0.07378	0.04004	0.00424	522.3	453.7	276.6	57.1	253.1	26.3
WL-31-14	368.3	509.2	37.1	0.72	0.05710	0.01208	0.32558	0.06628	0.04152	0.00380	494.5	411.1	286.2	50.8	262.3	23.5
WL-31-15	130.5	237.3	14.4	0.55	0.05472	0.01003	0.30587	0.05407	0.04053	0.00318	466.7	299.7	271.0	42.0	256.1	19.7
WL-31-16	255.5	348.8	24.5	0.73	0.05415	0.00824	0.29514	0.04302	0.04005	0.00257	376.0	311.1	262.6	33.7	253.2	15.9
WL-31-17	212.0	334.9	22.2	0.63	0.05113	0.00620	0.28424	0.03364	0.03989	0.00206	255.6	250.0	254.0	26.6	252.1	12.8
WL-31-18	260.4	366.6	24.3	0.71	0.05654	0.00230	0.31198	0.01216	0.03996	0.00060	472.3	86.1	275.7	9.4	252.6	3.7
WL-31-19	198.5	322.9	21.8	0.61	0.05326	0.00260	0.30904	0.01331	0.04150	0.00071	338.9	111.1	273.4	10.3	262.1	4.4
WL-31-20	197.0	322.5	20.0	0.61	0.05644	0.00253	0.31122	0.01447	0.03959	0.00064	477.8	98.1	275.1	11.2	250.3	4.0
WL-31-21	405.5	454.1	38.1	0.89	0.05443	0.00218	0.30040	0.01168	0.03998	0.00067	387.1	90.7	266.7	9.1	252.7	4.2
WL-31-22	193.2	284.7	19.8	0.68	0.05084	0.00270	0.28096	0.01456	0.03983	0.00065	235.3	122.2	251.4	11.5	251.8	4.0
MMEs																
WL-34-01	238.8	336.9	24.7	0.71	0.05215	0.00229	0.29899	0.01132	0.04078	0.00063	300.1	101.8	265.6	8.9	257.7	3.9
WL-34-02	298.9	426.5	30.7	0.70	0.05071	0.00230	0.28551	0.01270	0.04064	0.00062	227.8	103.7	255.0	10.0	256.8	3.8
WL-34-03	500.1	520.3	44.1	0.96	0.05160	0.00202	0.28960	0.01087	0.04054	0.00061	333.4	88.9	258.2	8.6	256.1	3.8
WL-34-04	163.0	222.4	17.2	0.73	0.05152	0.00277	0.28464	0.01324	0.04065	0.00071	264.9	91.7	254.3	10.5	256.9	4.4
WL-34-05	391.3	457.1	36.4	0.86	0.05033	0.00192	0.28227	0.01039	0.04040	0.00055	209.3	88.9	252.5	8.2	255.3	3.4
WL-34-06	316.9	394.2	31.6	0.80	0.05023	0.00214	0.27965	0.01169	0.04010	0.00064	205.6	100.0	250.4	9.3	253.5	3.9
WL-34-07	324.9	408.7	33.9	0.79	0.05226	0.00299	0.28905	0.01336	0.03920	0.00157	298.2	129.6	257.8	10.5	247.9	9.7
WL-34-08	689.9	705.6	61.2	0.98	0.04803	0.00175	0.26529	0.00960	0.03955	0.00051	101.9	85.2	238.9	7.7	250.0	3.2
WL-34-09	347.0	408.9	32.9	0.85	0.05246	0.00431	0.27897	0.01970	0.03931	0.00069	305.6	188.9	249.8	15.6	248.5	4.3
WL-34-10	653.2	588.2	61.8	1.11	0.05081	0.00210	0.28118	0.01084	0.03987	0.00061	231.6	62.0	251.6	8.6	252.0	3.8
WL-34-11	119.2	216.7	15.2	0.55	0.04938	0.00269	0.27053	0.01417	0.03952	0.00075	164.9	125.9	243.1	11.3	249.8	4.7
WL-34-12	274.2	397.5	28.2	0.69	0.05060	0.00201	0.28147	0.01097	0.03992	0.00056	233.4	97.2	251.8	8.7	252.3	3.5
WL-34-13	292.0	381.3	28.8	0.77	0.05052	0.00223	0.27931	0.01189	0.03988	0.00063	220.4	97.2	250.1	9.4	252.1	3.9
WL-34-14	203.0	401.9	25.3	0.51	0.05457	0.00353	0.29951	0.01182	0.04109	0.00076	394.5	178.7	266.0	9.2	259.6	4.7
WL-34-15	402.7	428.8	39.3	0.94	0.05143	0.00209	0.29453	0.01153	0.04126	0.00064	261.2	92.6	262.1	9.0	260.6	4.0
WL-34-16	362.0	424.2	34.9	0.85	0.05040	0.00252	0.28288	0.01511	0.03998	0.00055	213.0	112.0	252.9	12.0	252.7	3.4
WL-34-17	175.4	267.9	18.2	0.65	0.05166	0.00334	0.28512	0.01826	0.03982	0.00065	333.4	145.4	254.7	14.4	251.7	4.0
WL-34-18	229.5	315.9	22.0	0.73	0.05307	0.00229	0.29677	0.01208	0.04054	0.00064	331.5	98.1	263.9	9.5	256.2	4.0
WL-34-19	649.7	680.6	60.2	0.95	0.05164	0.00186	0.28793	0.01059	0.03988	0.00053	333.4	83.3	256.9	8.3	252.1	3.3
WL-34-20	129.9	223.0	14.1	0.58	0.05439	0.00244	0.30934	0.01410	0.04091	0.00074	387.1	100.0	273.7	10.9	258.5	4.6
WL-34-21	224.8	283.8	23.7	0.79	0.05620	0.00224	0.32031	0.01233	0.04128	0.00072	461.2	88.9	282.1	9.5	260.8	4.5
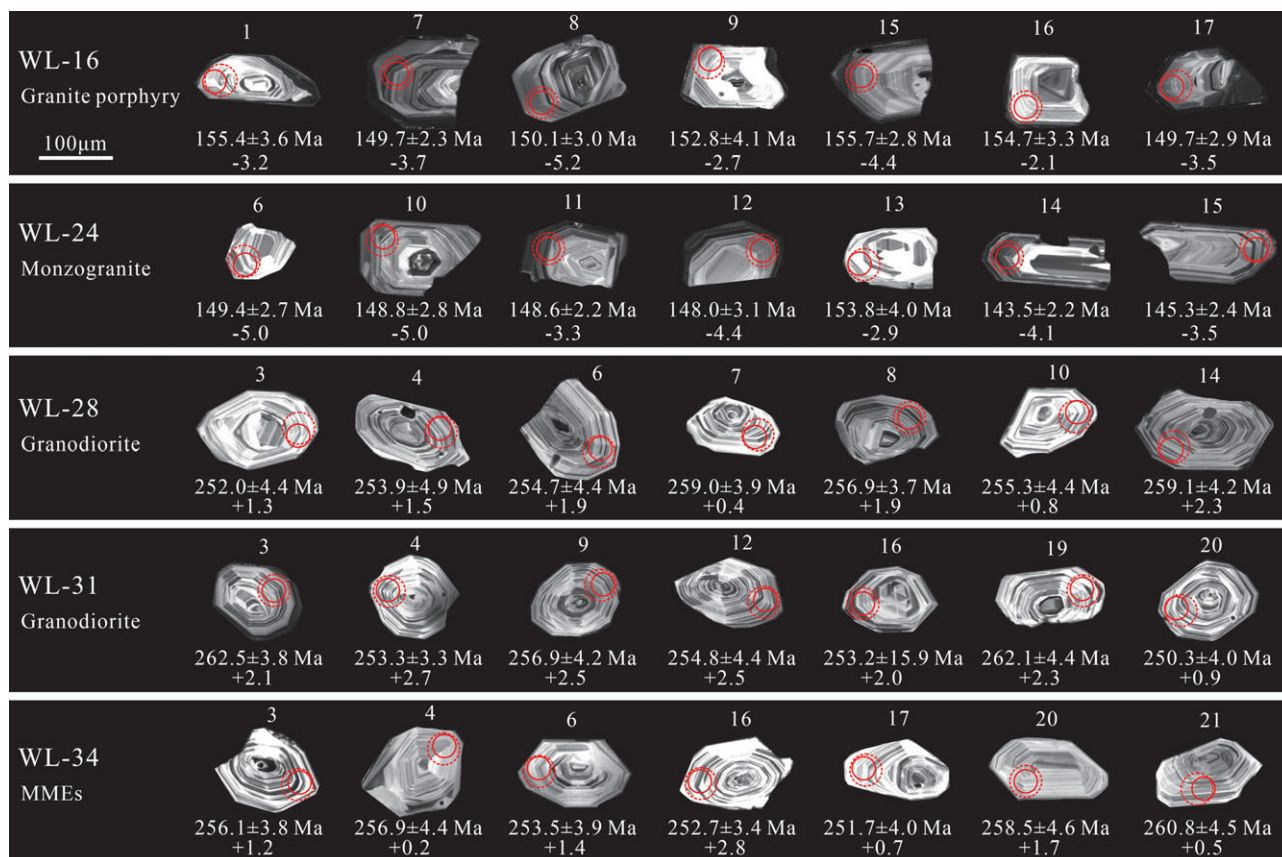
Fig. 5. (Colour online) CL images of selected zircons from the representative granitic intrusions and MMEs from the Narenwula complex. Red solid circles are the locations of U–Pb analyses and dashed circles are the locations of Hf analyses.

CaO = 0.46–0.79 wt %, P_2O_5 = 0.02–0.05 wt % and TiO_2 = 0.09–0.15 wt %. They have low MgO contents of 0.12–0.21 wt % and Mg no. values of 18.04–22.17.

On a total alkalis versus SiO_2 diagram (Middlemost, 1994), most monzogranite and granite porphyry samples plot in the granite field (Fig. 8a). The granodiorite samples plot in the granodiorite field, while the MMEs plot in the diorite and monzodiorite fields (Fig. 8a). On a K_2O versus SiO_2 diagram (Peccerillo & Taylor, 1976), the MMEs and granodiorite plot in the calc-alkaline field while the monzogranite and granite porphyry plot in the high-K calc-alkaline to shoshonite fields (Fig. 8b). On an A/NK (molar $Al_2O_3/(Na_2O + K_2O)$) versus A/CNK (molar $Al_2O_3/(CaO + Na_2O + K_2O)$) diagram (Maniar & Piccoli, 1989), all MME samples can be classified as metaluminous rocks, with A/CNK ratios of 0.91–0.92 (Fig. 8c). Comparatively, most granodiorite sample spots plot near the weakly peraluminous field, with A/CNK ratios of 0.99–1.12 (Fig. 8c). All monzogranite and granite porphyry samples plot in the weakly peraluminous field, with A/CNK ratios of 1.03–1.11 (Fig. 8c).

On a chondrite-normalized rare earth element (REE) diagram, all MMEs, granodiorite, monzogranite and granite porphyry samples exhibit light REE (LREE) enrichment and heavy REE (HREE) depletion, with $(La/Yb)_N$ ratios of 5.59–6.19, 11.67–14.03, 6.79–16.56 and 9.65–14.99, respectively (Fig. 9a; Table 3). The granodiorites show slight negative Eu anomalies (Eu/Eu* = 0.87–0.98) while the MMEs have moderate negative Eu anomalies (Eu/Eu* = 0.66). Comparatively, the monzogranite and granite porphyry display significant negative Eu anomalies

(Eu/Eu* = 0.28–0.52) (Fig. 9a; Table 3). On a primitive-mantle-normalized trace-element diagram (Sun & McDonough, 1989), all granodiorite and MME samples are characterized by enrichment in large-ion lithophile elements (LILEs; e.g. Rb, Th, K and Pb), and depletion in high field strength elements (HFSEs; e.g. Nb, Ta, P and Ti) (Fig. 9b). Comparatively, most monzogranite and granite porphyry samples exhibit stronger negative Ba, Sr, P and Ti anomalies than the granodiorite and MMEs (Fig. 9b).

5. Discussion

5.a. Timing of magmatism and associated W mineralization

Constraints on the timing and duration of ore-related magmatic events are crucial for understanding ore deposit formation, from both academic and economic viewpoints (Stein, 2014). In the study area, the barren granodiorites, which yield emplacement ages of 258.5–254.7 Ma (late Permian), record a pre-mineralization magmatic event. The W-bearing monzogranite and granite porphyry were emplaced after the barren granodiorite, yielding zircon U–Pb ages of 148.1 ± 2.1 Ma and 149.8 ± 2.7 Ma, respectively. Considering the Mesozoic extensive and intense W mineralization event in NE China, W mineralization at Narenwula was not an isolated event. Previous geochronological studies reported a wide range of ages for the W-related granitic intrusions in NE China. The LXZB experienced widespread W-related tectonomagmatic events during Early Triassic and Early and Middle Jurassic times, with the emplacement of granitoids such as the Yangjingou
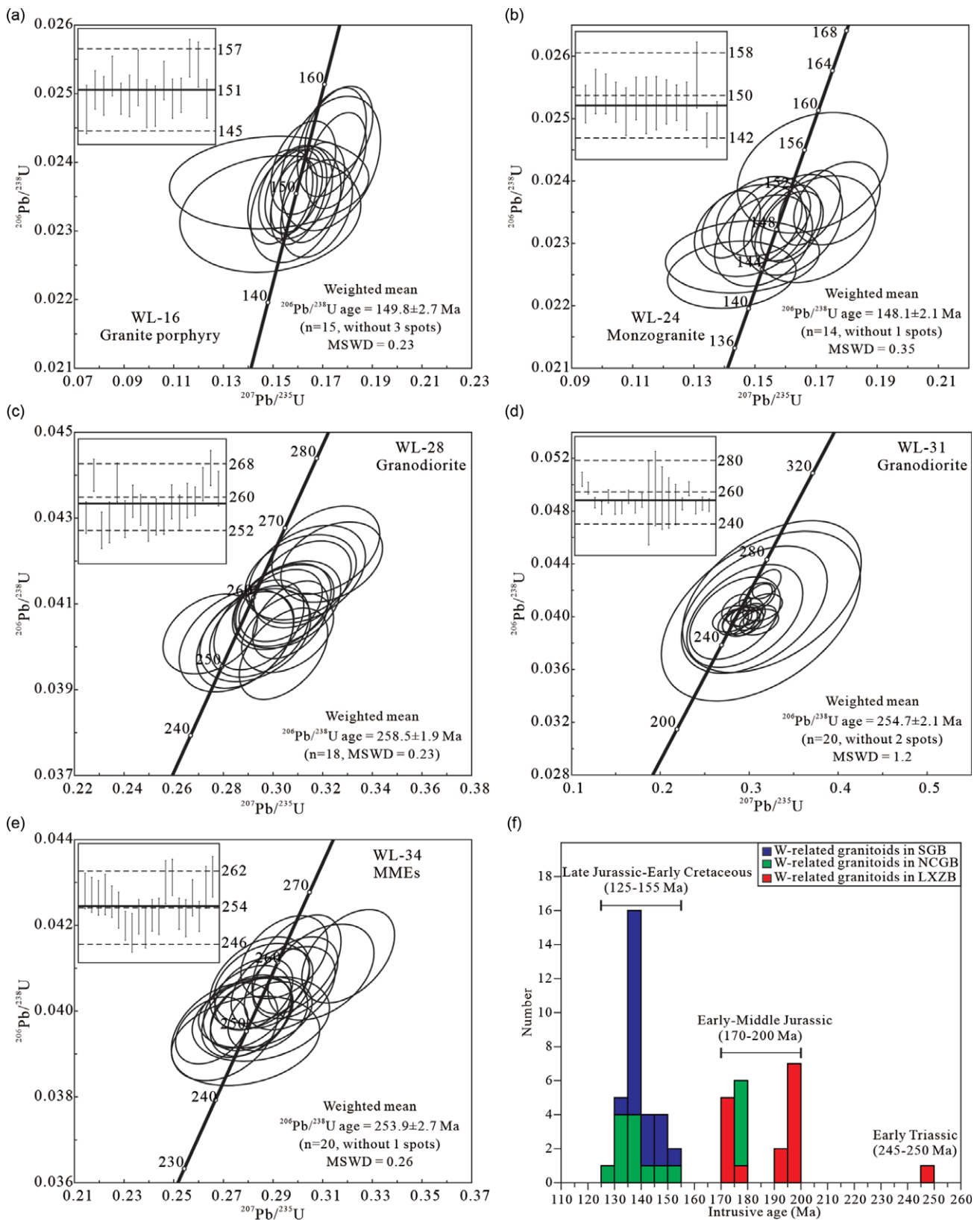
Fig. 6. (Colour online) (a–e) Zircon U–Pb Concordia diagrams for the granitoids and MMEs from the Narenwula complex. (f) Histogram and probability plot of the zircon U–Pb ages of W-related granitoids in NE China. Abbreviations: NCGB – northern and central Great Xing'an Range belt; SGB – southern Great Xing'an Range belt; LXZB – Lesser Xing'an–Zhangguangcai Range belt. Data sources are listed in online Supplementary Material Table S1.

Table 2. Hf isotopic compositions of zircons from the Narenwula complex and MMEs

Sample No.	^{176}Hf/^{177}Hf	2σ	^{176}Lu/^{177}Hf	2σ	^{176}Yb/^{177}Hf	2σ	Age (Ma)	$\epsilon_{Hf}(0)$	$\epsilon_{Hf}(t)$	T_{DM1}	T_{DM2}	$f_{Lu/Hf}$
Granite porphyry												
WL-16-01	0.282587	0.000018	0.001136	0.000011	0.035439	0.000226	155	−6.5	−3.2	944	1409	−0.97
WL-16-02	0.282588	0.000014	0.000660	0.000011	0.022137	0.000353	148	−6.5	−3.3	931	1409	−0.98
WL-16-03	0.282577	0.000014	0.001099	0.000036	0.037884	0.001370	151	−6.9	−3.7	957	1434	−0.97
WL-16-04	0.282568	0.000019	0.000824	0.000013	0.026219	0.000298	157	−7.2	−3.9	964	1451	−0.98
WL-16-05	0.282512	0.000021	0.001248	0.000010	0.040115	0.000279	150	−9.2	−6.0	1054	1583	−0.96
WL-16-06	0.282574	0.000015	0.001047	0.000009	0.031898	0.000252	153	−7.0	−3.7	960	1439	−0.97
WL-16-07	0.282577	0.000012	0.000995	0.000011	0.033832	0.000206	150	−6.9	−3.7	956	1436	−0.97
WL-16-08	0.282536	0.000015	0.001184	0.000018	0.039218	0.000492	150	−8.4	−5.2	1019	1529	−0.96
WL-16-09	0.282602	0.000014	0.000732	0.000010	0.024861	0.000207	153	−6.0	−2.7	914	1376	−0.98
WL-16-10	0.282544	0.000013	0.000664	0.000006	0.022223	0.000057	149	−8.1	−4.9	993	1508	−0.98
WL-16-11	0.282592	0.000014	0.000875	0.000007	0.030374	0.000214	149	−6.4	−3.2	931	1402	−0.97
WL-16-12	0.282556	0.000014	0.000797	0.000005	0.028506	0.000239	152	−7.6	−4.4	980	1480	−0.98
WL-16-13	0.282536	0.000014	0.000926	0.000021	0.027896	0.000577	150	−8.4	−5.2	1011	1527	−0.97
WL-16-14	0.282594	0.000018	0.001121	0.000034	0.035098	0.001121	150	−6.3	−3.1	934	1398	−0.97
WL-16-15	0.282552	0.000013	0.000931	0.000016	0.030224	0.000324	156	−7.8	−4.4	988	1487	−0.97
WL-16-16	0.282618	0.000012	0.000751	0.000005	0.025482	0.000242	155	−5.4	−2.1	891	1338	−0.98
WL-16-17	0.282582	0.000011	0.000874	0.000017	0.027749	0.000475	150	−6.7	−3.5	945	1423	−0.97
WL-16-18	0.282616	0.000018	0.001099	0.000011	0.034897	0.000212	144	−5.5	−2.5	903	1352	−0.97
Monzogranite												
WL-24-01	0.282603	0.000016	0.001605	0.000024	0.051525	0.000714	148	−6.0	−2.9	934	1382	−0.95
WL-24-02	0.282574	0.000015	0.001262	0.000021	0.040957	0.000399	151	−7.0	−3.8	966	1442	−0.96
WL-24-03	0.282557	0.000013	0.000748	0.000012	0.024942	0.000255	150	−7.6	−4.4	977	1478	−0.98
WL-24-04	0.282534	0.000012	0.001025	0.000012	0.034762	0.000472	149	−8.4	−5.2	1016	1532	−0.97
WL-24-05	0.282556	0.000019	0.001615	0.000012	0.053315	0.000307	147	−7.6	−4.6	1000	1487	−0.95
WL-24-06	0.282540	0.000013	0.001129	0.000004	0.039516	0.000147	149	−8.2	−5.0	1011	1519	−0.97
WL-24-07	0.282617	0.000015	0.001346	0.000039	0.045183	0.001165	148	−5.5	−2.4	907	1348	−0.96
WL-24-08	0.282556	0.000013	0.000693	0.000008	0.022284	0.000337	149	−7.6	−4.4	977	1481	−0.98
WL-24-09	0.282578	0.000012	0.000764	0.000005	0.026004	0.000290	141	−6.9	−3.8	948	1437	−0.98
WL-24-10	0.282542	0.000014	0.001063	0.000027	0.036070	0.000719	149	−8.1	−5.0	1006	1514	−0.97
WL-24-11	0.282589	0.000013	0.000763	0.000011	0.025341	0.000262	149	−6.5	−3.3	933	1408	−0.98
WL-24-12	0.282558	0.000014	0.000840	0.000006	0.028411	0.000241	148	−7.6	−4.4	978	1478	−0.97
WL-24-13	0.282598	0.000015	0.001211	0.000025	0.038446	0.000541	154	−6.2	−2.9	931	1388	−0.96

(Continued)

Table 2. (*Continued*)

Sample No.	^{176}Hf/^{177}Hf	2σ	^{176}Lu/^{177}Hf	2σ	^{176}Yb/^{177}Hf	2σ	Age (Ma)	$\epsilon_{Hf}(0)$	$\epsilon_{Hf}(t)$	T_{DM1}	T_{DM2}	$f_{Lu/Hf}$
WL-24-14	0.282571	0.000016	0.001781	0.000036	0.058475	0.001116	144	−7.1	−4.1	984	1456	−0.95
WL-24-15	0.282587	0.000017	0.001107	0.000011	0.034888	0.000617	145	−6.6	−3.5	944	1417	−0.97
Granodiorite												
WL-28-01	0.282640	0.000014	0.001104	0.000008	0.033456	0.000190	255	−4.7	0.8	869	1231	−0.97
WL-28-02	0.282670	0.000014	0.001350	0.000015	0.036784	0.000211	265	−3.6	2.0	832	1161	−0.96
WL-28-03	0.282659	0.000014	0.001127	0.000005	0.034719	0.000147	252	−4.0	1.3	843	1192	−0.97
WL-28-04	0.282662	0.000016	0.001163	0.000006	0.033037	0.000153	254	−3.9	1.5	839	1183	−0.96
WL-28-05	0.282711	0.000016	0.001120	0.000008	0.030681	0.000189	264	−2.1	3.4	768	1067	−0.97
WL-28-06	0.282672	0.000016	0.001172	0.000010	0.031812	0.000253	255	−3.5	1.9	825	1161	−0.96
WL-28-07	0.282631	0.000013	0.001638	0.000053	0.043024	0.001370	259	−5.0	0.4	895	1256	−0.95
WL-28-08	0.282673	0.000013	0.001376	0.000032	0.042425	0.000901	257	−3.5	1.9	828	1159	−0.96
WL-28-09	0.282680	0.000015	0.001874	0.000042	0.054084	0.000874	254	−3.2	2.0	829	1151	−0.94
WL-28-10	0.282643	0.000012	0.001314	0.000007	0.039848	0.000214	255	−4.5	0.8	869	1226	−0.96
WL-28-11	0.282670	0.000014	0.000844	0.000008	0.022550	0.000296	255	−3.6	1.9	820	1161	−0.97
WL-28-12	0.282674	0.000013	0.000952	0.000003	0.027064	0.000123	259	−3.5	2.1	818	1152	−0.97
WL-28-13	0.282670	0.000014	0.001066	0.000008	0.031243	0.000204	256	−3.6	1.8	825	1163	−0.97
WL-28-14	0.282680	0.000014	0.001178	0.000022	0.032892	0.000600	259	−3.2	2.3	814	1140	−0.96
WL-28-15	0.282673	0.000014	0.001189	0.000006	0.033387	0.000111	259	−3.5	2.0	825	1157	−0.96
WL-28-16	0.282654	0.000019	0.001046	0.000008	0.028031	0.000181	263	−4.2	1.4	848	1195	−0.97
WL-28-17	0.282655	0.000015	0.001307	0.000043	0.035385	0.000934	267	−4.1	1.5	852	1194	−0.96
WL-28-18	0.282646	0.000014	0.000858	0.000007	0.023770	0.000124	262	−4.4	1.2	855	1211	−0.97
WL-31-01	0.282708	0.000014	0.001473	0.000006	0.044045	0.000116	281	−2.3	3.6	781	1069	−0.96
WL-31-02	0.282670	0.000013	0.001620	0.000021	0.049011	0.000862	268	−3.6	2.0	838	1162	−0.95
WL-31-03	0.282674	0.000012	0.001365	0.000019	0.040909	0.000519	263	−3.5	2.1	827	1154	−0.96
WL-31-04	0.282696	0.000015	0.001191	0.000016	0.033086	0.000573	253	−2.7	2.7	791	1107	−0.96
WL-31-05	0.282689	0.000014	0.001223	0.000012	0.034687	0.000318	250	−2.9	2.4	802	1126	−0.96
WL-31-06	0.282681	0.000017	0.001247	0.000007	0.033087	0.000308	257	−3.2	2.2	814	1140	−0.96
WL-31-07	0.282661	0.000013	0.000740	0.000004	0.020608	0.000149	250	−3.9	1.4	832	1185	−0.98
WL-31-08	0.282695	0.000015	0.001357	0.000024	0.039155	0.000557	250	−2.7	2.6	796	1113	−0.96
WL-31-09	0.282688	0.000017	0.001230	0.000014	0.034462	0.000516	257	−3.0	2.5	804	1124	−0.96
WL-31-10	0.282649	0.000014	0.001023	0.000017	0.029160	0.000442	265	−4.3	1.3	854	1204	−0.97
WL-31-11	0.282695	0.000018	0.001358	0.000009	0.033470	0.000224	251	−2.7	2.5	797	1114	−0.96
WL-31-12	0.282689	0.000015	0.001194	0.000016	0.032133	0.000168	255	−2.9	2.5	801	1122	−0.96

(*Continued*)

Table 2. (*Continued*)

Sample No.	^{176}Hf/^{177}Hf	2σ	^{176}Lu/^{177}Hf	2σ	^{176}Yb/^{177}Hf	2σ	Age (Ma)	$\epsilon_{Hf}(0)$	$\epsilon_{Hf}(t)$	T_{DM1}	T_{DM2}	$f_{Lu/Hf}$
WL-31-13	0.282649	0.000012	0.001102	0.000003	0.032040	0.000132	253	−4.3	1.0	856	1212	−0.97
WL-31-14	0.282687	0.000013	0.001461	0.000011	0.043236	0.000296	262	−3.0	2.5	811	1127	−0.96
WL-31-15	0.282679	0.000013	0.001113	0.000029	0.031476	0.000657	256	−3.3	2.1	814	1144	−0.97
WL-31-16	0.282677	0.000017	0.001324	0.000008	0.033071	0.000160	253	−3.3	2.0	821	1151	−0.96
WL-31-17	0.282658	0.000012	0.001443	0.000010	0.043991	0.000333	252	−4.0	1.3	852	1198	−0.96
WL-31-18	0.282677	0.000014	0.001248	0.000008	0.037857	0.000136	253	−3.4	2.0	820	1152	−0.96
WL-31-19	0.282679	0.000013	0.001169	0.000005	0.031721	0.000146	262	−3.3	2.3	816	1142	−0.96
WL-31-20	0.282649	0.000013	0.001352	0.000026	0.035732	0.000487	250	−4.3	0.9	862	1217	−0.96
WL-31-21	0.282692	0.000013	0.001480	0.000012	0.041203	0.000330	253	−2.8	2.5	803	1120	−0.96
WL-31-22	0.282684	0.000013	0.000948	0.000005	0.027820	0.000082	252	−3.1	2.3	803	1133	−0.97
MMEs												
WL-34-01	0.282648	0.000013	0.001323	0.000010	0.040541	0.000396	258	−4.4	1.1	862	1214	−0.96
WL-34-02	0.282651	0.000015	0.001228	0.000003	0.035421	0.000207	257	−4.3	1.2	856	1208	−0.96
WL-34-03	0.282653	0.000014	0.001310	0.000012	0.035929	0.000337	256	−4.2	1.2	856	1205	−0.96
WL-34-04	0.282623	0.000013	0.001089	0.000012	0.033216	0.000465	257	−5.3	0.2	893	1269	−0.97
WL-34-05	0.282649	0.000016	0.001300	0.000013	0.036705	0.000509	255	−4.4	1.0	861	1214	−0.96
WL-34-06	0.282659	0.000013	0.001111	0.000007	0.032179	0.000104	253	−4.0	1.4	842	1191	−0.97
WL-34-07	0.282650	0.000021	0.001431	0.000016	0.035557	0.000394	248	−4.3	0.9	863	1218	−0.96
WL-34-08	0.282663	0.000016	0.001317	0.000016	0.035851	0.000238	250	−3.9	1.4	841	1186	−0.96
WL-34-09	0.282669	0.000015	0.001476	0.000019	0.039930	0.000217	249	−3.6	1.6	836	1175	−0.96
WL-34-10	0.282671	0.000014	0.001223	0.000008	0.034173	0.000344	252	−3.6	1.8	827	1165	−0.96
WL-34-11	0.282660	0.000012	0.001105	0.000013	0.032854	0.000365	250	−4.0	1.3	841	1191	−0.97
WL-34-12	0.282659	0.000015	0.001238	0.000004	0.035580	0.000116	252	−4.0	1.3	845	1192	−0.96
WL-34-13	0.282703	0.000014	0.001318	0.000006	0.039490	0.000365	252	−2.5	2.9	785	1095	−0.96
WL-34-14	0.282668	0.000014	0.001390	0.000013	0.040759	0.000518	260	−3.7	1.8	836	1169	−0.96
WL-34-15	0.282720	0.000019	0.002195	0.000028	0.058585	0.000988	261	−1.8	3.5	778	1061	−0.93
WL-34-16	0.282698	0.000015	0.001049	0.000012	0.027791	0.000181	253	−2.6	2.8	786	1102	−0.97
WL-34-17	0.282641	0.000015	0.001097	0.000002	0.030705	0.000147	252	−4.6	0.7	867	1232	−0.97
WL-34-18	0.282624	0.000017	0.001572	0.000022	0.044525	0.000459	256	−5.2	0.1	903	1272	−0.95
WL-34-19	0.282671	0.000015	0.001908	0.000006	0.055827	0.000315	252	−3.6	1.7	843	1172	−0.94
WL-34-20	0.282664	0.000013	0.000875	0.000004	0.025140	0.000118	258	−3.8	1.7	830	1174	−0.97
WL-34-21	0.282629	0.000012	0.001226	0.000005	0.034199	0.000171	261	−5.1	0.5	887	1255	−0.96
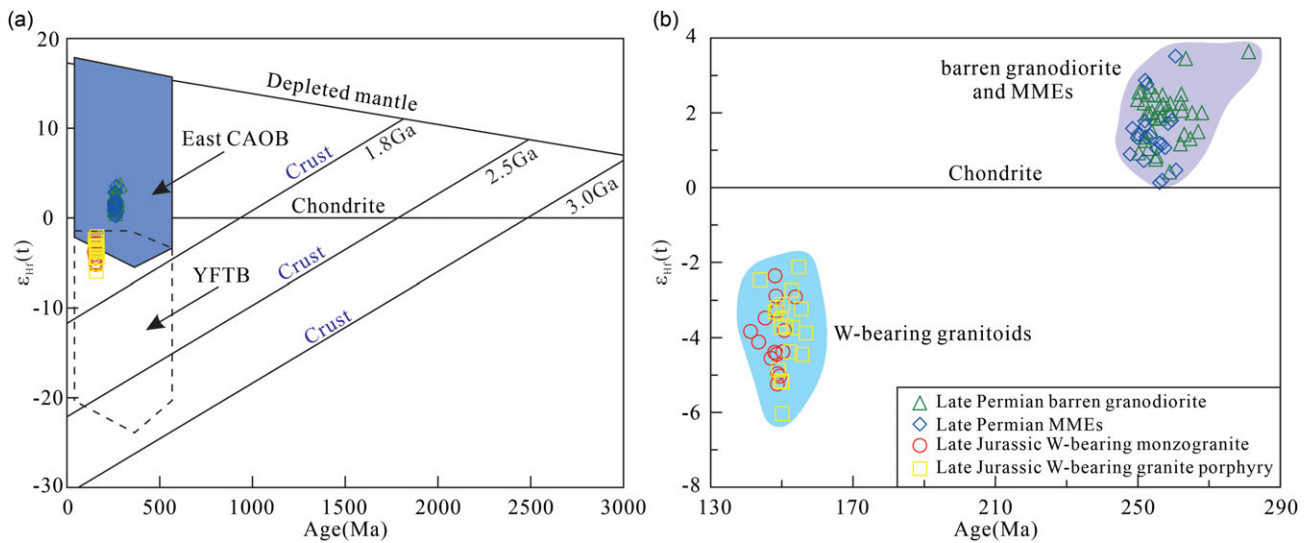
Fig. 7. (Colour online) ϵ_{Hf}(t) versus age (t) diagrams for granitic intrusions and MMEs from the Narenwula complex. Abbreviations: CAOB – Central Asian Orogenic Belt; YFTB – Yanshan Fold and Thrust Belt (Yang *et al.* 2006).

scheelite deposit (249.4 Ma) (Zhao, 2014), Cuihongshan W–Mo–Pb–Zn–(Fe–Cu) ore district (199.8–172.3 Ma) (Liu, 2009; Shao *et al.* 2011; Hu *et al.* 2014; Fei *et al.* 2018), Gongpengzi Cu–Zn–W polymetallic ore district (173.28 and 173.46 Ma) (Li, Y. S. *et al.* 2019), Xing'antun W–Mo ore district (195.4 Ma) (Wang *et al.* 2019), Sanjiazi scheelite ore district (172.4 Ma) (Ren *et al.* 2009) and Baishilizi W ore district (198.3 Ma) (Zhao, 2014). The W-related intrusive rocks in the NCGB mainly have Early–Middle Jurassic and Late Jurassic – Early Cretaceous ages, including granitoids dominated by monzogranite, quartz monzonite and biotite granite from the Honghuaerji W polymetallic ore district (179.4–178.6 Ma) (Xiang *et al.* 2014; Guo *et al.* 2015), biotite granite and biotite monzogranite from the Shamai W ore district (153.0–139.1 Ma) (Jiang *et al.* 2016; Li *et al.* 2016), granite from the Weilianhe region (143 Ma) (Xiang *et al.* 2018), fine-grained granite, granite porphyry and monzogranite from the Wurinitu region (139.7–131.9 Ma) (Liu *et al.* 2011; Yang *et al.* 2016; Zhang *et al.* 2016), and biotite monzogranite and quartz porphyry from the Dayana W–Mo ore district (135–130 Ma) (Xiang *et al.* 2016). The timing of the late Mesozoic W-related granitic magmatism in the SGB mainly indicates a Late Jurassic – Early Cretaceous age, including granitoids dominated by granite porphyry from the Dongshanwan Mo–W ore district (142.2 and 151.4 Ma) (Zeng *et al.* 2015b; Zhang, X. B. *et al.* 2017), granite from the Xiaodonggou Mo–W ore district (142 Ma) (Qin *et al.* 2009; Zeng *et al.* 2010), quartz porphyry, monzogranite and granite from the Weilasituo Sn–W–Cu–Zn ore district (140–135.7 Ma) (Liu *et al.* 2016, 2018; Zhai *et al.* 2016; Zhu *et al.* 2016; Yang *et al.* 2019), and granite from the Sansheng W–Mo ore district (136 Ma) (Zhou, 2013) and the Daolundaba Cu–W–Sn ore district (135 Ma) (Chen *et al.* 2018).

To obtain a more comprehensive understanding of W-related granitic magmatism in NE China, we integrated the results obtained in this study with previously published zircon U–Pb ages to distinguish three periods of W-related granitic magmatism: Early Triassic, Early–Middle Jurassic and Late Jurassic – Early Cretaceous (online Supplementary Material Table S1; Fig. 6f). Early Triassic W-related granitoids, with isotopic ages of 250–245 Ma, rarely occur in the LXZB. Early–Middle Jurassic

W-related granitoids are widely distributed in the LXZB and scattered throughout the NCGB, ranging in age from 200 to 170 Ma. Late Jurassic – Early Cretaceous W-related granitoids are widely exposed in the SGB, whereas there are minor occurrences in the NCGB, with ages ranging from 155 to 125 Ma (Figs 1c, 6f). The Late Jurassic granitic magmatism and W mineralization in Narenwula are consistent with the regional Late Jurassic to Early Cretaceous W-related tectonomagmatic–hydrothermal events.

5.b. Petrogenesis of the MMEs and host granodiorite

5.b.1. MMEs

MMEs are commonly observed in calc-alkaline granitic plutons, and can provide crucial insights into the petrogenesis of the host plutons (Didier, 1973; Chappell, 1996; Barbarin, 2005; Li, R. *et al.* 2021). Four models have been proposed to interpret the genesis of MMEs in granitoids: (a) recrystallized and residual phase assemblages (Chappell *et al.* 1987; Chen *et al.* 1989; Chappell & White, 1992; White *et al.* 1999); (b) xenoliths of the surrounding rock (Maas *et al.* 1997; Bonin, 2004); (c) cognate mafic accumulation in the felsic host magma (Tindle & Pearce, 1983; Clemens & Wall, 1988; Dodge & Kistler, 1990; Collins *et al.* 2006), and (d) products of magma mixing between mafic components and felsic magma (Yang *et al.* 2004; Barbarin, 2005; Clemens & Stevens, 2012).

The MMEs from the granodiorite display a porphyritic or hypidiomorphic granular texture without metamorphic or sedimentary textures (Fig. 4d, e). All MMEs contain the same mineral assemblages as the host granodiorites, but with increased mafic and plagioclase components relative to other felsic components (Fig. 4d, e). These textual features and identical zircon U–Pb ages between the MMEs and host granodiorites provide evidence against a residual or xenolith origin. Additionally, the lack of cumulate textures in the MMEs indicates that they are not mafic mineral cumulates (Didier, 1973; Vernon, 2014). The MMEs show complex and diverse shapes: many are irregularly ellipsoidal with sharp contacts with the host granitoids, and show ductile deformation (Fig. 4a). This phenomenon can imply significant contrasts in both temperature and viscosity between the injected mafic and

Table 3. Major (wt %) and trace-element (ppm) compositions of the Narenwula complex and MMEs

Age (Ma)	148.1	148.1	148.1	148.1	148.1	148.1	149.8	149.8	149.8	149.8	149.8	149.8	258.5	258.5	254.7	254.7	253.9	253.9
Sample	WL-5	WL-19	WL-23	WL-25	WL-26-1	WL-27	WL-6	WL-7-2	WL-8-2	WL-17	WL-18	WL-26-2	WL-29	WL-30	WL-32-2	WL-32-3	WL-33-2	WL-34-2
Lithology			Monzogranite							Granite porphyry					Granodiorite			MMEs
SiO_2	74.55	73.77	74.78	73.73	75.65	75.48	75.03	74.97	74.65	74.32	74.89	74.55	70.72	68.32	67.24	68.43	58.03	55.53
Al_2O_3	13.64	13.64	13.52	13.82	12.86	12.92	13.14	13.16	13.52	13.64	13.42	13.58	14.30	15.02	15.46	15.00	16.76	17.08
$Fe_2O_3^T$	1.32	1.37	1.26	1.46	1.08	1.14	1.16	1.18	1.27	1.35	1.22	1.30	3.08	3.93	4.41	3.98	8.21	9.16
FeO^T	1.19	1.23	1.13	1.31	0.97	1.03	1.04	1.06	1.14	1.21	1.10	1.17	2.77	3.54	3.97	3.58	7.39	8.24
CaO	0.66	0.74	0.62	0.79	0.46	0.56	0.59	0.6	0.65	0.72	0.61	0.66	2.78	3.23	3.98	2.65	5.33	5.04
MgO	0.18	0.19	0.16	0.21	0.12	0.14	0.14	0.15	0.17	0.18	0.16	0.17	1.06	1.38	1.60	1.42	3.27	3.66
K_2O	5.05	5.49	5.21	5.39	4.87	4.76	4.94	5.09	5.09	4.99	4.98	4.97	3.10	2.64	2.40	3.15	1.96	2.48
Na_2O	3.48	3.65	3.56	3.73	3.67	3.65	3.53	3.39	3.31	3.55	3.44	3.57	3.35	3.30	3.51	3.14	4.00	4.09
TiO_2	0.13	0.14	0.12	0.15	0.09	0.09	0.09	0.09	0.12	0.14	0.10	0.13	0.29	0.36	0.38	0.34	0.77	0.97
MnO	0.04	0.04	0.04	0.03	0.05	0.05	0.03	0.04	0.03	0.05	0.04	0.04	0.07	0.09	0.09	0.08	0.19	0.21
P_2O_5	0.03	0.04	0.02	0.05	0.02	0.02	0.02	0.02	0.02	0.03	0.02	0.02	0.08	0.09	0.11	0.10	0.23	0.25
Mg no.	21.27	21.55	20.10	22.17	18.04	19.57	19.29	20.12	20.96	20.89	20.62	20.57	40.54	41.02	41.82	41.41	44.10	44.18
σ	2.31	2.71	2.42	2.71	2.23	2.18	2.24	2.25	2.23	2.33	2.22	2.31	1.50	1.39	1.44	1.56	2.36	3.44
A/NK	1.22	1.14	1.18	1.15	1.14	1.16	1.18	1.19	1.23	1.21	1.21	1.21	1.61	1.81	1.85	1.75	1.93	1.81
A/CNK	1.10	1.03	1.07	1.03	1.06	1.06	1.07	1.08	1.11	1.09	1.10	1.09	1.03	1.06	0.99	1.12	0.91	0.92
Na_2O/K_2O	0.69	0.66	0.68	0.69	0.75	0.77	0.71	0.67	0.65	0.71	0.69	0.72	1.08	1.25	1.46	1.00	2.04	1.65
$Na_2O + K_2O$	8.53	9.14	8.77	9.12	8.54	8.41	8.47	8.48	8.40	8.54	8.42	8.54	6.45	5.94	5.91	6.29	5.96	6.57
LOI	0.82	0.88	0.72	0.80	0.53	0.70	0.79	0.88	0.93	0.77	1.00	0.83	0.89	1.35	0.73	1.28	0.99	1.17
Total	100.05	100.08	99.96	99.74	99.73	97.79	99.91	100.13	99.92	99.87	100.19	98.33	99.35	99.27	98.87	100.94	100.70	100.53
La	39.30	39.70	40.70	47.10	33.70	44.70	28.80	31.40	23.40	34.50	34.60	26.20	23.30	23.40	27	20.50	20.90	23.90
Ce	84.80	73.70	80.50	92.20	66.30	88.30	63.30	69.30	53.50	78.30	73.80	54.90	47.00	48.40	52.50	38.40	49.20	56.50
Pr	7.72	7.43	7.82	9.94	6.67	8.83	5.49	6.80	4.51	7.67	7.54	5.85	3.97	4.44	4.97	3.98	6.22	6.59
Nd	24.40	22.30	24.40	31.00	20.30	27.10	16.20	21.60	14.80	25.40	24.50	18.20	12.30	14.30	15.70	13.10	23.10	24.10
Sm	4.65	3.70	4.65	5.94	3.93	5.38	2.81	4.84	3.41	5.26	5.06	4.27	2.42	2.66	2.92	2.54	5.24	5.51
Eu	0.46	0.47	0.49	0.61	0.41	0.45	0.42	0.45	0.29	0.39	0.40	0.36	0.62	0.76	0.75	0.68	1.06	1.11
Gd	3.38	2.38	3.31	3.97	3.52	4.62	2.13	3.64	2.54	3.51	3.27	3.15	1.95	2.13	2.36	2.14	4.66	4.82
Tb	0.57	0.37	0.54	0.65	0.63	0.82	0.38	0.62	0.41	0.53	0.50	0.51	0.33	0.35	0.39	0.36	0.76	0.79
Dy	3.16	1.99	2.91	3.19	3.77	4.79	2.17	3.00	2.19	2.78	2.61	2.77	1.88	2.04	2.23	1.99	4.32	4.52
Ho	0.71	0.41	0.59	0.63	0.83	1.02	0.50	0.57	0.40	0.55	0.52	0.54	0.39	0.43	0.46	0.41	0.92	0.93
Er	2.17	1.26	1.80	1.86	2.70	3.07	1.63	1.67	1.09	1.68	1.56	1.57	1.14	1.22	1.35	1.20	2.59	2.63
Tm	0.36	0.23	0.30	0.33	0.48	0.50	0.29	0.27	0.17	0.29	0.25	0.24	0.19	0.19	0.21	0.18	0.42	0.41
Yb	2.59	1.72	2.12	2.40	3.56	3.42	2.14	1.86	1.12	2.08	1.88	1.65	1.30	1.26	1.38	1.26	2.68	2.77
Lu	0.47	0.31	0.38	0.42	0.66	0.56	0.40	0.31	0.20	0.37	0.34	0.28	0.24	0.21	0.23	0.21	0.47	0.48
Y	22.60	15.20	21.20	24.40	31.90	33.40	15.80	19.00	13.20	19.30	17.70	19.50	13.30	13.30	15.00	13.70	29.20	29.70
Rb	342.00	345.00	298.00	349.00	326.00	300.00	297.00	305.00	318.00	329.00	312.00	336.00	113.00	96.00	73.10	113.50	130.00	158.00

(Continued)

Table 3. (*Continued*)

Age (Ma)	148.1	148.1	148.1	148.1	148.1	148.1	149.8	149.8	149.8	149.8	149.8	149.8	258.5	258.5	254.7	254.7	253.9	253.9
Sample	WL-5	WL-19	WL-23	WL-25	WL-26-1	WL-27	WL-6	WL-7-2	WL-8-2	WL-17	WL-18	WL-26-2	WL-29	WL-30	WL-32-2	WL-32-3	WL-33-2	WL-34-2
Lithology	Monzogranite						Granite porphyry						Granodiorite				MMEs	
Sr	74.30	89.60	84.70	78.50	76.90	73.80	94.70	110.50	96.50	99.60	96.90	105.50	271.00	327.00	343.00	317.00	320.00	298.00
Ba	280.00	342.00	315.00	320.00	269.00	250.00	337.00	341.00	308.00	335.00	303.00	308.00	815.00	803.00	720.00	1145.00	676.00	858.00
U	6.16	3.92	5.27	2.99	10.40	34.60	7.29	3.36	3.56	3.49	3.39	17.95	1.10	0.85	0.68	0.58	1.23	1.93
Th	37.20	35.20	36.40	38.70	36.80	40.10	36.80	41.50	31.50	41.20	34.40	39.30	12.80	9.93	9.59	6.99	7.70	6.55
Nb	33.20	25.10	24.90	27.20	28.80	24.40	24.90	20.50	17.60	28.30	25.20	20.00	6.20	5.70	5.90	5.80	9.90	12.80
Ta	3.81	2.08	2.94	2.83	3.10	2.35	2.01	2.60	2.59	2.80	2.54	3.26	0.59	0.44	0.45	0.42	0.66	0.78
Zr	153.00	123.00	158.00	125.00	141.00	146.00	155.00	114.00	107.00	137.00	126.00	111.00	115.00	133.00	139.00	106.00	125.00	139.00
Hf	5.40	4.10	5.10	4.20	4.80	4.60	5.00	3.90	3.50	4.80	4.70	3.80	3.10	3.30	3.40	2.60	3.20	3.40
Li	20.70	25.60	25.80	22.20	53.00	39.90	24.90	27.20	34.10	38.20	51.90	29.30	23.10	27.90	29.40	44.00	48.10	60.10
V	9.00	7.00	10.00	11.00	7.00	9.00	8.00	14.00	8.00	8.00	7.00	6.00	64.00	90.00	108.00	98.00	223.00	257.00
Cr	20.00	20.00	30.00	20.00	30.00	30.00	20.00	10.00	10.00	20.00	10.00	20.00	20.00	30.00	30.00	30.00	10.00	20.00
Co	1.60	0.80	1.10	1.00	0.70	0.70	1.40	1.00	1.30	1.00	1.00	0.80	6.40	8.70	9.90	8.90	19.80	24.20
Ni	2.10	1.00	1.20	4.20	1.40	1.10	1.90	1.60	1.90	1.80	1.60	0.70	3.90	5.00	5.80	6.50	7.00	8.10
Ga	21.60	20.80	20.70	21.80	20.50	20.50	20.10	20.20	18.70	21.00	20.60	20.30	15.20	15.30	16.10	15.20	19.30	20.40
Cs	11.40	11.15	9.61	8.86	11.85	8.84	11.00	26.60	18.95	18.00	15.00	21.70	4.67	5.24	3.71	12.30	9.89	11.45
Ag	0.24	0.09	0.03	0.06	0.03	0.09	0.11	0.03	0.07	0.08	0.03	0.03	0.07	0.49	0.04	0.04	0.03	0.01
Cu	5.00	0.40	0.90	5.50	1.50	0.60	1.10	1.20	1.40	1.70	0.90	0.60	14.00	100.50	15.70	28.90	45.10	52.40
Fe	1.02	0.97	0.93	0.86	0.89	0.93	0.75	0.88	0.81	0.82	0.85	0.77	2.12	2.74	3.03	2.62	5.35	6.00
Mn	309.00	259.00	290.00	165.00	293.00	350.00	222.00	248.00	226.00	326.00	248.00	292.00	469.00	643.00	649.00	551.00	1320.00	1420.00
Mo	2.95	1.72	2.38	2.28	4.07	2.84	1.60	1.10	1.15	2.06	1.09	1.89	0.91	1.45	1.01	0.96	0.52	0.53
Pb	24.90	28.80	20.20	50.10	19.30	22.10	24.50	35.00	46.30	34.80	39.40	39.50	11.80	12.10	12.10	14.80	12.40	13.10
W	7.00	6.00	12.00	7.00	8.00	10.00	11.00	13.00	14.00	11.00	22.00	32.00	1.00	1.00	0.50	1.00	1.00	1.00
Zn	21.00	196.00	14.00	178.00	15.00	75.00	24.00	51.00	304.00	27.00	36.00	465.00	32.00	57.00	48.00	47.00	89.00	104.00
ΣREE	174.74	155.97	170.51	200.24	147.46	193.56	126.66	146.33	108.03	163.31	156.83	120.49	97.03	101.79	112.45	86.95	122.54	135.06
LREE/HREE	12.03	16.99	13.27	13.89	8.13	9.30	12.14	11.26	12.30	12.85	13.35	10.25	12.08	12.00	12.06	10.22	6.29	6.78
$(La/Yb)_N$	10.88	16.56	13.77	14.08	6.79	9.38	9.65	12.11	14.99	11.90	13.20	11.39	12.86	13.32	14.03	11.67	5.59	6.19
δEu	0.35	0.48	0.38	0.38	0.34	0.28	0.52	0.33	0.30	0.28	0.30	0.30	0.87	0.98	0.87	0.89	0.66	0.66
Sr/Y	3.29	5.89	4.00	3.22	2.41	2.21	5.99	5.82	7.31	5.16	5.47	5.41	20.38	24.59	22.87	23.14	10.96	10.03
Th/Yb	14.36	20.47	17.17	16.13	10.34	11.73	17.20	22.31	28.13	19.81	18.30	23.82	9.85	7.88	6.95	5.55	2.87	2.36
Ta/Yb	1.47	1.21	1.39	1.18	0.87	0.69	0.94	1.40	2.31	1.35	1.35	1.98	0.45	0.35	0.33	0.33	0.25	0.28
Nb/Yb	12.82	14.59	11.75	11.33	8.09	7.13	11.64	11.02	15.71	13.61	13.40	12.12	4.77	4.52	4.28	4.60	3.69	4.62
Lu/Yb	0.18	0.18	0.18	0.18	0.19	0.16	0.19	0.17	0.18	0.18	0.18	0.17	0.18	0.17	0.17	0.17	0.18	0.17
Rb/Sr	4.60	3.85	3.52	4.45	4.24	4.07	3.14	2.76	3.30	3.30	3.22	3.18	0.42	0.29	0.21	0.36	0.41	0.53
La/Sm	8.45	10.73	8.75	7.93	8.58	8.31	10.25	6.49	6.86	6.56	6.84	6.14	9.63	8.80	9.25	8.07	3.99	4.34
Zr/Hf	28.33	30.00	30.98	29.76	29.38	31.74	31.00	29.23	30.57	28.54	26.81	29.21	37.10	40.30	40.88	40.77	39.06	40.88

(*Continued*)

Table 3. *(Continued)*

Age (Ma)	148.1	148.1	148.1	148.1	148.1	148.1	149.8	149.8	149.8	149.8	149.8	149.8	258.5	258.5	254.7	254.7	253.9	253.9
Sample	WL-5	WL-19	WL-23	WL-25	WL-26-1	WL-27	WL-6	WL-7-2	WL-8-2	WL-17	WL-18	WL-26-2	WL-29	WL-30	WL-32-2	WL-32-3	WL-33-2	WL-34-2
Lithology	Monzogranite						Granite porphyry						Granodiorite				MMEs	
Ti/Zr	5.09	6.82	4.55	7.19	3.83	3.70	3.48	4.73	6.72	6.13	4.76	7.02	15.12	16.23	16.39	19.23	36.93	41.84
Ti/Y	34.48	55.22	33.93	36.85	16.91	16.15	34.15	28.40	54.50	43.49	33.87	39.97	130.72	162.27	151.87	148.78	158.09	195.80
Nb/Ta	8.71	12.07	8.47	9.61	9.29	10.38	12.39	7.88	6.80	10.11	9.92	6.13	10.51	12.95	13.11	13.81	15.00	16.41
Zr/Nb	4.61	4.90	6.35	4.60	4.90	5.98	6.22	5.56	6.08	4.84	5.00	5.55	18.55	23.33	23.56	18.28	12.63	10.86
Dy/Yb	1.22	1.16	1.37	1.33	1.06	1.40	1.01	1.61	1.96	1.34	1.39	1.68	1.45	1.62	1.62	1.58	1.61	1.63
La/Yb	15.17	23.08	19.20	19.63	9.47	13.07	13.46	16.88	20.89	16.59	18.40	15.88	17.92	18.57	19.57	16.27	7.80	8.63
K/Cs	3677.33	4087.37	4500.50	5050.11	3411.59	4469.93	3728.04	1588.48	2229.74	2301.30	2756.03	1901.27	5510.50	4182.33	5370.11	2125.94	1645.15	1798.01
U/Th	0.17	0.11	0.14	0.08	0.28	0.86	0.20	0.08	0.11	0.08	0.10	0.46	0.09	0.09	0.07	0.08	0.16	0.29
K/Rb	122.58	132.10	145.13	128.21	124.01	131.71	138.08	138.54	132.87	125.91	132.50	122.79	227.73	228.29	272.55	230.39	125.16	130.30
Y/Ho	31.83	37.07	35.93	38.73	38.43	32.75	31.60	33.33	33.00	35.09	34.04	36.11	34.10	30.93	32.61	33.41	31.74	31.94
R1	2511.60	2295.07	2462.90	2284.86	2566.43	2586.40	2556.50	2566.67	2570.76	2484.45	2568.03	2498.83	2710.11	2652.49	2549.58	2596.74	1760.39	1411.78
R2	348.15	357.21	340.52	367.10	308.42	321.29	328.83	330.79	344.22	354.57	337.48	346.48	631.63	709.83	809.66	649.37	1062.55	1057.18
T_{Zr} (°C)	818	812	819	813	820	821	817	818	821	819	822	822	785	782	781	776	–	–

Note: Mg no. $= 100 \times$ Mg/(Mg + Fe^{2+}); A/CNK $=$ Al/(Ca + Na + K) in molar; A/NK $=$ Al/(Na + K) in molar; δEu $=$ Eu$_N$/(Sm$_N \times$ Gd$_N$)$^{1/2}$

host melts that may have been caused by the rapid cooling of the mafic melt (Sarjoughian *et al.* 2012). Plagioclase with a sieve texture was also observed in the MMEs (Fig. 4e), which is thought to be the result of the partial melting of feldspar after it entered the mafic magma at a higher temperature (Castro *et al.* 1999). Hence, we suggest that the petrogenesis of the MMEs involved a magma mixing process.

Although magma mixing (as well as fractionation) processes compositionally modified the injected mafic melts, their geochemistry and zircon Hf isotope compositions can still provide constraints on their origin. The MMEs have lower SiO$_2$ (55.53–58.03 wt %), but higher MgO (3.27–3.66 wt %) and Fe$_2$O$_3^T$ (8.21–9.16 wt %) contents, as well as Mg no. values (44.10–44.18), than common crust-derived melts (Rapp & Watson, 1995; Patiño Douce, 1999), demonstrating that the parental mafic melts were unequivocally derived from an ultra-mafic mantle. The MMEs are characterized by enrichment in LREEs and LILEs (Rb, Th, K and Pb), but depletion in HREEs and HFSEs (Nb, Ta, P and Ti) (Fig. 9a, b). The MMEs have high Y (29.20–29.70 ppm) and Yb$_N$ (15.76–16.29) concentrations, whereas they have low Sr/Y (10.03–10.96) and (La/Yb)$_N$ (5.59–6.19) ratios (Fig. 8e, f). Additionally, these MMEs have uniform zircon Hf isotopic compositions, with positive $\epsilon_{Hf}(t)$ values from +0.1 to +3.5 (Fig. 7). These characteristics are similar to those of normal arc magmas (Defant & Drummond, 1990; McDonough & Sun, 1995), indicating an isotopically enriched lithospheric mantle source modified by fluid/melt-related metasomatism associated with subduction. Furthermore, the metasomatism was likely dominated by slab-derived fluids rather than sediments and associated melts, as indicated by the high Ba/Th (87.79–130.99) and Ba/La (32.34–35.90), and low Th/Nb (0.51–0.78) and Th/Yb (2.36–2.87) ratios (Ribeiro *et al.* 2013). In summary, we suggest that the Narenwula MMEs likely formed as the products of mixed mafic and felsic magmas. The mafic magmas may have been derived from the partial melting of an enriched lithospheric mantle metasomatized by slab-derived fluids.

5.b.2. Host granodiorites

We propose that the host granodiorites are I-type granitoids (Chappell & White, 1992) based on the following observations: (1) they contain minerals typical of I-type granitoids (e.g. hornblende and biotite) (Fig. 4b, c); (2) they are metaluminous to weakly peraluminous with A/CNK ratios of 0.99–1.12 (Fig. 8c) and have high CaO contents (2.65–3.98 wt %) (Chappell, 1999; Frost *et al.* 2001); (3) their low Rb/Sr (0.21–0.42) and Rb/Ba (0.10–0.14), but high K/Rb ratios (227.73–230.39) are similar to those of I-type granites and inconsistent with those of S-type granites (Whalen *et al.* 1987); (4) 10 000 Ga/Al ratios (1.92–2.01; Fig. 10) are less than 2.6, and the Zr + Nb + Ce + Y contents of the samples (163.90–212.40) are less than 350 ppm (Whalen *et al.* 1987); and (5) the T$_{Zr}$ of the samples is estimated at 776–785 °C, much lower than that of A-type granitoids in this study (Watson & Harrison, 1983). According to the above evidence, we propose that the host granodiorites of the Narenwula complex are I-type granitoids.

The granodiorite samples are enriched in LREEs and LILEs (Rb, Th, K and Pb) but depleted in HREEs and HFSEs (Nb, Ta, P and Ti) (Fig. 9a, b). They have high Y (13.30–15.00 ppm) and Yb$_N$ (7.41–8.12) concentrations, but low Sr/Y (20.38–24.59) and (La/Yb)$_N$ (11.67–14.03) ratios (Fig. 8e, f). These geochemical characteristics are identical to those of normal arc magmas

Fig. 8. (Colour online) (a) TAS (total alkali silica) diagram (after Middlemost, 1994). (b) K_2O versus SiO_2 diagram (after Peccerillo & Taylor, 1976). (c) A/NK versus A/CNK diagram (after Maniar & Piccoli, 1989). (d) Rb–Ba–Sr diagram (after El Bouseily & El Sokkary, 1975). (e) Sr/Y versus Y diagram (after Defant & Drummond, 1990). (f) $(La/Yb)_N$ versus Yb_N diagram (after Defant & Drummond, 1990). Abbreviations: HFGs – highly fractionated granites; NGs – normal granites.
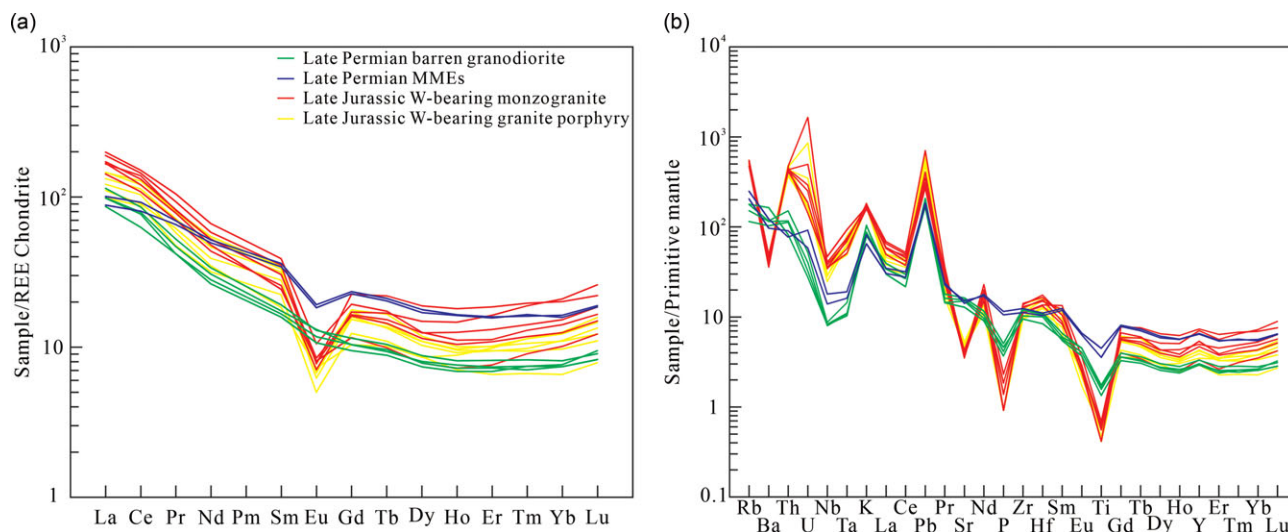
Fig. 9. (Colour online) (a) Chondrite-normalized REE patterns and (b) primitive-mantle-normalized trace-element spider diagrams for the granitic intrusions and MMEs from the Narenwula complex (normalization values are from Sun & McDonough, 1989).

(Defant & Drummond, 1990). The granodiorite samples have higher MgO (1.06–1.60 wt %) and $Fe_2O_3^T$ (3.08–4.41 wt %) contents, as well as Mg no. values (40.54–41.82), compared to common crustal-derived melts (Rapp & Watson, 1995; Patiño Douce, 1999). Moreover, geochemical evidence suggests the mixing of mantle- and crustal-derived components. The Nb/Ta, Zr/Hf and Rb/Sr ratios of these granodiorite samples vary from 10.51 to 13.81, 37.10 to 40.88, and 0.21 to 0.42, respectively, which are between those of the crust (Nb/Ta = 11.4, Zr/Hf = 33.0 and Rb/Sr > 0.5) and mantle (Nb/Ta = 17.8, Zr/Hf = 37 and Rb/Sr = 0.03–0.047) (McDonough & Sun, 1995; Taylor & McLennan, 1995; Rudnick & Gao, 2003). The geochemical data for the host granodiorites and MMEs also support a magma mixing origin (Fig. 11). The samples define hyperbolic mixing arrays in the MgO/Al_2O_3 versus SiO_2/CaO diagram (Fig. 11a). The $Fe_2O_3^T/SiO_2$ versus CaO/SiO_2 diagram (Fig. 11b) also exhibits an array suggesting that the mixing of distinct magma occurred during the evolution of the samples. In the $Fe_2O_3^T$ versus MgO diagram (Fig. 11c), the samples do not plot along the fractional crystallization trend but near the mixing line between mantle and crustal magmas. These trends are consistent with two-component mixing and are in accordance with field and petrographic evidence (e.g. the chilled margin and plagioclase with sieve texture). The granodiorite samples have positive and homogeneous zircon $\epsilon_{Hf}(t)$ values (+0.4 to +3.6) with two-stage model ages of 1067–1256 Ma, indicating its derivation from Mesoproterozoic juvenile lower crust. However, large volumes of the *c.* 1.3–1.0 Ga crust have not been reported beneath the Narenwula area or the northern NCC. The identification of spinel lherzolite in the lithospheric mantle beneath the northern NCC, distinct from the cratonic lithospheric mantle, indicates that the ancient cratonic lithospheric mantle was partially modified before or at 1.3 Ga and transferred as a part of a relatively young, fertile, thin and hot lithospheric mantle (Klemme & O'Neill, 2000). Thus, the granodiorites were mostly generated by the partial melting of the Mesoproterozoic juvenile lower crust with varying contributions from mantle-derived magmas. Notably, the zircon grains from the MMEs have a similar morphology and $\epsilon_{Hf}(t)$ values (+0.1 to +3.5) to those of zircon grains from the host granodiorites ($\epsilon_{Hf}(t)$ from +0.4 to +3.6), indicating the isotopic equilibrium

between them due to the magma mixing processes (Vernon, 1984; Vernon *et al.* 1988; Elburg, 1996; Barbarin, 2005) (Figs 5, 7). On a Rb–Ba–Sr diagram (El Bouseily & El Sokkary, 1975), most granodiorite samples plot in the normal granite field (Fig. 8d), indicating that limited fractional crystallization occurred during the formation of the granodiorites. Moreover, in the primitive mantle-normalized trace-element diagrams (Fig. 9b), the negative Nb, Ta, P and Ti values may reflect the separation of Ti-bearing minerals and apatite. In summary, the host granodiorites and MMEs formed by the mixing of felsic (derived from the partial melting of the juvenile lower crust) and mafic melts (derived from the partial melting of the mantle that had been metasomatized by slab-derived fluids), while these hybrid magmas subsequently underwent limited fractional crystallization.

5.c. Petrogenesis of the W-bearing monzogranite and granite porphyry

We propose that the W-bearing monzogranite and granite porphyry are A-type granitoids based on the following observations: (1) the lower P_2O_5 concentration (0.02–0.05 wt %) and absence of phosphate minerals (King *et al.* 1997; Bonin, 2007); (2) the high $K_2O + Na_2O$ contents (8.40–9.14 wt %), Ga concentrations (18.70–21.80 ppm) (Fig. 10a; Table 3), ΣREE and Ga/Al ratios (2.61–3.01), and low Eu, Ba, Sr, P and Ti contents (Fig. 9a, b); (3) the plotting of most samples in the A-type granite field (Fig. 10b–f) on the discrimination diagrams (Whalen *et al.* 1987); (4) their moderate Al_2O_3 contents, while their A/CNK values mainly range from 1.03 to 1.11, showing a weakly peraluminous nature (Fig. 8c); and (5) the T_{Zr} of the samples is 812–822 °C, much higher than that of I-type granitoids (T_{Zr} = 764–781 °C) but similar to that of A-type granitoids (T_{Zr} = 839 °C) (Watson & Harrison, 1983).

Although A-type granites are commonly associated with extensional tectonic settings, their origin remains controversial. Several models have been proposed to decipher the origin of A-type granites: (a) direct fractionation of mantle-derived alkaline basalts (Turner *et al.* 1992, 1996; Mushkin *et al.* 2003), (b) mixing between crust-derived granitic magmas and mantle-derived mafic magmas (Bedard, 1990; Kerr & Fryer, 1993; Mingram *et al.* 2000), and
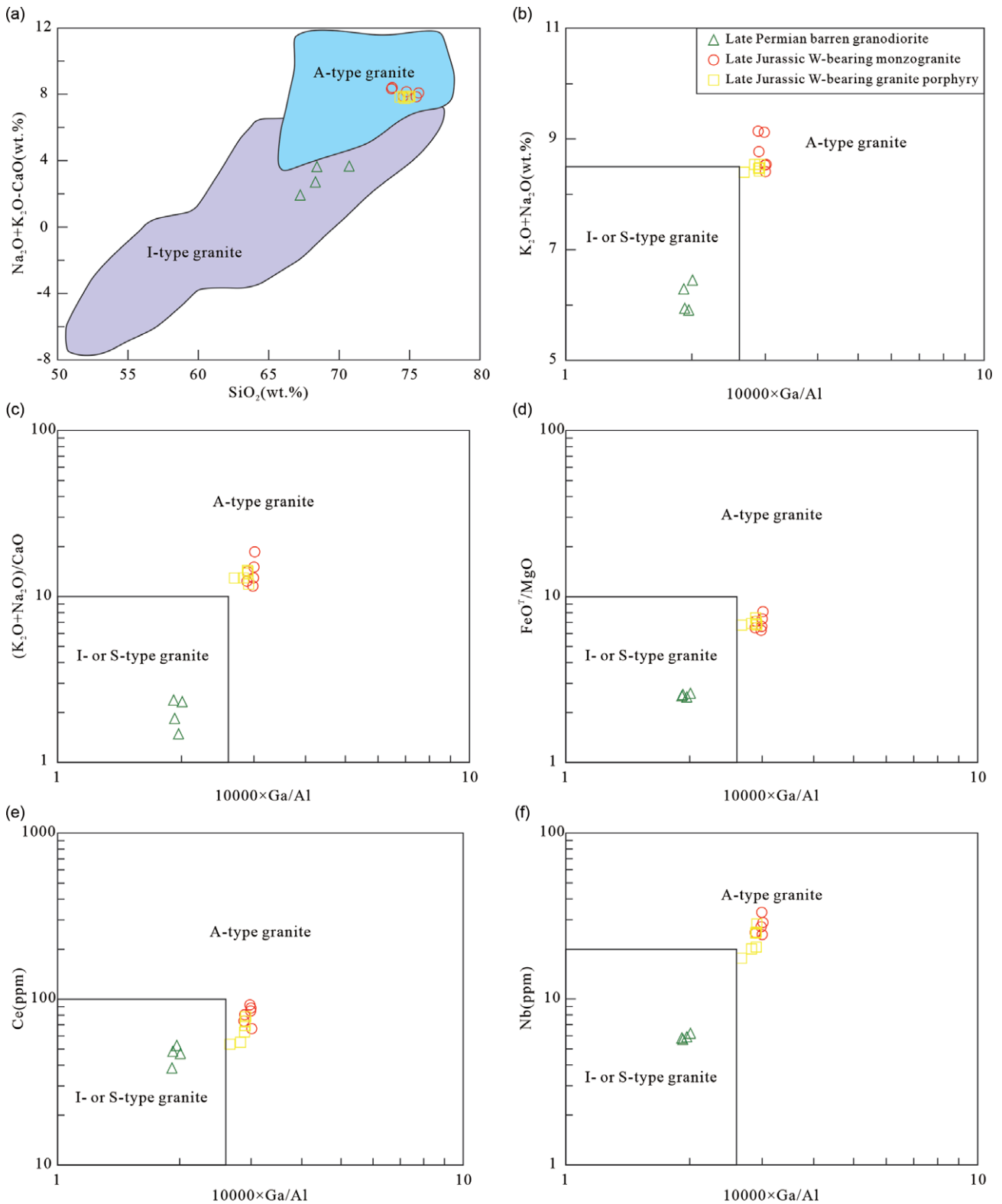
Fig. 10. (Colour online) (a) (Na$_2$O + K$_2$O–CaO) versus SiO$_2$ diagram (after Frost *et al.* 2001). (b) K$_2$O + Na$_2$O, (c) (K$_2$O + Na$_2$O)/CaO, (d) FeO^T/MgO, (e) Ce and (f) Nb versus 10 000 × Ga/Al discrimination diagrams of Whalen *et al.* (1987).

(c) partial melting of crust-sourced rocks (Collins *et al.* 1982; Clemens *et al.* 1986; Skjerlie & Johnston, 1993; King *et al.* 1997).

Experimental studies indicate that mantle melting cannot directly produce silica-rich magmas; that is, only small quantities

of silica-rich rocks can be generated by the differentiation of mafic mantle-derived magmas (Hirose, 1997). Current researchers have come to a consensus that if a granitic magma is generated by direct fractional crystallization of a mantle-derived magma, it should be
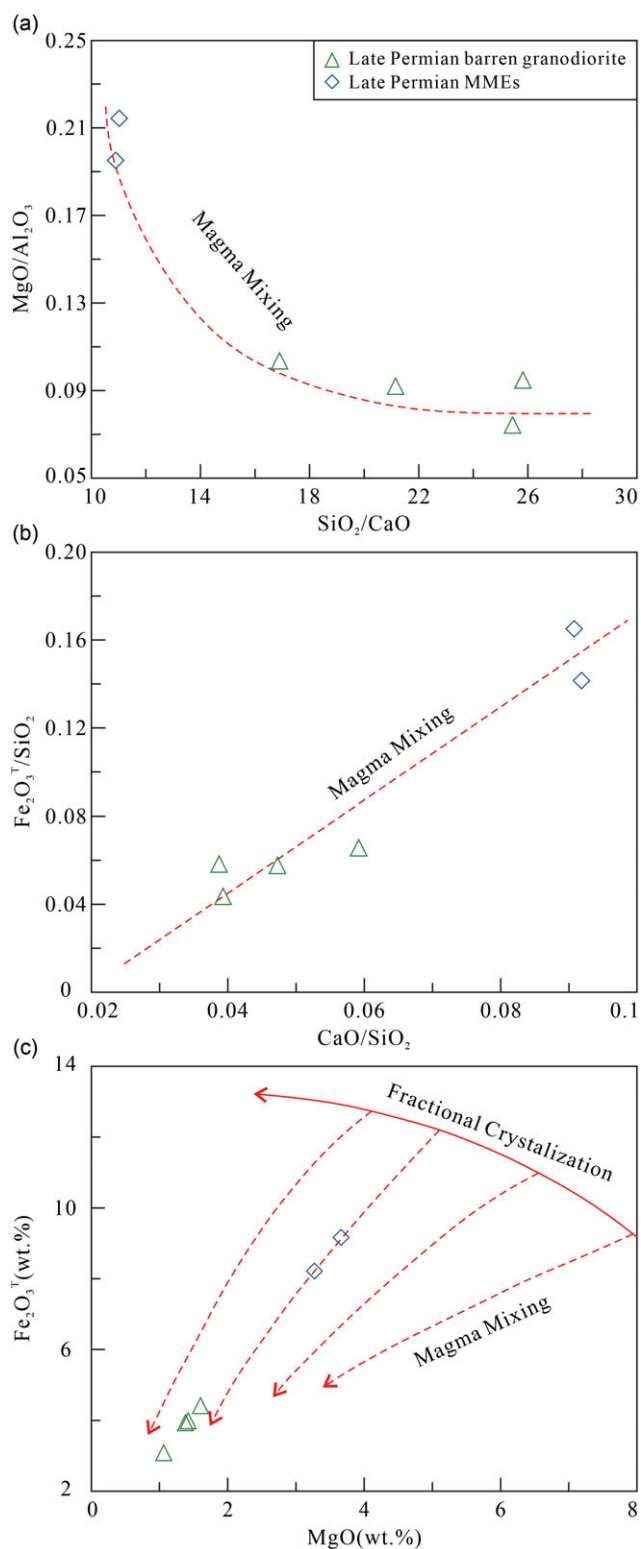
Fig. 11. (Colour online) Element correlation diagrams of mafic microgranular enclaves and host granodiorites from the Narenwula complex (after Zorpi *et al.* 1989; Berzina *et al.* 2014; Yang *et al.* 2015).

possible to observe a complete evolutionary sequence from mafic to felsic rocks (e.g. Turner *et al.* 1992; Mushkin *et al.* 2003; Litvinovsky *et al.* 2015). However, intermediate–felsic and felsic rocks are more widespread than mafic rocks in the Narenwula

region (Fig. 2). Therefore, we can exclude the scenario where W-bearing granitoids originated from the direct fractionation of mantle-derived alkaline basalts. Furthermore, the absence of MMEs and mafic compositions precludes the magma mixing scenario between crust- and mantle-derived magmas, which indicates a crustal source genesis for A-type granites.

The W-bearing granitoids are enriched in LREEs and LILEs (Rb, Th, U, K and Pb), depleted in HREEs, Ba, Sr and HFSEs (Nb, Ta, P and Ti), and show significantly negative Eu anomalies (0.28–0.52). All these characteristics are likely derived from the continental crust (Harris *et al.* 1986; Sun & McDonough, 1989). They have high Y (13.20–33.40 ppm) and Yb_N (6.59–20.94) concentrations, but low Sr/Y (2.21–7.31) and $(La/Yb)_N$ (6.79–16.56) ratios, consistent with arc rocks (Fig. 8e, f). They contain a SiO_2 content of 73.73–75.65 wt %, with lower Mg no. values (18.04–22.17) than those of mantle-generated magma (Mg no. > 70) (Rudnick & Gao, 2003); however, these values are consistent with those of crust-derived melts (Mg no. < 40) (Rapp & Watson, 1995). Additionally, the Ti/Zr and Ti/Y ratios are 3.48–7.19 and 16.15–55.22, respectively, consistent with those of crust-derived rocks (Ti/Zr < 20 and Ti/Y < 200) (Wedepohl, 1995). The Th/Ce, Th/La, Lu/Yb and Rb/Sr ratios are 0.42–0.72, 0.82–1.50, 0.16–0.19 and 2.76–4.60, respectively, which are significantly higher than the values of primitive mantle (Th/Ce = 0.02–0.05, Th/La = 0.12, Lu/Yb = 0.14–0.15 and Rb/Sr = 0.03–0.047) (Sun & McDonough, 1989), but similar to those of crustal rocks (Th/Ce > 0.15, Th/La > 0.30, Lu/Yb = 0.16–0.18 and Rb/Sr > 0.5) (Sun & McDonough, 1989; Rudnick & Gao, 2003; Plank, 2005). Moreover, the Nb/Ta, Zr/Hf and Ta/U ratios are 6.13–12.39, 26.81–31.74 and 0.07–0.95, respectively, which are closer to the values of the crust (Nb/Ta = 11.4, Zr/Hf = 33.0 and Ta/U = ~1.1) (Sun & McDonough, 1989; Taylor & McLennan, 1995) than those of primitive mantle (Nb/Ta = 17.8, Zr/Hf = 37.0 and Ta/U = ~2.7) (McDonough & Sun, 1995), indicating a crustal component in the magma source. The negative $\epsilon_{Hf}(t)$ values (–6.0 to –2.1), with old two-stage model ages (1338–1583 Ma), indicate that the partial melting of the ancient lower crust predominantly generated these rocks, supported by the findings of Zhao *et al.* (2005) and Zhang *et al.* (2012). Zhao *et al.* (2005) argued that the Archaean continental crust in the northern NCC was rejuvenated by the underplating of mafic magmas at *c.* 1.8–1.6 Ga. The highly depleted zircon $\epsilon_{Hf}(t)$ values of the *c.* 1.3 Ga diabase in northern NCC indicate that depleted lithospheric mantle sources were involved (Zhang *et al.* 2012). Yang *et al.* (2017) recognized that the O–Hf isotopic variations of zircons from late Mesozoic alkaline A-type granites in NE China can be explained by the melting of a hybrid source consisting of different proportions of altered oceanic crust and enriched mantle components. Thus, Yang *et al.* (2017) concluded that the recycling of subducted oceanic crust represents a novel exotic source for the origin of alkaline A-type granites in intraplate extensional settings. More evidence is needed to affirm the incorporation of subducted oceanic crust in the source of the late Mesozoic A-type granitoids; for example, obtaining the oxygen isotopic ratio would be beneficial (Yang *et al.* 2017). However, certain geochemical characteristics of the Late Jurassic A-type granitoids in the present study are inconsistent with those of alkaline A-type granitoids reported by Yang *et al.* (2017), including (1) the Ti and Ni contents of the Jurassic A-type granitoids are lower (0.09–0.15 wt % and 0.70–4.2 ppm, respectively) than those reported by Yang *et al.* (2017) (0.13–0.7 wt % and 3.4–8.9 ppm, respectively); (2) the Nb/Ta ratios of these A-type granitoids are

6.1–12.4, while those reported by Yang *et al.* (2017) range from 9.8 to 16.4 (mostly > 13), which demonstrates the continental source nature of our samples compared to the mantle affinity of the samples described by Yang *et al.* (2017); and (3) the negative $\epsilon_{Hf}(t)$ values. The combination of these features led us to conclude that a significant contribution of a hybrid source (altered oceanic crust and enriched mantle-derived mafic rocks) in the granite genesis can be excluded.

Advanced fractional crystallization occurred during the formation of the Late Jurassic W-bearing granitic intrusions, where the monzogranite and granite porphyry samples plot in the highly fractionated granite field based on their Rb, Sr, and Ba concentrations (Fig. 8d). In the chondrite-normalized REE patterns, significantly negative Eu anomalies (Eu/Eu* = 0.28–0.52) reflect the fractional crystallization of plagioclase and/or K-feldspar (Fig. 9a). In the primitive mantle-normalized trace-element diagrams (Fig. 9b), pronounced depletions in Ba, Sr, P and Ti may reflect the separation of plagioclase, K-feldspar, Ti-bearing minerals and apatite. This evidence indicates that the parent magmas of W-bearing granitoids underwent extensive fractional crystallization. In summary, we propose that the W-bearing granitoids from the Narenwula complex are highly fractionated A-type granitoids, which were derived from the partial melting of ancient lower crust and subsequently underwent a high degree of fractional crystallization.

5.d. Genetic link between the Narenwula complex and W mineralization

Generally, W mineralization is associated with highly fractionated granites, as demonstrated by numerous cases worldwide (Singh & Singh, 2001; Fogliata *et al.* 2012; Mao *et al.* 2013; Huang & Jiang, 2014; Zhang, Y. *et al.* 2017; Cao *et al.* 2018, 2020; Jiang *et al.* 2018; Yuan *et al.* 2018; Steiner, 2019; Li, J. *et al.* 2021; Xie *et al.* 2021). It has been proposed that ore-forming elements may be concentrated during multiple stages of magmatic activity and then extracted by magmatic fluids (Che *et al.* 2013; Harlaux *et al.* 2018) or leached from granitoids and/or metamorphic rocks and transported by external (metamorphic or meteoric) fluids (Linnen & Williams-Jones, 1995; Vindel *et al.* 1995; Vallance *et al.* 2001). Xie *et al.* (2021) systematically collected the published geochemical data of W-barren and W-mineralized granitoids in NE China, and concluded that the late Mesozoic W-mineralized granitoids have higher Rb/Sr and U/Th, but lower (La/Yb)$_N$, LREE/HREE, Eu/Eu*, K/Rb, Zr/Hf, Nb/Ta and Y/Ho ratios than contemporary W-barren granitoids. The K/Rb, Zr/Hf and Nb/Ta ratios are considered to be 'geochemical twin' elemental ratios because they have the same charge and ionic radius. They have similar geochemical properties and are not expected to fractionate during most geological processes (Green, 1995). Previous studies have suggested that these 'geochemical twin' elemental ratios in granites decrease because of fractional crystallization (Bau, 1996; Linnen & Keppler, 1997, 2002; Dostal & Chatterjee, 2000; Claiborne *et al.* 2006; Deering & Bachmann, 2010; Dostal *et al.* 2015; Ballouard *et al.* 2016). In present study, the W-bearing granitoids had higher Rb/Sr, and lower Nb/Ta, Zr/Hf and K/Rb ratios than the W-barren granodiorites (Fig. 12a–d). Moreover, the W-bearing granitoids all plot in the field of W-mineralized granitoids proposed by Xie *et al.* (2021) (Fig. 12a–d). In contrast, the W-barren granodiorites from the Narenwula complex plot in the field of W-barren granitoids (Fig. 12a–d). In addition, the W-bearing granitoids have higher W concentrations than the

W-barren granodiorites and the average continental crust (Fig. 12e, f). Combined with the published geochemical data for late Mesozoic W-mineralized granitoids, we noted that the W concentrations of W-mineralized granitoids increased with an increasing Rb/Sr ratio (Fig. 12e) and decreased with an increasing K/Rb ratio (Fig. 12f), suggesting that fractional crystallization of the W-mineralized granitic magma was beneficial for the concentration of W. Using Rb/Sr as a parameter for the extent of fractionation, Lehmann (1987) and Lehmann *et al.* (1990) demonstrated that extreme fractional crystallization may result in both very high Rb/Sr ratios and enhanced W concentrations, necessary for W mineralization. Additionally, many studies have confirmed that the enrichment in W and related incompatible elements during magmatic fractionation is an essential requirement for W mineralization (Webster *et al.* 2004; Breiter *et al.* 2005; Thomas *et al.* 2005; Zhang, Y. *et al.* 2017; Cao *et al.* 2018; Yuan *et al.* 2018; Li, J. *et al.* 2021). Relatively low ratios of 'geochemical twin' elements suggest that the W-bearing granitoids are more fractionated than the W-barren granodiorites, and that the extreme fractional crystallization process is favourable for W enrichment.

Based on the geological, geochronological and geochemical features of the Narenwula complex in NE China, an integrated model of granitic magmatism and W mineralization in the Narenwula ore district can be proposed as follows. First, during late Permian time, mantle-derived mafic magmas successively underplated beneath the juvenile lower crust and induced extensive crustal melting, which produced a deep hot zone and generated felsic magmas. The mantle-derived mafic magmas halted as a result of obstruction by the deep hot zone and rarely passed through the zone (Annen *et al.* 2006), which may explain why contemporaneous mafic rocks are rarely exposed in this area. However, when small amounts of mantle-derived mafic magmas passed through the zone and mixed with felsic magmas in deeper magma chambers, hybrid magmas were generated. The hybrid magmas subsequently underwent limited fractional crystallization and formed the MMEs and host granodiorite. Second, during Late Jurassic time, the parental magmas for the W-bearing granitoids were mainly derived from the partial melting of ancient lower crustal rocks. W is a lithophile element, so it is generally enriched in the crust, but depleted in the mantle (Rudnick & Gao, 2003; Arevalo & McDonough, 2008). Therefore, the ancient lower crust beneath the Narenwula area may show significant potential for W mineralization. Continual fractional crystallization appears to have been the dominant process that further enriched W in the granitic magmas. Previous studies have demonstrated the importance of magmatic differentiation in the formation of W deposits, where ore metals (W) and volatiles (F and Li) become enriched in highly evolved magma, followed by their accumulation in the residual liquid (Thomas *et al.* 2005; Romer *et al.* 2014; Li, J. *et al.* 2021). Therefore, the highly fractionated A-type granitoids in the Narenwula area contributed to the W enrichment. Third, in the late stages of magma evolution, the volatile-rich fluids exsolved and segregated from the melt. Their subsequent liquid–vapour phase separation could have changed the physical and chemical conditions of the magmatic–hydrothermal system (Li, J. *et al.* 2021). The post-magmatic fluids became enriched in F and Cl, significantly enhancing the solubility of W (Webster & Holloway, 1988; Keppler & Wyllie, 1991; Schaller *et al.* 1992; Signorelli & Carroll, 2000; Zajacz *et al.* 2008; Yuan *et al.* 2019). Previous studies have shown that W can be strongly partitioned from the melt to the fluid (Gibert *et al.* 1992;
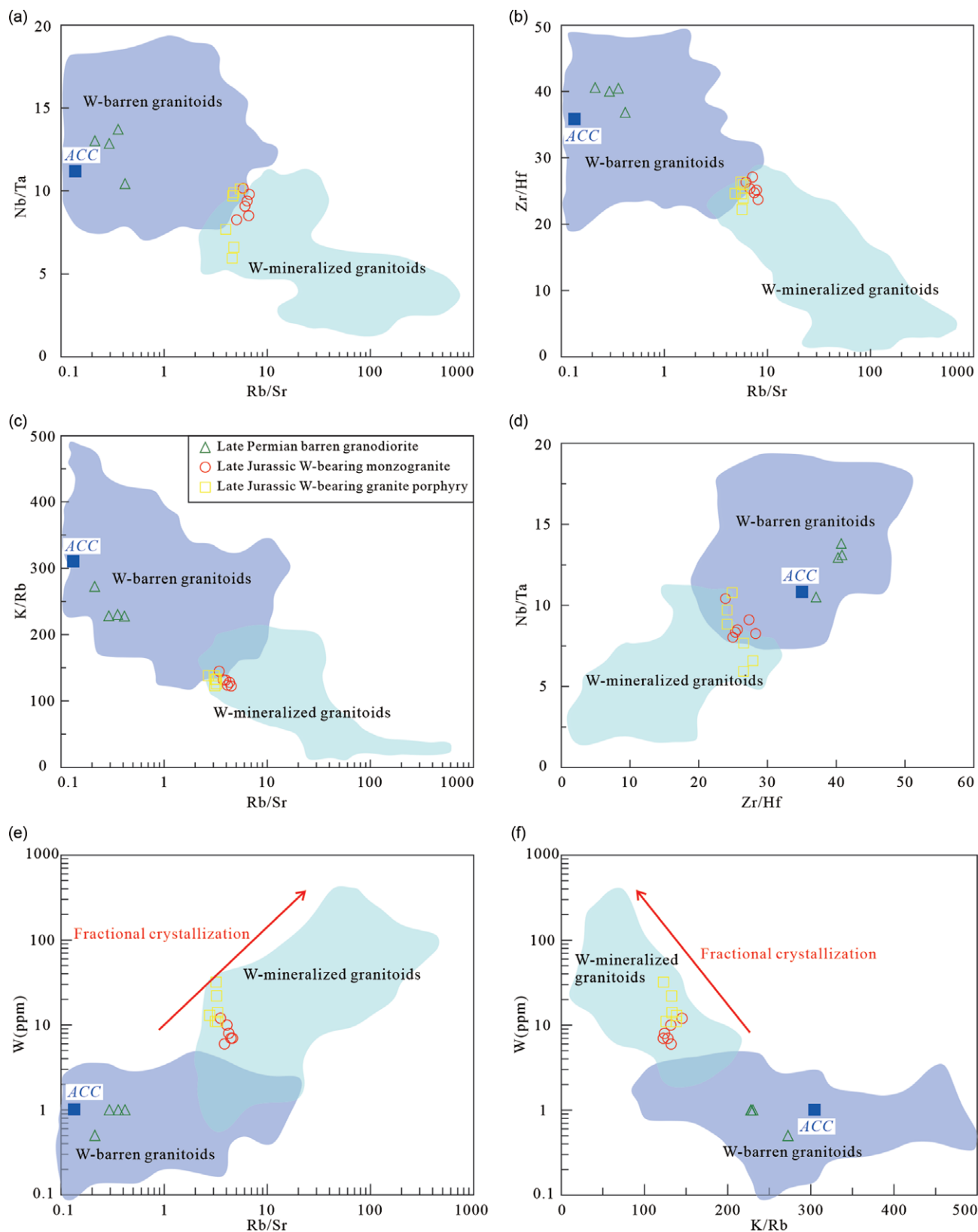
Fig. 12. (Colour online) Discrimination diagrams of W-mineralized and W-barren granitoids. Field for average continental crust (ACC) is from Rudnick & Gao (2003), and fields for W-mineralized and W-barren granitoids are from Xie *et al.* (2021).

Wood & Samson, 2000). Under the effect of temperature and pressure gradients, the ore-bearing hydrothermal fluid would have risen along a series of NE-trending faults. Infiltration and metasomatism occurred continuously between the W-bearing hydrothermal fluids and wall-rock, finally leading to the precipitation of W due to the variation in physical and chemical conditions.
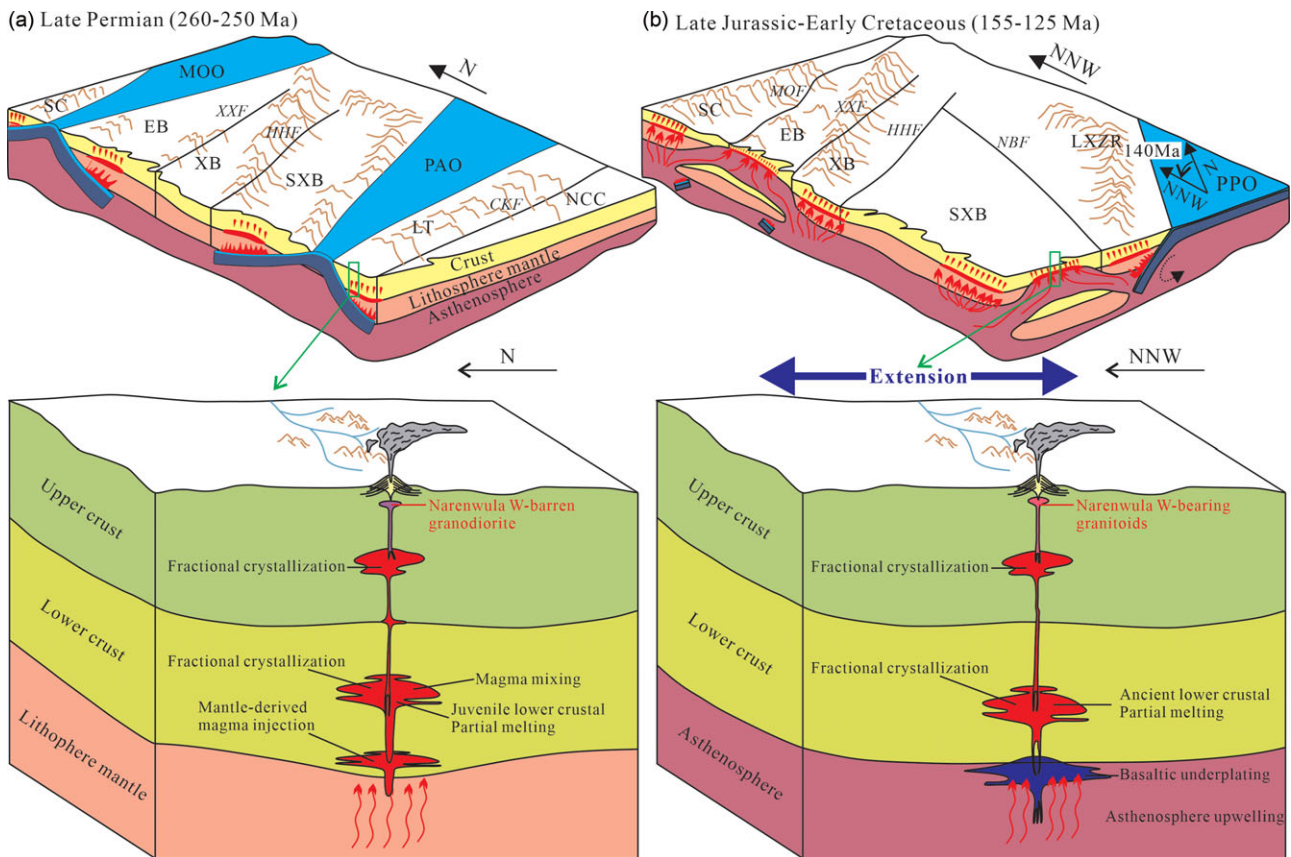
Fig. 13. (Colour online) Simplified cartoon showing tectonic evolution of NE China during late Permian and Late Jurassic – Early Cretaceous times, and the genetic model of the Narenwula complex (after Han *et al.* 2021). Abbreviations: SC – Siberian Craton; EB – Erguna Block; XB – Xing'an Block; SXB – Songliao–Xilinhot Block; LT – Liaoyuan Terrane; NCC – North China Craton; LXZR – Lesser Xing'an–Zhangguangcai Range; PAO – Palaeo-Asian Ocean; MOO – Mongol–Okhotsk Ocean; PPO – Palaeo-Pacific Ocean; MOF – Mongolia–Okhotsk Fault; XXF – Xinlin–Xiguitu Fault; HHF – Heganshan–Heihe Fault; NBF – Nenjiang–Balihan Fault; CKF – Chifeng–Kangbao Fault.

5.e. Tectonic implications

During late Permian and Late Jurassic – Early Cretaceous times, NE China experienced the overprinting of the PAO, MOO and PPO tectonic regimes; the tectonomagmatic evolution of NE China is therefore complicated, with substantial long-term debates (Wu *et al.* 2011; Liu, Y. J. *et al.* 2017; Guo *et al.* 2019). Our interpretations and previous studies provide some evidence that can elucidate the tectonic evolution of the SGB during late Permian and Late Jurassic – Early Cretaceous times.

5.e.1. Late Permian (260–250 Ma)

Although the disappearance of the PAO occurred along the SXCF, the closure time of the PAO remains ambiguous (Eizenhöfer *et al.* 2014; Liu, Y. J. *et al.* 2017). Liu, Y. J. *et al.* (2017) systematically summarized the available reported data and different models for the Palaeozoic tectonic evolution of the easternmost CAOB, concluding that the final closure of the PAO occurred along the SXCF with a scissor-style closure from late Permian – Early Triassic times in the west to late Permian – Middle Triassic times in the east (Fig. 13a). The presence of collision-related granites (Chen *et al.* 2009), the Xilingol Complex and terrestrial Linxi Formation deposition provide evidence for these conclusions (Li, Y. L. *et al.* 2014). In addition, middle Permian – Early Triassic syncollisional granitoids in the eastern Jilin belt (Cao *et al.* 2013) and Triassic mafic volcanic rocks and lacustrine molasses in the SGB (Zhang, J. H. *et al.* 2008) have been discovered.

These findings, combined with the late Permian I-type granitoids along the SXCF, granodiorites in the Baiyinnuoer area (SGB; 245 Ma) (Jiang *et al.* 2017), Early–Middle Triassic syncollisional S-type granitoids in Linxi (SGB) and Horqin Right-Wing Middle Banner (CGB), and synchronous adakitic plutons in the Yanbian fold belt (251−240 Ma) (Ma *et al.* 2017) suggest that the parental magmas of the granitoids in this area formed via the melting of a thickened lower crust as a result of the amalgamation of the NE China block and NCC during the subduction of the PAO (Fig. 13a). The late Permian I-type granodiorites from the Narenwula complex show normal arc magma characteristics, derived from the mixing of mantle-derived mafic melts and crust-derived felsic melts, and may have formed under a volcanic arc setting triggered by the subduction of the PAO plate (Fig. 13a). Shang (2004) reported radiolarians found in the argillite bed of the Zhesi Formation from the middle Permian in the Zhesi and Xilinhot areas. This indicates that deep marine sedimentary facies persisted during middle Permian time and suggests that the ocean between the NCC and Siberian Craton (SC), probably extending along the Linxi ophiolite belt, was not closed until late Guadalupian time (~270–250 Ma). Han *et al.* (2015) reported a youngest detrital zircon U–Pb age of 238 Ma from the Linxi Formation in the Linxi area (Fig. 1c), indicating that the final closure of the PAO occurred in Early Triassic time. Detrital zircon U–Pb dating of the Xingfuzhilu Formation in southern Inner Mongolia suggested that a closing remnant ocean basin or narrow seaway possibly existed in middle Permian time immediately prior

to the final collision of the CAOB and closure of the PAO (Li, S. *et al.* 2014). The Wudaoshimen ophiolite in Keshenketengqi (SGB) composed of pillow basalt yielded a concordant age of 277 Ma (Wang *et al.* 2014), indicating that an open ocean still existed in the north of the NCC. Reported palaeomagnetic data provide further constraints on the final closure of the PAO. According to the palaeomagnetic data, Li *et al.* (2006) concluded that the SC began to drift southwards rapidly in early Permian time and collided with the NCC at the end of the Permian period (*c.* 250 Ma). Rock magnetic and palaeomagnetic studies of the Permian sandstone from the Taohaiyingzi area in Inner Mongolia indicated that the area amalgamated with the NCC in late Permian time (Qin *et al.* 2013).

The studies above clearly indicate that the PAO closure had a long history throughout Palaeozoic time until early Mesozoic time, which involved subduction/accretion processes on the northern margin of the NCC and the southern margin of the SGB during Palaeozoic time and a final collision along the SXCF during late Permian – Early Triassic times in the west.

5.e.2. Late Jurassic – Early Cretaceous (155–125 Ma)

Romer & Kroner (2016) concluded that the occurrence of Sn and/ or W mineralization is the result of a sequence of processes, i.e. source enrichment, source accumulation and metal extraction. In the process of metal extraction, different tectonic settings may have led to the input of mantle melt or the emplacement of ultrahigh-temperature metamorphic rocks, which were essential for metal extraction from the source rocks. These factors played an important role in controlling the discontinuous distribution of W mineralization within the belt. Therefore, understanding the tectonic setting and deep geodynamic processes is crucial for deciphering the W mineralization mechanisms in the Narenwula area and the SGB.

It is generally accepted that the SGB and all of NE China was under an extensional setting during Late Jurassic – Early Cretaceous times (Wu *et al.* 2011; Ouyang *et al.* 2015; Mao *et al.* 2020; Wei *et al.* 2021; Zhang, G. L. *et al.* 2020; Jing *et al.* 2021). The widespread metamorphic core complexes (Wang *et al.* 2011, 2012) combined with the occurrence of bimodal rock suites, A-type granites (Gou *et al.* 2019; Han *et al.* 2021; Zhang, C. *et al.* 2020), alkaline rhyolites, extensional basins and some Au–Mo–REE mineralization in the SGB (Wu *et al.* 2005; Guo *et al.* 2017; Li *et al.* 2017) also indicate a Late Jurassic – Early Cretaceous extensional setting. Some geophysical data also provide constraints for the extensional setting. Shao *et al.* (2005) reported electromagnetic anomalies in the SGB and revealed two low-resistivity layers in the crust, at depths of ~10 and 30 km. Seismic tomography studies indicated the existence of an ~100–500 km thick low-velocity block at a depth of ~50–100 km beneath the SGB, broadly coincident with the electromagnetic data (Huang & Zhao, 2006), which can be interpreted as upwelling asthenosphere. Several high-velocity blocks have been found beneath a depth of 400 km (one as deep as 1000 km), and a low-velocity atypical plume-like block was identified rising from below 800–1000 km (Shao *et al.* 2005). These findings provided evidence of the occurrence of lithospheric delamination and asthenospheric upwelling beneath the SGB (Wan *et al.* 2019). However, the deep geodynamic processes that led to the widespread extension and abundant W-related granitic magmatism remain contentious.

A mantle plume model was initially proposed to explain the extensive late Mesozoic magmatism (Ge *et al.* 1999). However, this model was later abandoned because late Mesozoic magmatism in the Great Xing'an Range (GXR) lasted for a relatively long period

of time (40 Ma), distinguishing it from the short-lived intense period of magmatic eruption expected to result from a mantle plume (Wu *et al.* 2011). More recent studies have suggested a genetic relationship between the late Mesozoic magmatism in NE China and the subduction of the PPO (Ji *et al.* 2019; Li, S. Z. *et al.* 2019; Suo *et al.* 2019; He *et al.* 2020; Sun *et al.* 2020; Wang, L. *et al.* 2020; Wei *et al.* 2020; Jing *et al.* 2021). However, this scenario can be precluded because (1) late Mesozoic SGB magmatism likely occurred far from (> 2000 km) the PPO subduction front, whereas the maximum extent of the PPO plate subduction is evaluated as 1300 km (Wan *et al.* 2019); (2) seismological studies suggest that back-arc extension led by the PPO subduction did not reach the late Mesozoic SGB (Li *et al.* 2017); and (3) during Late Jurassic time, igneous rocks were mainly distributed in the GXR and absent in other regions of NE China, indicating that the PPO plate was rotating and undergoing oblique subduction beneath the Eurasian continent during this time (Maruyama *et al.* 1997; Xu, W. L. *et al.* 2013).

In this study, we favour the pattern that the SGB was affected by the combined effects resulting from the closure of the MOO and subduction of the PPO during late Mesozoic time (Ouyang *et al.* 2015; Liu, C. F. *et al.* 2017; Liu *et al.* 2020; Pang *et al.* 2020; Zhang, C. *et al.* 2020; Mi *et al.* 2021). A series of strike-slip faults developed along the Eurasian plate boundaries during Late Jurassic and Early Cretaceous times (Khanchuk, 2001). A simultaneous quiescence in volcanism at 160−140 Ma in the KJB (Xu, W. L. *et al.* 2013; Ma *et al.* 2017) implies N-dipping subduction of the PPO plate (Fig. 13b) (Abrajevitch *et al.* 2012). In addition, the southeastward younging trend of volcanic rocks in NE China, from Late Jurassic time (160 Ma) to Late Cretaceous time (80 Ma), indicates that Early Cretaceous rocks are related to the rollback of the subducted PPO plate (Wang *et al.* 2006). Furthermore, a change in the PPO plate subduction direction towards the NNW occurred at 140 Ma (Fig. 13b) (Maruyama *et al.* 1997; Ma *et al.* 2017), together with the rollback of the subducting plate (Ji *et al.* 2020). Tang *et al.* (2019) suggested that the force resulting from the southward subduction of the MOO plate and subsequent asthenosphere upwelling could be the dynamic mechanisms that initiated the rollback of the PPO plate. The rollback likely caused large-scale lithosphere delamination and asthenosphere upwelling (Fig. 13b), which consequently caused large-scale magmatic activity, ore mineralization and lithospheric thinning in NE China (Ouyang *et al.* 2015).

The MOO formed between the SC and NCC in late Palaeozoic time (Tomurtogoo *et al.* 2005). At that time, the SC rotated clockwise relative to Mongolia, which resulted in the closure of the MOO and the formation of the MO suture belt (Zorin, 1999). The western part of the ocean was closed during Triassic time, and the central part closed during Early–Middle Jurassic time (Li *et al.* 2015). However, the exact closure time of the eastern part of the ocean remains controversial, with suggestions including Early–Middle Jurassic (Zorin, 1999; Tomurtogoo *et al.* 2005), Late Jurassic – Early Cretaceous (Kravchinsky *et al.* 2002) and Early Cretaceous (Ren *et al.* 2016). Regardless of the timing of closure, a substantial number of studies have indicated that the late Mesozoic extensional setting in the SGB is related to post-orogenic gravitational collapse and/or subduction-induced back-arc extension related to the closure of the MOO (Wang, Z. H. *et al.* 2015; Fritzell *et al.* 2016; Guan *et al.* 2018; Ji *et al.* 2018, 2020; Han *et al.* 2021; Shi *et al.* 2020; Wei *et al.* 2021). On Rb versus (Y + Nb) and (Yb + Ta) diagrams, most Late Jurassic W-bearing granitoids in this study and late Mesozoic W-related granitoids from previous studies plot in the post-collision granite field (Fig. 14a, b). On an R2 versus R1 diagram (Fig. 14c) as well as
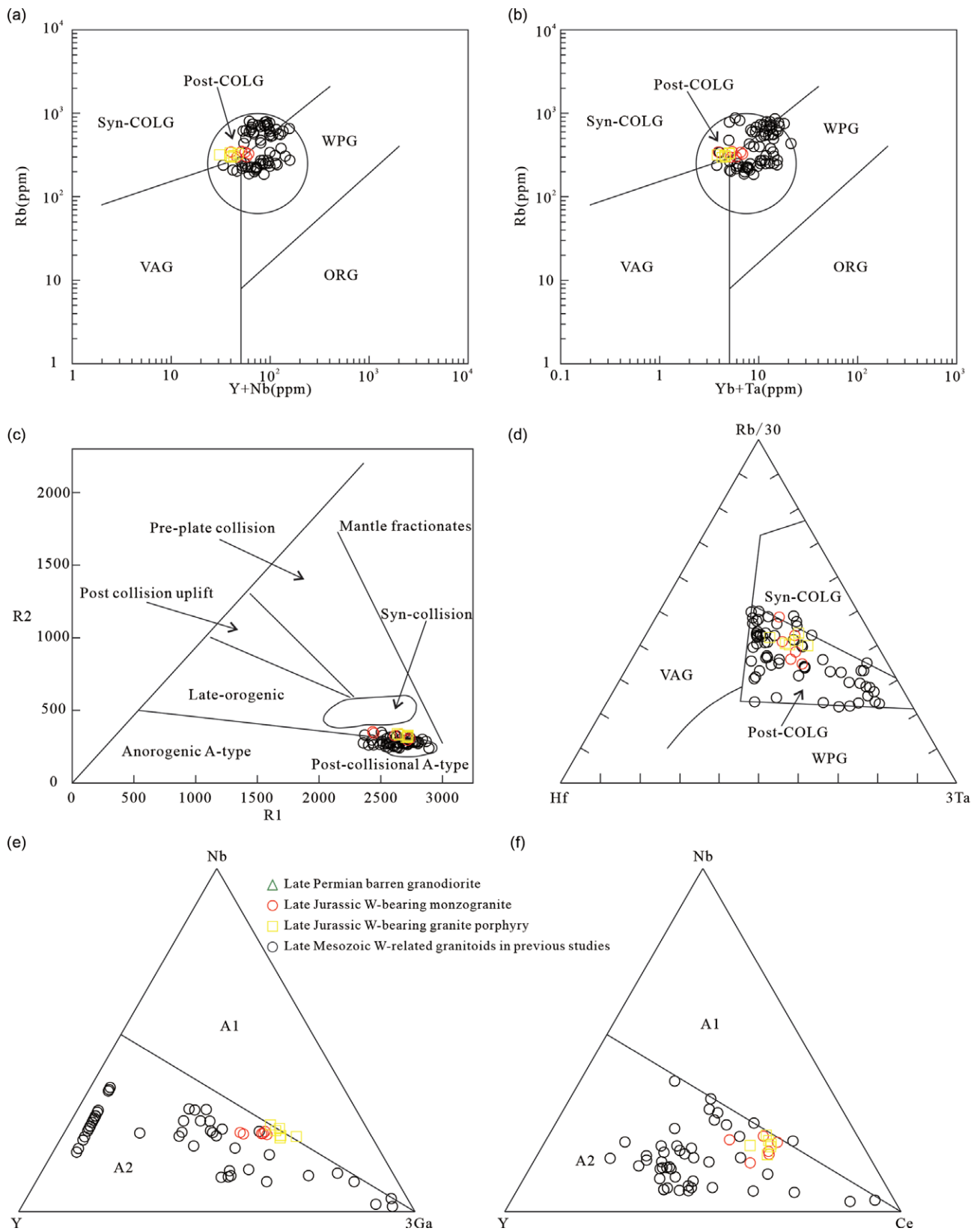
Fig. 14. (Colour online) (a) Rb versus (Y + Nb) diagram (after Pearce *et al.* 1984). (b) Rb versus (Yb + Ta) diagram (after Pearce *et al.* 1984). (c) R2 versus R1 diagram (after Batchelor & Bowden, 1985). (d) Rb/30–Hf–3Ta discrimination diagram (after Harris *et al.* 1986). (e) Nb–Y–3Ga discrimination diagram (after Eby, 1992). (f) Nb–Y–Ce discrimination diagram (after Eby, 1992). Abbreviations: VAG – volcanic arc granite; ORG – ocean ridge granite; WPG – within-plate granite; Syn-COLG – syncollision granite; Post-COLG – post-collision granite; A1 – anorogenic A-type granites; A2 – post-collisional A-type granites. Data for the late Mesozoic W-related granitoids in the southern Great Xing'an Range belt from other studies are listed in online Supplementary Material Table S2.

on the Rb/30–Hf–3Ta diagram (Fig. 14d), most samples plot in the post-collisional A-type granite field. Similarly, on Nb–Y–3Ga/Ce diagrams (Eby, 1992), most samples plot in the A2-type granite field, representing post-collisional A-type granites (Fig. 14e, f). Collectively, we suggest that the Late Jurassic W-bearing granitoids from the Narenwula complex and late Mesozoic W-related granitoids in the SGB were emplaced under a post-collisional setting instead of a subduction-dominated setting. Furthermore, this evidence indicates that the MOO tectonic regime played a critical role in the formation of the late Mesozoic W-related granitoids in the SGB.

During late Mesozoic time, a plate tear developed because the MOO plate could not subduct owing to its older age, as predicted by the petrological and geochemical constraints (Ouyang *et al.* 2015). In contrast, when the young PPO plate subducted, a long segment of the plate was temporarily stagnant in the transition zone between the upper and lower mantle (Liu & Stegman, 2012). The juxtaposition of the cold PPO plate against the hot mantle generated small-scale thermal upwelling along the edges of the plate (Liu & Stegman, 2012). Owing to the forces generated by the MOO plate break-off and subsequent asthenospheric upwelling, the PPO plate began to roll back, rather than continuing to subduct (Ouyang *et al.* 2015). Consequently, the MOO plate tear in Late Jurassic time resulted in rapid asthenospheric upwelling and lithospheric thinning. The continuous rollback of the PPO plate, induced by the MOO plate tear, also triggered large-scale upwelling of the asthenosphere, lithospheric thinning and delamination, and back-arc spreading (Fig. 13b). These resulted in the generation of large-scale post-orogenic W-related granitic magmas and associated W deposits in the SGB during this period.

In summary, we suggest that the late Mesozoic W-related granitoids and associated W deposits in the SGB formed in a post-orogenic extensional setting induced by the closure of the MOO and rollback of the PPO plate.

6. Conclusions

(1) Our new LA-ICP-MS zircon U–Pb ages indicate that the MMEs and host granodiorites are coeval, with similar late Permian crystallization ages of 258.5–253.9 Ma, while W-bearing monzogranite and granite porphyry formed during Late Jurassic time, dated at 149.8–148.1 Ma.

(2) The late Permian granodiorites exhibit the characteristics of I-type granite. The MMEs and host granodiorites formed by the magma mixing of mafic and felsic magmas. The felsic magma was derived from the partial melting of juvenile lower crust, while the mafic magma was derived from the partial melting of an enriched lithospheric mantle metasomatized by slab-derived fluids.

(3) The Late Jurassic W-bearing granitoids are highly fractionated A-type granites, mainly derived from the partial melting of an ancient lower crust that subsequently underwent extreme fractional crystallization processes.

(4) In contrast to the W-barren granodiorite, the W-bearing granitoids are characterized by high W concentrations and Rb/Sr ratios, and low Nb/Ta, Zr/Hf and K/Rb ratios. Extreme fractional crystallization is critical for W enrichment in the granitic magma. The granodiorites did not induce W mineralization, likely attributable to their low fractionated signatures.

(5) The late Permian granodiorites formed in a volcanic arc setting related to the southward subduction of the PAO, whereas the Late Jurassic W-bearing granitoids and related W deposits formed in a post-orogenic extensional setting related to the MOO closure and rollback of the PPO plate.

References

Abrajevitch A, Zyabrev S, Didenko AN and Kodama K (2012) Palaeomagnetism of the West Sakhalin Basin: evidence for northward displacement during the Cretaceous. *Geophysical Journal International* **190**, 1439–54.

Annen C, Blundy JD and Sparks RSJ (2006) The genesis of intermediate and silicic magmas in deep crustal hot zones. *Journal of Petrology* **47**, 505–39.

Arevalo RJ and McDonough WF (2008) Tungsten geochemistry and implications for understanding the earth's interior. *Earth and Planetary Science Letters* **272**, 656–65.

Ballouard C, Poujol M, Boulvais P, Branquet Y, Tartese R and Vigneresse JL (2016) Nb–Ta fractionation in peraluminous granites: a marker of magmatic-hydrothermal transition. *Geology* **3**, 231–4.

Barbarin B (2005) Mafic magmatic enclaves and mafic rocks associated with some granitoids of the central Sierra Nevada batholith, California: nature, origin, and relations with the hosts. *Lithos* **88**, 155–77.

Batchelor RA and Bowden VP (1985) Petrogenetic interpretation of granitoids rock series using multicationic parameters. *Chemical Geology* **48**, 43–55.

Bau M (1996) Controls on the fractionation of isovalent trace elements in magmatic and aqueous systems: evidence from Y/Ho, Zr/Hf, and lanthanide tetrad effect. *Contributions to Mineralogy and Petrology* **123**, 323–33.

Bedard JH (1990) Enclaves from the A-type granite of the Megantic Complex, White Mountain magma series: clues to granite magmagenesis. *Journal of Geophysical Research* **1990**, 17797–819.

Belousova EA, Griffin WL, O'Reilly SY and Fisher NI (2002) Igneous zircon: trace element composition as an indicator of source rock type. *Contributions to Mineralogy and Petrology* **143**, 602–22.

Berzina AP, Berzina AN and Gimon VO (2014) Geochemical and Sr–Pb–Nd isotopic characteristics of the Shakhtama porphyry Mo–Cu system (Eastern Transbaikalia, Russia). *Journal of Asian Earth Sciences* **79**, 655–65.

Bonin B (2004) Do coeval mafic and felsic magmas in post-collisional to within-plate regimes necessarily imply two contrasting mantle and crustal sources? A review. *Lithos* **78**, 1–24.

Bonin B (2007) A-type granites and related rocks: evolution of a concept, problems and prospects. *Lithos* **97**, 1–29.

Bouvier A, Vervoort JD and Patchett PJ (2008) The Lu–Hf and Sm–Nd isotopic composition of CHUR, constraints from unequilibrated chondrites and implications for the bulk composition of terrestrial planets. *Earth and Planetary Science Letters* **273**, 48–57.

Breiter K, Müller A, Leichmann J and Gabašová A (2005) Textural and chemical evolution of a fractionated granitic system: the Podlesí stock, Czech Republic. *Lithos* **80**, 323–45.

Cao JY, Wu QH, Yang XY, Deng XT, Li H, Kong H and Xi XS (2020) Geochemical factors revealing the differences between the Xitian and Dengfuxian composite plutons, middle Qin-Hang Belt: implications to the W–Sn mineralization. *Ore Geology Reviews* **118**, 103353. doi: 10.1016/j.oregeorev.2020.103353.

Cao HH, Xu WL, Pei FP, Wang ZW, Wang F and Wang ZJ (2013) Zircon U–Pb geochronology and petrogenesis of the Late Paleozoic–Early Mesozoic intrusive rocks in the eastern segment of the northern margin of the North China Block. *Lithos* **170–171**, 191–207.

Cao JY, Yang XY, Du JG, Wu QH, Kong H, Li H, Wan Q, Xi XS, Gong YS and Zhao HR (2018) Formation and geodynamic implication of the Early

Yanshanian granites associated with W–Sn mineralization in the Nanling range, South China: an overview. *International Geology Review* 60, 1744–71.

Castro A, Patiño Douce AE, Corretgé LG, De La Rosa JD, El-Biad M and El-Hmidi H (1999) Origin of peraluminous granites and granodiorites, Iberian Massif, Spain: an experimental test of granite petrogenesis. *Contributions to Mineralogy and Petrology* 135, 255–76.

Chappell BW (1996) Magma mixing and the production of compositional variation within granite suites: evidence from the granites of southeastern Australia. *Journal of Petrology* 37, 449–70.

Chappell BW (1999) Aluminium saturation in I- and S-type granites and the characterization of fractionated haplogranites. *Lithos* 46, 535–51.

Chappell BW and White AJR (1992) I-and S-type granites in the Lachlan Fold Belt. *Earth and Environmental Science Transactions of the Royal Society of Edinburgh* 83, 1–26.

Chappell BW, White AJR and Wyborn D (1987) The importance of residual source material in granite petrogenesis. *Journal of Petrology* 28, 1111–38.

Che XD, Linnen RL, Wang RC, Aseri A and Thibault Y (2013) Tungsten solubility in evolved granitic melts: an evaluation of magmatic wolframite. *Geochimica et Cosmochimica Acta* 106, 84–98.

Chen B, Jahn BM and Tian W (2009) Evolution of the Solonker suture zone: constraints from zircon U–Pb ages, Hf isotopic ratios and whole-rock Sr–Nd isotope compositions of subduction and collision-related magmas and forearc sediments. *Journal of Asian Earth Sciences* 34, 245–57.

Chen B, Jahn BM, Wilde S and Xu B (2000) Two contrasting Paleozoic magmatic belts in northern Inner Mongolia, China: petrogenesis and tectonic implications. *Tectonophysics* 328, 157–82.

Chen YD, Price RC and White AJR (1989) Inclusions in three S-type granites from southeastern Australia. *Journal of Petrology* 30, 1181–218.

Chen GZ, Wu G, Li TG, Liu RL, Wu LW, Zhang PC, Zhang T and Chen YC (2018) LA-ICP-MS zircon and cassiterite U–Pb ages of Daolundaba copper-tungsten-tin deposit in Inner Mongolia and their geological significance. *Mineral Deposits* 37, 225–45 (in Chinese with English abstract).

Claiborne LL, Miller CF, Walker BA, Wooden JL, Mazdab FK and Bea F (2006) Tracking magmatic processes through Zr/Hf ratios in rocks and Hf and Ti zoning in zircons: an example from the Spirit Mountain batholith, Nevada. *Mineralogical Magazine* 70, 517–43.

Clemens JD, Holloway JR and White AJR (1986) Origin of an A-type granite: experimental constraints. *American Mineralogist* 71, 317–24.

Clemens JD and Stevens G (2012) What controls chemical variation in granitic magmas? *Lithos* 134–135, 317–29.

Clemens JD and Wall VJ (1988) Controls on mineralogy of S-type volcanic and plutonic rocks. *Lithos* 21, 53–66.

Collins WJ, Beams SD, White AJR and Chappell BW (1982) Nature and origin of A-type granites with particular reference to southeastern Australia. *Contributions to Mineralogy and Petrology* 80, 189–200.

Collins WJ, Wiebe R, Healy B and Richards S (2006) Replenishment, crystal accumulation and floor aggradation in the megacrystic Kameruka Suite, Australia. *Journal of Petrology* 47, 2073–104.

Deering CD and Bachmann O (2010) Trace element indicators of crystal accumulation in silicic igneous rocks. *Earth and Planetary Science Letters* 297, 324–31.

Defant MJ and Drummond MS (1990) Derivation of some modern arc magmas by melting of young subducted lithosphere. *Nature* 347, 662–5.

Didier J (1973) *Granites and their Enclaves: The Bearing of Enclaves on the Origin of Granites*. Amsterdam: Elsevier, 393 pp.

Dodge FCW and Kistler RW (1990) Some additional observations on inclusions in the granitic rocks of the Sierra Nevada. *Journal of Geophysical Research: Solid Earth* 95, 17841–48.

Dostal J and Chatterjee AK (2000) Contrasting behavior of Nb/Ta and Zr/Hf ratios in a peraluminous granitic pluton (Nova Scotia, Canada). *Chemical Geology* 163, 207–18.

Dostal J, Kontak DJ, Gerel O, Gregory SJ and Fayek M (2015) Cretaceous ongonites (topaz-bearing albite-rich microleucogranites) from Ongon Khairkhan, Central Mongolia: products of extreme magmatic fractionation and pervasive metasomatic fluid: rock interaction. *Lithos* 236–237, 173–89.

Eby GN (1992) Chemical subdivision of the A-type granitoids: petrogenetic and tectonic implications. *Geology* 20, 641–44.

Eizenhöfer PR, Zhao GC, Zhang J and Sun M (2014) Final closure of the Paleo-Asian Ocean along the Solonker suture zone: constraints from geochronological and geochemical data of Permian volcanic and sedimentary rocks. *Tectonics* 33, 441–63.

El Bouseily AM and El Sokkary AA (1975) The relation between Rb, Ba and Sr in granitic rocks. *Chemical Geology* 16, 207–19.

Elburg MA (1996) Evidence of isotopic equilibration between microgranitoid enclaves and host granodiorite, Warburton granodiorite, Lachlan Fold Belt, Australia. *Lithos* 38, 1–22.

Fei XH, Zhang ZC, Cheng ZG, Santosh M, Jin ZL, Wen BB, Li ZX and Xu LJ (2018) Highly differentiated magmas linked with polymetallic mineralization: a case study from the Cuihongshan granitic intrusions, Lesser Xing'an Range, NE China. *Lithos* 302–303, 158–77.

Feng ZQ, Liu YJ, Li L, Jin W, Jiang LW, Li WM, Wen QB and Zhao YL (2019) Geochemical and geochronological constraints on the tectonic setting of the Xinlin ophiolite, northern Great Xing'an Range, NE China. *Lithos* 326–327, 213–29.

Fogliata AS, Baez MA, Hagemann SG, Santos JO and Sardi F (2012) Post-orogenic, Carboniferous granite-hosted Sn–W mineralization in the Sierras Pampeanas Orogen, Northwestern Argentina. *Ore Geology Reviews* 45, 16–32.

Fritzell EH, Bull AL and Shephard GE (2016) Closure of the Mongol-Okhotsk Ocean: insights from seismic tomography and numerical modelling. *Earth and Planetary Science Letters* 445, 1–12.

Frost BR, Barnes CG, Collins WJ, Arculus RJ, Ellis DJ and Frost CD (2001) A geochemical classification for granitic rocks. *Journal of Petrology* 42, 2033–48.

Gao X, Zhou Z, Breiter K, Ouyang H and Liu J (2019) Ore-formation mechanism of the Weilasituo tin–polymetallic deposit, NE China: constraints from bulk-rock and mica chemistry, He–Ar isotopes, and Re–Os dating. *Ore Geology Reviews* 109, 163–83.

Ge WC, Lin Q, Sun DY, Wu FY, Yuan ZK, Li WY, Chen MZ and Yin CX (1999) Geochemical characteristics of the Mesozoic basalts in Da Hinggan Ling: evidence of the mantle-crust interaction. *Acta Petrologica Sinica* 15, 396–406 (in Chinese with English abstract).

Gibert F, Moine B, Schott J and Dandurand JL (1992) Modeling of the transport and deposition of tungsten in the scheelite-bearing calc-silicate gneisses of the Montagne Noire, France. *Contributions to Mineralogy and Petrology* 112, 371–84.

Gou J, Sun DY and Qin Z (2019) Late Jurassic–Early Cretaceous tectonic evolution of the Great Xing'an Range: geochronological and geochemical evidence from granitoids and volcanic rocks in the Erguna Block, NE China. *International Geology Review* 61, 1842–63.

Green TH (1995) Significance of Nb/Ta as an indicator of geochemical processes in the crust-mantle system. *Chemical Geology* 120, 347–59.

Griffin WL, Wang X, Jackson SE, Pearson SE, O'Reilly SY, Xu XS and Zhou XM (2002) Zircon chemistry and magma genesis, SE China: in-situ analysis of Hf isotopes, Tonglu and Pingtan igneous complexes. *Lithos* 61, 237–69.

Guan QB, Liu ZH, Wang B, Wang X, Wang XA, Shi Q and Chen YS (2018) Middle Jurassic−Early Cretaceous tectonic evolution of the Bayanhushuo area, southern Great Xing'an Range, NE China: constraints from zircon U–Pb geochronology and geochemical data of volcanic and subvolcanic rocks. *International Geology Review* 60, 1883–905.

Guo F, Huang MW and Zhao L (2019) Nd–Hf–O isotopic evidence for subduction-induced crustal replacement in NE China. *Chemical Geology* 525, 125–42.

Guo ZJ, Li JW, Chang YL, Han ZG, Dong XZ, Yang YC, Tian J, She HQ, Xiang AP and Kang YJ (2015) Genetic types and ore-forming geological significance of granites in the Honghuaerji scheelite deposit, Inner Mongolia. *Acta Petrologica et Mineralogica* 34, 322–42 (in Chinese with English abstract).

Guo ZX, Yang YT, Zyabrev S and Hou ZH (2017) Tectonostratigraphic evolution of the Mohe-upper Amur Basin reflects the final closure of the Mongol-Okhotsk Ocean in the latest Jurassic-earliest Cretaceous. *Journal of Asian Earth Sciences* 145, 494–511.

Han SJ, Wang X, Wang X, Wang Y and Zhang Y (2021) Geochronology and geochemistry of late Jurassic–Early Cretaceous volcanic rocks in the southern Great Xing'an range, NE China: constraints for late Mesozoic

tectono-magmatic evolution. *International Geology Review* 63, 1366–88. doi: 10.1080/00206814.2020.1768442.

Han J, Zhou JB, Wang B and Cao JL (2015) The final collision of the CAOB: constraint from the zircon U–Pb dating of the Linxi Formation, Inner Mongolia. *Geoscience Frontiers* 6, 211–25.

Harlaux M, Mercadier J, Marignac C, Peiffert C, Cloquet C and Cuney M (2018) Tracing metal sources in peribatholitic hydrothermal W deposits based on the chemical composition of wolframite: the example of the Variscan French Massif Central. *Chemical Geology* 479, 58–85.

Harris NB, Pearce JA and Tindle AG (1986) Geochemical characteristics of collision-zone magmatism. In *Collision Tectonics* (eds MP Coward and AC Reis), pp. 67–81. Geological Society of London, Special Publication no. 19.

He XH, Tan SC, Liu Z, Bai ZJ, Wang XC, Wang YC and Zhong H (2020) Petrogenesis of the Early Cretaceous Aolunhua adakitic monzogranite porphyries, Southern Great Xing'an Range, NE China: implication for geodynamic setting of Mo mineralization. *Minerals* 10, 332–52.

Hirose K (1997) Melting experiments on lherzolite KLB-1 under hydrous conditions and generation of high-magnesian andesite melts. *Geology* 25, 42–4.

Hou KJ, Li YH, Zou TR, Qu XM, Shi YR and Xie GQ (2007) Laser ablation-MC-ICP-MS technique for Hf isotope microanalysis of zircon and its geological applications. *Acta Petrologica Sinica* 23, 2595–604 (in Chinese with English abstract).

Hu XL, Ding ZJ, He MC, Yao SZ, Zhu BP, Shen J and Chen B (2014) Two epochs of magmatism and metallogeny in the Cuihongshan Fe-polymetallic deposit, Heilongjiang Province, NE China: constrains from U–Pb and Re–Os geochronology and Lu–Hf isotopes. *Journal of Geochemical Exploration* 143, 116–26.

Huang LC and Jiang SY (2014) Highly fractionated S-type granites from the giant Dahutang tungsten deposit in Jiangnan orogen, southeast China: geochronology, petrogenesis and their relationship with W-mineralization. *Lithos* 202–203, 207–26.

Huang JL and Zhao DP (2006) High-resolution mantle tomography of China and surrounding regions. *Journal of Geophysical Research* 111, B09305. doi: 10.1029/2005JB004066.

IMBGMED (Inner Mongolian Bureau of Geology and Mineral Exploration and Development) (2016) *Prospecting Report of Narenwula W-Bi-Ag Polymetallic Deposit at Xianghuang Banner, Inner Mongolia Autonomous Region County.* Beijing: Geological Publishing House, 265 pp. (in Chinese).

IMBGMR (Inner Mongolian Bureau of Geology Mineral Resources) (1991) *Regional Geology of Inner Mongolia.* Beijing: Geological Publishing House, 725 pp. (in Chinese).

Jiang SH, Bagas L, Hu P, Han N, Chen CL, Liu Y and Kang H (2016) Zircon U–Pb ages and Sr–Nd–Hf isotopes of the highly fractionated granite with tetrad REE patterns in the Shamai tungsten deposit in eastern Inner Mongolia, China: implications for the timing of mineralization and ore genesis. *Lithos* 261, 322–39.

Jiang SH, Chen CL, Bagas L, Liu Y, Han N, Kang H and Wang ZH (2017) Two mineralization events in the Baiyinnuoer Zn–Pb deposit in Inner Mongolia China: evidence from field observations, S–Pb isotopic compositions and U–Pb zircon ages. *Journal of Asian Earth Sciences* 144, 339–67.

Jiang H, Jiang SY, Li WQ, Zhao KD and Peng NJ (2018) Highly fractionated Jurassic I-type granites and related tungsten mineralization in the Shirenzhang deposit, northern Guangdong, south China: evidence from cassiterite and zircon U–Pb ages, geochemistry and Sr–Nd–Pb–Hf isotopes. *Lithos* 312–313, 186–203.

Ji Z, Ge WC, Yang H, Wang QH, Zhang YL, Wang ZH and Bi JH (2018) Late Jurassic rhyolites from the Wuchagou region in the central Great Xing'an Range, NE China: petrogenesis and tectonic implications. *Journal of Asian Earth Sciences* 158, 381–97.

Ji D, Liu HC and Li YL (2020) Large-scale early Cretaceous lower-crust melting derived adakitic rocks in NE China: implications for convergent bidirectional subduction and slab rollback. *International Geology Review* 62, 2324–43. doi: 10.1080/00206814.2019.1697968.

Ji Z, Meng QA, Wan CB, Zhu DF, Ge WC, Zhang YL, Yang H and Dong Y (2019) Geodynamic evolution of flat-slab subduction of Paleo-Pacific Plate:

constraints from Jurassic adakitic lavas in the Hailar Basin, NE China. *Tectonics* 38, 4301–19.

Jing JH, Yang H, Ge WC, Dong Y, Ji Z, Jing Y, Bi JH and Zhou HY (2021) Early Cretaceous crust–mantle interaction linked to rollback of the Palaeo-Pacific flat-subducting slab: constraints from the intermediate–felsic volcanic rocks of the northern Great Xing'an Range, NE China. *Geological Magazine* 158, 1617–38.

Ju W and Hou G (2014) Late Permian to Triassic intraplate orogeny of the southern Tianshan and adjacent regions, NW China. *Geoscience Frontiers* 5, 83–93.

Keppler H and Wyllie PJ (1991) Partitioning of Cu, Sn, Mo, W, U, and Th between melt and aqueous fluid in the systems haplogranite-H_2O-HCl and haplogranite-H_2O-HF. *Contributions to Mineralogy and Petrology* 109, 139–50.

Kerr A and Fryer BJ (1993) Nd isotopic evidence for crust–mantle interaction in the generation of A-type granitoid suites in Labrador, Canada. *Chemical Geology* 104, 39–60.

Khanchuk AI (2001) Pre-Neogene tectonics of the Sea-of-Japan regions: a view from the Russian side. *Earth Science* 55, 275–91.

King PL, White AJR, Chappell W and Allen CM (1997) Characterization and origin of aluminous A-type granites from the Lachlan Fold Belt, Southeastern Australia. *Journal of Petrology* 38, 371–91.

Klemme S and O'Neill HS (2000) The near-solidus transition from garnet lherzolite to spinel lherzolite. *Contributions to Mineralogy and Petrology* 138, 237–48.

Kravchinsky VA, Cogné JP, Harbert WP and Kuzmin MI (2002) Evolution of the Mongol-Okhotsk Ocean as constrained by new palaeomagnetic data from the Mongol-Okhotsk suture zone, Siberia. *Geophysical Journal International* 148, 34–57.

Lehmann B (1987) Tin granites, geochemical heritage, magmatic differentiation. *Geologische Rundschau* 76, 177–85.

Lehmann B, Ishihara S, Michel H, Miller J, Rapela C, Sanchez A, Tistl M and Winkelmann L (1990) The Bolivian tin province and regional tin distribution in the Central Andes: a reassessment. *Economic Geology* 85, 1044–58.

Li S, Chung SL, Wang T, Wilde SA, Chu MF and Guo QQ (2017) Tectonic significance and geodynamic processes of large-scale Early Cretaceous granitoids magmatic events in the southern Great Xing'an Range, North China. *Tectonics* 36, 615–33.

Li R, Collins WJ, Yang JH, Blereau E and Wang H (2021) Two-stage hybrid origin of Lachlan S-type magmas: a re-appraisal using isotopic microanalysis of lithic inclusion minerals. *Lithos* 402–403, 106378. doi: 10.1016/j.lithos.2021.106378.

Li Y, Ding LL, Xu WL, Wang F, Tang J, Zhao S and Wang ZJ (2015) Geochronology and geochemistry of muscovite granite in Sunwu area, NE China: implications for the timing of closure of the Mongol-Okhotsk Ocean. *Acta Petrologica Sinica* 31, 56–66 (in Chinese with English abstract).

Li JJ, Fu C, Tang WL, Li HM, Lin YX, Zhang T, Wang SG, Zhao ZL, Dang ZC and Zhao LJ (2016) The metallogenic age of the Shamai wolframite deposit in Dong Ujimqin Banner, Inner Mongolia. *Geological Bulletin of China* 35, 524–30 (in Chinese with English abstract).

Li PW, Gao R, Guan Y and Li QS (2006) Palaeomagnetic constraints on the final closure time of Solonker-Linxi suture. *Journal of Jilin University (Earth Science Edition)* 36, 744–58 (in Chinese with English abstract).

Li J, Huang XL, Fu Q and Li WX (2021) Tungsten mineralization during the evolution of a magmatic-hydrothermal system: mineralogical evidence from the Xihuashan rare-metal granite in South China. *American Mineralogist* 106, 443–60.

Li SZ, Suo YH, Li XY, Zhou J, Santosh M, Wang PC, Wang GZ, Guo LL, Yu SY, Lan HY, Dai LM, Zhou ZZ, Cao XZ, Zhu JJ, Liu B, Jiang SH, Wang G and Zhang GW (2019) Mesozoic tectono-magmatic response in the East Asian ocean-continent connection zone to subduction of the Paleo-Pacific Plate. *Earth-Science Reviews* 192, 91–137.

Li S, Wilde SA, He ZJ, Jiang XJ, Liu RY and Zhao L (2014) Triassic sedimentation and postaccretionary crustal evolution along the Solonker suture zone in Inner Mongolia, China. *Tectonics* 33, 960–81.

Li YS, Yu XF, Mi KF, Carranza EJM, Liu JJ, Jia WB and He S (2019) Deposit geology, geochronology and geochemistry of the Gongpengzi skarn Cu–Zn–W polymetallic deposit, NE China. *Ore Geology Reviews* 109, 465–81.

Li YL, Zhou HW, Brouwer FM, Xiao WJ, Wijbrans JR, Zhao JH, Zhong ZQ and Liu HF (2014) Nature and timing of the Solonker suture of the Central Asian Orogenic Belt: insights from geochronology and geochemistry of basic intrusions in the Xilin Gol Complex, Inner Mongolia, China. *International Journal of Earth Sciences* **103**, 41–60.

Linnen RL and Keppler H (1997) Columbite solubility in granitic melts: consequences for the enrichment and fractionation of Nb and Ta in the Earth's crust. *Contributions to Mineralogy and Petrology* **128**, 213–27.

Linnen RL and Keppler H (2002) Melt composition control of Zr/Hf fractionation in magmatic processes. *Geochimica et Cosmochimica Acta* **66**, 3293–301.

Linnen RL and Williams-Jones AE (1995) Genesis of a magmatic metamorphic hydrothermal system; the Sn–W polymetallic deposits at Pilok, Thailand. *Economic Geology* **90**, 1921–35.

Litvinovsky BA, Jahn BM and Eyal M (2015) Mantle-derived sources of syenites from the A-type igneous suites-new approach to the provenance of alkaline silicic magmas. *Lithos* **232**, 242–65.

Liu ZH (2009) *Geological characteristic and origin of deposit in Cuihongshan W, Mo, Zn polymetallic deposit*. M.Sc. thesis, Jilin University, Changchun, China. Published thesis (in Chinese with English abstract).

Liu C, Deng JF, Kong WQ, Xu LQ, Zhao GC, Luo ZH and Li N (2011) LA-ICP-MS zircon U–Pb geochronology of the fine-grained granite and molybdenite Re–Os dating in the Wurinitu molybdenum deposit, Inner Mongolia, China. *Acta Geologica Sinica (English Edition)* **85**, 1057–66.

Liu YS, Gao S, Hu ZC, Gao CG, Zong KQ and Wang DB (2010) Continental and oceanic crust recycling-induced melt-peridotite interactions in the Trans-North China Orogen: U–Pb dating, Hf isotopes and trace elements in zircons from mantle xenoliths. *Journal of Petrology* **51**, 537–71.

Liu YF, Jiang SH and Bagas L (2016) The genesis of metal zonation in the Weilasituo and Bairendaba Ag–Zn–Pb–Cu–(Sn–W) deposits in the shallow part of a porphyry Sn–W–Rb system, Inner Mongolia, China. *Ore Geology Reviews* **75**, 150–73.

Liu Y, Jiang SH, Bagas L, Chen CL, Han N and Wan YY (2020) Petrogenesis and metallogenic potential of the Wulanba granite, southern Great Xing'an Range, NE China: constraints from whole-rock and apatite geochemistry. *Geological Magazine* **157**, 411–34.

Liu YJ, Li WM, Feng ZQ, Wen QB, Neubauer F and Liang CY (2017) A review of the Paleozoic tectonics in the eastern part of Central Asian Orogenic Belt. *Gondwana Research* **43**, 123–48.

Liu CH and Nie FJ (2015) Permian magmatic sequences of the Bilihe gold deposit in central Inner Mongolia, China: petrogenesis and tectonic significance. *Lithos* **231**, 35–52.

Liu LJ and Stegman DR (2012) Origin of Columbia River flood basalt controlled by propagating rupture of the Farallon slab. *Nature* **482**, 386–9.

Liu RL, Wu G, Li TG, Chen GZ, Wu LW, Zhang PC, Zhang T, Jiang B and Liu WY (2018) LA-ICP-MS cassiterite and zircon U–Pb ages of the Weilasituo tin-polymetallic deposit in the southern Great Xing'an Range and their geological significance. *Earth Science Frontiers* **25**, 183–201 (in Chinese with English abstract).

Liu CF, Zhou ZG, Tang YJ, Wu C, Li HY, Zhu Y, Jiang T, Liu WC and Ye BY (2017) Geochronology and tectonic settings of Late Jurassic – Early Cretaceous intrusive rocks in the Ulanhot region, central and southern Da Xingan Range. *Geological Magazine* **154**, 923–45.

Ludwig KR (2003) *User's Manual for Isoplot 3.00: A Geochronological Toolkit for Microsoft Excel*. Berkeley Geochronology Center, Special Publication no. 4, 70 pp.

Ma XH, Zhu WP, Zhou ZH and Qiao SL (2017) Transformation from Paleo-Asian Ocean closure to Paleo-Pacific subduction: new constraints from granitoids in the eastern Jilin-Heilongjiang Belt, NE China. *Journal of Asian Earth Sciences* **144**, 261–86.

Maas R, Nicholls IA and Legg C (1997) Igneous and metamorphic enclaves in the S-type Deddick granodiorite, Lachlan Fold Belt, SE Australia: petrographic, geochemical and Nd–Sr isotopic evidence for crustal melting and magma mixing. *Journal of Petrology* **38**, 815–41.

Maniar PD and Piccoli PM (1989) Tectonic discrimination of granitoids. *Geological Society of America Bulletin* **101**, 635–43.

Mao JW, Cheng YB, Chen MH and Franco P (2013) Major types and time–space distribution of Mesozoic ore deposits in South China and their geodynamic settings. *Mineralium Deposita* **48**, 267–94.

Mao AQ, Sun DY, Yang DG, Tang ZY, Zheng H and Liu Y (2020) Petrogenesis and tectonic implications of Early Cretaceous volcanic rocks from the Shanghulin Basin within the north-western Great Xing'an Range, NE China: constraints from geochronology and geochemistry. *Geological Journal* **55**, 3476–96.

Maruyama S, Isozaki Y, Kimura G and Terabayashi M (1997) Paleogeographic maps of the Japanese Islands: plate tectonic synthesis from 750 Ma to the present. *Island Arc* **6**, 121–42.

McDonough WF and Sun SS (1995) The composition of the earth. *Chemical Geology* **120**, 223–53.

Mei W, Lu XB, Liu Z, Tang RK, Ai ZL, Wang XD and Cisse M (2015) Geochronological and geochemical constraints on the ore-related granites in Huanggang deposit, southern Great Xing'an Range, NE China and its tectonic significance. *Geosciences Journal* **19**, 53–67.

Mi KF, Lü ZC, Zhao SJ, Yan TJ, Yu HY and Dong SY (2021) Petrogenesis and metallogenic implications of the Late Jurassic Dagayin pluton, southern Great Xing'an Range, northeast China: integrated geochronological, petrological, and geochemical constraints. *Journal of Geochemical Exploration* **220**, 106666. doi: 10.1016/j.gexplo.2020.106666.

Middlemost EAK (1994) Naming materials in the magma/igneous rock system. *Earth-Science Reviews* **37**, 215–24.

Mingram B, Trumbull RB, Littman S and Gerstenberger H (2000) A petrogenetic study of anorogenic felsic magmatism in the Cretaceous Paresis ring complex, Namibia: evidence for mixing of crust and mantle-derived components. *Lithos* **54**, 1–22.

Mushkin A, Navon O, Halicz L, Hartmann G and Stein M (2003) The petrogenesis of A-type magmas from the Amram Massif, southern Israel. *Journal of Petrology* **44**, 815–32.

Ouyang HG, Mao JW, Zhou ZH and Su HM (2015) Late Mesozoic metallogeny and intracontinental magmatism, southern Great Xing'an Range, northeastern China. *Gondwana Research* **27**, 1153–72.

Pang YM, Guo XW, Zhang XH, Zhu XQ, Hou FH, Wen ZH and Han ZZ (2020) Late Mesozoic and Cenozoic tectono-thermal history and geodynamic implications of the Great Xing'an Range, NE China. *Journal of Asian Earth Sciences* **189**, 104155. doi: 10.1016/j.jseaes.2019.104155.

Patiño Douce AE (1999) What do experiments tell us about the relative contributions of crust and mantle to the origin of granitic magmas? In *Understanding Granites: Integrating New and Classical Techniques* (eds A Castro, C Fernandez and JL Vigneresse), pp. 55–75. Geological Society of London, Special Publication no. 168.

Pearce JA, Harris NBW and Tindle AG (1984) Trace element discrimination diagrams for the tectonic interpretation of granitic rocks. *Journal of Petrology* **25**, 956–83.

Peccerillo A and Taylor SR (1976) Geochemistry of Eocene calc-alkaline volcanic rocks form the Kastamonu area, Northern Turkey. *Contributions to Mineralogy and Petrology* **58**, 63–81.

Plank T (2005) Constraints from thorium/lanthanum on sediment recycling at subduction zones and the evolution of the continents. *Journal of Petrology* **46**, 921–44.

Qin HF, Li YF, Huang C, Cai SH and Ren SM (2013) Palaeomagnetic investigation of Permian sandstone in Taohaiyingzi area of Inner Mongolia and its tectonic significance. *Geological Bulletin of China* **32**, 388–98 (in Chinese with English abstract).

Qin F, Liu JM, Zeng QD and Luo ZH (2009) Petrogenetic and metallogenic mechanism of the Xiaodonggou porphyry molybdenum deposit in Hexigten Banner, Inner Mongolia. *Acta Petrologica Sinica* **25**, 3357–68 (in Chinese with English abstract).

Rapp PR and Watson EB (1995) Dehydration melting of metabasalt at 8–32 kbar: implications for continental growth and crust-mantle recycling. *Journal of Petrology* **36**, 891–931.

Ren YS, Niu JP, Wang H and Lei E (2009) LA-ICP-MS zircon U–Pb age and its geological significance of tungsten-bearing Mengjialing granitic intrusion in Siping area, Jilin Province. *Journal of Mineralogy and Petrology* **29**, 100–5 (in Chinese with English abstract).

Ren Q, Zhang S, Wu H, Liang Z, Miao X, Zhao H, Li H, Yang T, Pei J and Davis GA (2016) Further paleomagnetic results from the ~155 Ma Tiaojishan Formation, Yanshan Belt, North China, and their implications

for the tectonic evolution of the Mongol-Okhotsk suture. *Gondwana Research* **35**, 180–91.

Ribeiro JM, Stern RJ, Kelley KA, Martinez F, Ishizuka O, Manton WI and Ohara Y (2013) Nature and distribution of slab-derived fluids and mantle sources beneath the Southeast Mariana forearc rift. *Geochemistry, Geophysics, Geosystems* **14**, 4585–607.

Romer RL and Kroner U (2016) Phanerozoic tin and tungsten mineralization—tectonic controls on the distribution of enriched protoliths and heat sources for crustal melting. *Gondwana Research* **31**, 60–95.

Romer RL, Meixner A and Förster HJ (2014) Lithium and boron in late-orogenic granites – isotopic fingerprints for the source of crustal melts? *Geochimica et Cosmochimica Acta* **131**, 98–114.

Rudnick RL and Gao S (2003) Composition of the continental crust. In *Treatise on Geochemistry, Vol. 3* (eds HD Holland and KK Turekian), pp. 1–64. Oxford: Elsevier-Pergamon.

Sarjoughian F, Kananian A, Haschke M, Ahmadian J, Ling W and Zong K (2012) Magma mingling and hybridization in the Kuh-e Dom pluton, Central Iran. *Journal of Asian Earth Sciences* **54–55**, 49–63.

Schaller T, Dingwell DB, Keppler H, Knöller W, Merwin L and Sebald A (1992) Fluorine in silicate glasses: a multinuclear nuclear magnetic resonance study. *Geochimica et Cosmochimica Acta* **56**, 701–7.

Sengör AMC, Natal'in BA and Burtman VS (1993) Evolution of the Altaid tectonic collage and Paleozoic crustal growth in Eurasia. *Nature* **364**, 299–307.

Shang QH (2004) Occurrences of Permian radiolarians in central and eastern Nei Mongol (Inner Mongolia) and their geological significance to the Northern China Orogen. *Chinese Science Bulletin* **49**, 2613–19.

Shao J, Li XR and Yang HZ (2011) Zircon SHRIMP U–Pb dating of granite in the Cuihongshan polymetallic deposit and its geological implications. *Acta Geoscientica Sinica* **32**, 163–70 (in Chinese with English abstract).

Shao JA, Zhang LQ, Xiao QH and Li XB (2005) Rising of Da Hinggan Mts in Mesozoic: a possible mechanism of intracontinental orogeny. *Acta Petrologica Sinica* **21**, 789–94 (in Chinese with English abstract).

Shi YR, Liu DY, Miao LC, Zhang FQ, Jian P, Zhang W, Hou KJ and Xu JY (2010) Devonian A-type granitic magmatism on the northern margin of the North China Craton: SHRIMP U–Pb zircon dating and Hf isotopes of the Hongshan granite at Chifeng, Inner Mongolia, China. *Gondwana Research* **17**, 632–41.

Shi KT, Wang KY, Ma XL, Li SD, Li J and Wang R (2020) Fluid inclusions, C–H–O–S–Pb isotope systematics, geochronology and geochemistry of the Budunhua Cu deposit, northeast China: implications for ore genesis. *Geoscience Frontiers* **11**, 1145–61.

Signorelli S and Carroll MR (2000) Solubility and fluid-melt partitioning of Cl in hydrous phonolitic melts. *Geochimica et Cosmochimica Acta* **64**, 2851–62.

Singh SK and Singh S (2001) Geochemistry and tungsten metallogeny of the Balda granite, Rajasthan, India. *Gondwana Research* **4**, 487–95.

Skjerlie KP and Johnston AD (1993) Vapor-absent melting at 10 kbar of a biotite- and amphibole-bearing tonalitic gneiss: implications for the generation of A-type granites. *Geology* **20**, 263–6.

Söderlund U, Patchett PJ, Vervoort JD and Isachsen CE (2004) The ^{176}Lu decay constant determined by Lu–Hf and U–Pb isotope systematics of Precambrian mafic intrusions. *Earth and Planetary Science Letters* **219**, 311–24.

Stein HJ (2014) Dating and tracing the history of ore formation. In *Treatise in Geochemistry (2nd Edition), Vol. 13* (eds KK Turekian, HD Holland and SD Scott), pp. 88–118. Oxford: Elsevier-Pergamon.

Steiner BM (2019) W and Li–Cs–Ta geochemical signatures in I-type granites – a case study from the Vosges Mountains, NE France. *Journal of Geochemical Exploration* **197**, 238–50.

Sun YG, Li BL, Sun FY, Ding QF, Wang BY, Li YJ and Wang K (2020) Mineralization events in the Xiaokele porphyry Cu (–Mo) deposit, NE China: evidence from zircon U–Pb and K-feldspar Ar–Ar geochronology and petrochemistry. *Resource Geology* **70**, 254–72.

Sun SS and McDonough WF (1989) Chemical and isotopic systematics of oceanic basalts: implications for mantle composition and processes. In *Magmatism in the Ocean Basins* (eds AD Saunders and MJ Norry), pp. 313–45. Geological Society of London, Special Publication no. 42.

Suo YH, Li SZ, Jin C, Zhang Y, Zhou J, Li XY, Wang PC, Liu Z, Wang XY and Somerville I (2019) Eastward tectonic migration and transition of the Jurassic–Cretaceous Andean-type continental margin along Southeast China. *Earth-Science Reviews* **196**, 102884. doi: 10.1016/j.earscirev.2019.102884.

Tang ZY, Sun DY, Mao AQ, Yang DG, Deng CZ and Liu Y (2019) Timing and evolution of Mesozoic volcanism in the central Great Xing'an Range, northeastern China. *Geological Journal* **54**, 3737–54.

Taylor SR and McLennan SM (1995) The geochemical evolution of the continental crust. *Reviews of Geophysics* **33**, 241–65.

Thomas R, Förster HJ, Rickers K and Webster JD (2005) Formation of extremely F-rich hydrous melt fractions and hydrothermal fluids during differentiation of highly evolved tin-granite magmas: a melt/fluid-inclusion study. *Contributions to Mineralogy and Petrology* **148**, 582–601.

Tindle AG and Pearce JA (1983) Assimilation and partial melting of continental crust: evidence from the mineralogy and geochemistry of autoliths and xenoliths. *Lithos* **16**, 185–202.

Tomurtogoo O, Windley BF, Kroner A, Badarch G and Liu DY (2005) Zircon age and occurrence of the Adaatsag ophiolite and Muron shear zone, central Mongolia: constraints on the evolution of the Mongol–Okhotsk ocean, suture and orogen. *Journal of the Geological Society, London* **162**, 197–229.

Turner S, Arnaud N, Liu J, Rogers N, Hawkesworth C, Harris N, Kelley S, Van Calsteren P and Deng W (1996) Post-collision, shoshonitic volcanism on the Tibetan Plateau: implications for convective thinning of the lithosphere and the source of ocean island basalts. *Journal of Petrology* **37**, 45–71.

Turner SP, Foden JD and Morrison RS (1992) Derivation of some A-type magmas by fractionation of basaltic magma: an example from the Padthaway Ridge, South Australia. *Lithos* **28**, 151–79.

Vallance J, Cathelineau M, Marignac C, Boiron MC, Fourcade S, Martineau F and Fabre C (2001) Microfracturing and fluid mixing in granites: W-(Sn) ore deposition at Vaulry (NW French Massif Central). *Tectonophysics* **336**, 43–61.

Vernon RH (1984) Microgranitoid enclaves in granites-globules of hybrid magma quenched in a plutonic environment. *Nature* **309**, 438–39.

Vernon RH (2014) Microstructures of microgranitoid enclaves and the origin of S-type granitoids. *Australian Journal of Earth Sciences* **61**, 227–39.

Vernon RH, Etheridge MA and Wall VJ (1988) Shape and microstructure of microgranitoid enclaves: indicators of magma mingling and flow. *Lithos* **22**, 1–11.

Vindel E, Lopez JA, Boiron MC, Cathelineau M and Prieto AC (1995) P-V-T-X -fO$_2$ evolution from wolframite to sulphide depositional stages in intragranitic W-veins. An example from the Spanish Central System. *European Journal of Mineralogy* **7**, 675–88.

Wan L, Lu CD, Zeng ZX, Mohammed AS, Liu ZH, Dai QQ and Chen KL (2019) Nature and significance of the late Mesozoic granitoids in the southern Great Xing'an range, eastern Central Asian Orogenic Belt. *International Geology Review* **61**, 584–606.

Wang F, Bagas L, Jiang S and Liu Y (2017) Geological, geochemical, and geochronological characteristics of Weilasituo Sn-polymetal deposit, Inner Mongolia, China. *Ore Geology Reviews* **80**, 1206–29.

Wang CZ, Gao Q, Ren L, Chen JW, Wang WB and Zheng DH (2019) Fluid inclusions, H-O isotope and metallogenic epoch of the Xin'antun W-Mo deposit in Jiaohe City, Jilin Province. *Geology and Exploration* **55**, 673–84 (in Chinese with English abstract).

Wang ZH, Ge WC, Yang H, Zhang YL, Bi JH, Tian DX and Xu WL (2015) Middle Jurassic oceanic island igneous rocks of the Raohe accretionary complex, northeastern China: petrogenesis and tectonic implications. *Journal of Asian Earth Sciences* **111**, 120–37.

Wang T, Guo L, Zhang L, Yang QD, Zhang JJ, Tong Y and Ye K (2015) Timing and evolution of Jurassic–Cretaceous granitoid magmatisms in the Mongol-Okhotsk belt and adjacent areas, NE Asia: implications for transition from contractional crustal thickening to extensional thinning and geodynamic settings. *Journal of Asian Earth Sciences* **97**, 365–92.

Wang T, Guo L, Zheng YD, Donskaya T, Gladkochub G, Zeng LS, Li J, Wang YB and Mazukabzov AM (2012) Timing and processes of Late Mesozoic mid-lower-crustal extension in continental NE Asia and implications for the tectonic setting of the destruction of the North China Craton:

mainly constrained by zircon U–Pb ages from metamorphic core complexes. *Lithos* **154**, 315–45.

Wang L, Tang L, Zhang ST, Santosh M, Pei QM, Cao HW and Liu FG (2020) Genesis of the Yujiadian F–Pb–Zn–Ag deposit, Inner Mongolia, NE China: constraints from geochemistry, fluid inclusion, zircon geochronology and stable isotopes. *Ore Geology Reviews* **122**, 103528. doi: 10.1016/j.oregeorev.2020.103528.

Wang Y, Xu B, Cheng SD, Liao W, Shao J and Wang Y (2014) Zircon U–Pb dating of the mafic lava from Wudaoshimen, Hexigten, Inner Mongolia and its geological significance. *Acta Petrologica Sinica* **30**, 2055–62 (in Chinese with English abstract).

Wang RL, Zeng QD, Zhang ZC, Guo YP and Lu JH (2020) Fluid evolution, H–O isotope and Re–Os age of molybdenite from the Baiyinhan tungsten deposit in the Eastern Central Asian Orogenic Belt, NE China, and its geological significance. *Minerals* **10**, 664.

Wang RL, Zeng QD, Zhang ZC, Zhou LL and Qin KZ (2021) Extensive mineralization in the eastern segment of the Xingmeng orogenic belt, NE China: a regional view. *Ore Geology Reviews* **135**, 104204. doi: 10.1016/j.oregeorev.2021.104204.

Wang T, Zheng Y, Zhang J, Zeng L, Donskaya T, Guo L and Li J (2011) Pattern and kinematic polarity of late Mesozoic extension in continental NE Asia: perspectives from metamorphic core complexes. *Tectonics* **30**, 1–27.

Wang F, Zhou XH, Zhang LC, Ying JF, Zhang YT, Wu FY and Zhu RX (2006) Late Mesozoic volcanism in the Great Xing'an Range (NE China): timing and implications for the dynamic setting of NE Asia. *Earth and Planetary Science Letters* **251**, 179–98.

Watson EB and Harrison TM (1983) Zircon saturation revisited: temperature and composition effects in a variety of crustal magma types. *Earth and Planetary Science Letters* **64**, 295–304.

Webster JD and Holloway JR (1988) Experimental constraints on the partitioning of Cl between topaz rhyolite melt and H_2O and H_2O+CO_2 fluids: new implications for granitic differentiation and ore deposition. *Geochimica et Cosmochimica Acta* **52**, 2091–105.

Webster J, Thomas R, Förster HJ, Seltmann R and Tappen C (2004) Geochemical evolution of halogen-enriched granite magmas and mineralizing fluids of the Zinnwald tin–tungsten mining district, Erzgebirge, Germany. *Mineralium Deposita* **39**, 452–72.

Wedepohl KH (1995) The composition of the continental crust. *Geochimica et Cosmochimica Acta* **59**, 1217–32.

Wei W, Lv XB and Wang XD (2021) The granite porphyry hidden in the Shuangjianzishan deposit, southern Great Xing'an Range, NE China: geochronology, isotope geochemistry and tectonic implications. *Geological Magazine* **158**, 995–1009.

Wei W, Zou T, Huang XK, Jiang BB, Zhu XY and Wu XY (2020) Petrogenesis of early Cretaceous granitoids in the southern Great Xing'an Range, NE China: constraints from the Haliheiba pluton. *Geochemistry* **80**, 125608. doi: 10.1016/j.chemer.2020.125608.

Whalen JB, Currie KL and Chappell BW (1987) A-type granites: geochemical characteristics, discrimination and petrogenesis. *Contributions to Mineralogy and Petrology* **95**, 407–19.

White RV, Tarney J, Kerr AC, Saunders AD, Kempton PD, Pringle MS and Klaver GT (1999) Modification of an oceanic plateau, Aruba, Dutch Caribbean: implications for the generation of continental crust. *Lithos* **46**, 43–68.

Wilde SA (2015) Final amalgamation of the Central Asian Orogenic Belt in NE China: Paleo-Asian Ocean closure versus Paleo-Pacific plate subduction — a review of the evidence. *Tectonophysics* **662**, 345–62.

Wood SA and Samson IM (2000) The hydrothermal geochemistry of tungsten in granitoid environments: I. Relative solubilities of ferberite and scheelite as a function of T, P, pH, and m NaCl. *Economic Geology* **95**, 143–82.

Wu FY, Lin JQ, Wilde SA, Zhang XO and Yang JH (2005) Nature and significance of the Early Cretaceous giant igneous event in eastern China. *Earth and Planetary Science Letters* **233**, 103–19.

Wu FY, Sun DY, Ge WC, Zhang YB, Grant ML, Wilde SA and Jahn BM (2011) Geochronology of the Phanerozoic granitoids in northeastern China. *Journal of Asian Earth Sciences* **41**, 1–30.

Xiang AP, Chen YC, Bagas L, She HQ, Kang YJ, Yang WS and Li CJ (2016) Molybdenite Re–Os and U–Pb zircon dating and genesis of the Dayana W–Mo deposit in eastern Ujumchin, Inner Mongolia. *Ore Geology Reviews* **78**, 268–80.

Xiang AP, Chen YC, She HQ, Li GM and Li YX (2018) Chronology and geochemical characteristics of granite in Weilianhe of Inner Mongolia and its geological significance. *Geology in China* **45**, 963–76 (in Chinese with English abstract).

Xiang AP, Wang YJ, Qin DJ, She HQ, Han ZG, Guan JD and Kang YJ (2014) Metallogenic and diagenetic age of Honghuaerji tungsten polymetallic deposit in Inner Mongolia. *Mineral Deposits* **33**, 428–39 (in Chinese with English abstract).

Xiao WJ and Santosh M (2014) The western Central Asian Orogenic Belt: a window to accretionary orogenesis and continental growth. *Gondwana Research* **25**, 1429–44.

Xie W, Zeng QD, Wang RL, Wu JJ, Zhang ZM, Li FC and Zhang Z (2021) Spatial-temporal distribution and tectonic setting of Mesozoic W-mineralized granitoids in the Xing-Meng Orogenic Belt, NE China. *International Geology Review*, published online 30 August 2021. doi: 10.1080/00206814.2021.1961105.

Xu B, Charvet J, Chen Y, Zhao P and Shi GZ (2013) Middle Paleozoic convergent orogenic belts in western Inner Mongolia (China): framework, kinematics, geochronology and implications for tectonic evolution of the Central Asian Orogenic Belt. *Gondwana Research* **23**, 1342–64.

Xu WL, Pei FP, Wang F, Meng E, Ji WQ, Yang DB and Wang W (2013) Spatial-temporal relationships of Mesozoic volcanic rocks in NE China: constraints on tectonic overprinting and transformations between multiple tectonic systems. *Journal of Asian Earth Sciences* **74**, 167–93.

Xu B, Zhao P, Wang YY, Liao W, Luo ZW, Bao QZ and Zhou YH (2015) The pre-Devonian tectonic framework of Xing'an-Mongolia orogenic belt (XMOB) in north China. *Journal of Asian Earth Sciences* **97**, 183–96.

Yang H, Ge WC, Zhao GC, Dong Y, Xu WL, Ji Z and Yu JJ (2015) Late Triassic intrusive complex in the Jidong region, Jiamusi-Khanka Block, NE China: geochemistry, zircon U–Pb ages, Lu–Hf isotopes, and implications for magma mingling and mixing. *Lithos* **224–225**, 143–59.

Yang WB, Niu HC, Hollings P, Zurevinski SE and Li NB (2017) The role of recycled oceanic crust in the generation of alkaline A-type granites. *Journal of Geophysical Research: Solid Earth* **122**, 9775–83.

Yang F, Sun J, Wang Y, Fu J, Na F, Fan Z and Hu Z (2019) Geology, geochronology and geochemistry of Weilasituo Sn-polymetallic deposit in Inner Mongolia, China. *Minerals* **9**, 1–28.

Yang ZH, Wang JP, Liu JJ, Wang SG, Wang QY, Kang SG, Zhang JX and Zhao Y (2016) Geochronology and geochemistry of the Wurinitu granites in Inner Mongolia and their geological implications *Geoscience* **30**, 528–40 (in Chinese with English abstract).

Yang JH, Wu FY, Chung SL, Wilde SA and Chu MF (2004) Multiple sources for the origin of granites: geochemical and Nd–Sr isotopic evidence from the Gudaoling granite and its mafic enclaves, Northeast China. *Geochimica et Cosmochimica Acta* **68**, 4469–83.

Yang JH, Wu FY, Shao JA, Wilde SA, Xie LW and Liu XM (2006) Constrains on the timing of uplift of the Yanshan fold and thrust belt, North China. *Earth and Planetary Science Letters* **246**, 336–52.

Yuan SD, Williams-Jones AE, Mao JW, Zhao PL, Yan C and Zhang DL (2018) The origin of the Zhangjialong tungsten deposit, South China: implications for W–Sn mineralization in large granite batholiths. *Economic Geology* **113**, 1193–208.

Yuan SD, Williams-Jones AE, Romer RL, Zhao PL and Mao JW (2019) Protolith-related thermal controls on the decoupling of Sn and W in Sn–W metallogenic provinces: insights from the Nanling region, China. *Economic Geology* **114**, 1005–12.

Zajacz Z, Halter WE, Pettke T and Guillong M (2008) Determination of fluid/melt partition coefficients by LA-ICPMS analysis of co-existing fluid and silicate melt inclusions: controls on element partitioning. *Geochimica et Cosmochimica Acta* **72**, 2169–97.

Zeng QD, Liu JM, Chu SX, Wang YB, Sun Y, Duan XX and Zhou LL (2012) Mesozoic molybdenum deposits in the East Xingmeng orogenic belt, northeast China: characteristics and tectonic setting. *International Geology Review* **54**, 1843–69.

Zeng QD, Liu JM, Qin F and Zhang ZL (2010) Geochronology of the Xiaodonggou porphyry Mo deposit in northern margin of North China Craton. *Resource Geology* **60**, 192–202.

Zeng QD, Qin KZ, Liu JM, Li GM, Zhai MG, Chu SX and Guo YP (2015a) Porphyry molybdenum deposits in the Tianshan–Xingmeng orogenic belt, northern China. *International Journal of Earth Sciences* **104**, 991–1023.

Zeng QD, Sun Y, Chu SX, Duan XX and Liu JM (2015b) Geochemistry and geochronology of the Dongshanwan porphyry Mo–W deposit, Northeast China: implications for the Late Jurassic tectonic setting. *Journal of Asian Earth Sciences* **97**, 472–85.

Zhai DG, Liu JJ, Li JM, Zhang M, Li BY, Fu X, Jiang HC, Ma LJ and Qi L (2016) Geochronological study of Weilasituo porphyry type Sn deposit in Inner Mongolia and its geological significance. *Mineral Deposits* **35**, 1011–22 (in Chinese with English abstract).

Zhai M and Santosh M (2013) Metallogeny of the North China Craton: link with secular changes in the evolving Earth. *Gondwana Research* **24**, 275–97.

Zhang ZJ, Cheng QM, Yao LQ, Bai HS and Li C (2016) Zircon U–Pb–Hf isotopic systematics and geochemistry of the granites in the Wurintu molybdenum deposit, Inner Mongolia, China: implications for tectonic setting and genetic type of mineralization. *Acta Geologica Sinica (English Edition)* **90**, 2066–79.

Zhang JH, Ge WC, Wu FY, Wilde SA, Yang JH and Liu XM (2008) Large-scale Early Cretaceous volcanic events in the northern Great Xing'an Range, Northeastern China. *Lithos* **102**, 138–57.

Zhang C, Quan JY, Zhang YJ, Liu ZH, Li W, Wang Y, Qian C, Zhang L and Ge JT (2020) Late Mesozoic tectonic evolution of the southern Great Xing'an Range, NE China: evidence from whole-rock geochemistry, and zircon U–Pb ages and Hf isotopes from volcanic rocks. *Lithos* **362–363**, 105409. doi: 10.1016/j.lithos.2020.105409.

Zhang GL, Xie W, Wen SQ, Gong EP, Guo RR and Tang TQ (2020) Petrogenesis and tectonic implications of Late Mesozoic volcanic rocks in the northern and central Great Xing'an Range, NE China: constraints from geochronology and geochemistry. *Geological Journal* **55**, 8282–308.

Zhang Y, Yang JH, Chen JY, Wang H and Xiang YX (2017) Petrogenesis of Jurassic tungsten-bearing granites in the Nanling Range, South China: evidence from whole-rock geochemistry and zircon U–Pb and Hf–O isotopes. *Lithos* **278–281**, 166–80.

Zhang XB, Wang KY, Wang CY, Li W, Yu Q, Wang YC, Li JF, Wan D and Huang GH (2017) Age, genesis, and tectonic setting of the Mo–W mineralized Dongshanwan granite porphyry from the Xilamulun metallogenic belt, NE China. *Journal of Earth Science* **28**, 433–46.

Zhang XH, Zhang HF, Tang YJ, Wilde SA and Hu ZC (2008) Geochemistry of Permian bimodal volcanic rocks from central Inner Mongolia, North China: implication for tectonic setting and Phanerozoic continental growth in Central Asian Orogenic Belt. *Chemical Geology* **249**, 262–81.

Zhang SH, Zhao Y, Ye H, Hou KJ and Li CF (2012) Early Mesozoic alkaline complexes in the northern North China Craton: implications for cratonic lithospheric destruction. *Lithos* **155**, 1–18.

Zhao HL (2014) *Ore genesis and geodynamic settings of tungsten deposits in Eastern Jilin and Heilongjiang Provinces.* Ph.D. thesis, Jinlin University, Changchun, China. Published thesis (in Chinese with English abstract).

Zhou Y (2013) *The mineralization of Sansheng W–Mo deposit in Huade, Inner Mongolia.* M.Sc. thesis, Chinese Academy of Geological Science, Beijing, China. Published thesis (in Chinese with English abstract).

Zhao GC, Sun M, Wilde SA and Li SZ (2005) Late Archaean to Paleoproterozoic evolution of the North China Craton: key issues revisited. *Precambrian Research* **136**, 177–202.

Zhu XY, Zhang ZH, Fu X, Li BY, Wang YL, Jiao ST and Sun YL (2016) Geological and geochemical characteristics of the Weilasito Sn–Zn deposit, Inner Mongolia. *Geology in China* **43**, 188–208 (in Chinese with English abstract).

Zorin YA (1999) Geodynamics of the western part of the Mongol-Okhotsk collisional belt, Trans-Baikal region (Russia) and Mongolia. *Tectonophysics* **306**, 33–56.

Zorpi MJ, Coulon C, Orsini JB and Cocirta C (1989) Magma mingling, zoning and emplacement in calc-alkaline granitoid plutons. *Tectonophysics* **157**, 315–29.